

# ***Nonlinear Control Of Fighter Aircraft***

**Kevin A. Wise  
Jack L. Sedwick  
Yutaka Ikeda**

***The Boeing Company  
St. Louis, Missouri 63166***

**June 1999**

**Contract No. F49620-96-C-0011**

***Air Force Office of  
Scientific Research***

20010301 066

# REPORT DOCUMENTATION PAGE

AFRL-SR-BL-TR-01-

9  
Data sources  
inspect of this  
115 Jefferson

Public reporting burden for this collection of information is estimated to average 1 hour per response gathering and maintaining the data needed, and completing and reviewing the collection of information collection of information, including suggestions for reducing this burden, to Washington Headquarters Davis Highway, Suite 1204, Arlington, VA 22202-4302, and to the Office of Management and Budget, 1

0035

1. AGENCY USE ONLY (Leave blank)		2. REPORT DATE	3. REPORT PERIOD FROM FINAL REPORT JUN 1996 TO JUN 1999	
4. TITLE AND SUBTITLE Nonlinear Control Of Fighter Aircraft			5. FUNDING NUMBERS F49620-96-C-0011	
6. AUTHOR(S) Kevin A. Wise Jack L. Sedwick Yutaka Ikeda				
7. PERFORMING ORGANIZATION NAME(S) AND ADDRESS(ES) McDonnell Douglas Corporation P. O. Box 516 St. Louis Missouri, 63166			8. PERFORMING ORGANIZATION REPORT NUMBER	
9. SPONSORING / MONITORING AGENCY NAME(S) AND ADDRESS(ES) Dr. Marc Jacobs AFOSR/NM Directorate of Mathematics and Geosciences 801 North Randolph Street, Room 732 Arlington, VA 22203-1977			10. SPONSORING / MONITORING AGENCY REPORT NUMBER	
11. SUPPLEMENTARY NOTES				
12a. DISTRIBUTION / AVAILABILITY STATEMENT  <b>DISTRIBUTION STATEMENT A</b> Approved for Public Release Distribution Unlimited			12b. DISTRIBUTION CODE	
13. ABSTRACT (Maximum 200 words)  The problem of designing flight control systems for high performance tailless fighter aircraft is discussed in the report. The research uses linear matrix inequalities and semidefinite programming to addresses three areas of tailless fighter flight control. The first area investigates H2 and Hinf controller design using linear matrix inequalities. The second area uses linear matrix inequalities and linear parameter varying models to develop stability analysis tools for gain scheduled and reconfigurable control laws. The third area focused on using linear matrix inequalities to design aeroservoelastic filters.				
14. SUBJECT TERMS linear matrix inequalities optimal control stability analysis		tailless fighters unstable aircraft gain scheduling		15. NUMBER OF PAGES 122
17. SECURITY CLASSIFICATION OF REPORT UNCLASSIFIED		18. SECURITY CLASSIFICATION OF THIS PAGE UNCLASSIFIED		16. PRICE CODE
17. SECURITY CLASSIFICATION OF REPORT UNCLASSIFIED		19. SECURITY CLASSIFICATION OF ABSTRACT UNCLASSIFIED		20. LIMITATION OF ABSTRACT UL

## Nonlinear Control Of Fighter Aircraft

F49620-96-C-0011

Kevin A. Wise  
 Jack L. Sedwick  
 Yutaka Ikeda

Dr. Marc Jacobs AFOSR/NM  
 Directorate of Mathematics and Geosciences  
 801 North Randolph Street, Room 732  
 Arlington, VA 22203-1977

linear matrix inequalities  
 optimal control  
 stability analysis

tailless fighters  
 unstable aircraft  
 gain scheduling

122

The problem of designing flight control systems for high performance tailless fighter aircraft is discussed in the report. The research uses linear matrix inequalities and semidefinite programming to address three areas of tailless fighter flight control. The first area investigates H2 and Hinf controller design using linear matrix inequalities. The second area uses linear matrix inequalities and linear parameter varying models to develop stability analysis tools for gain scheduled and reconfigurable control laws. The third area focused on using linear matrix inequalities to design aeroservoelastic filters.

$$\Phi_{x_d} = \left[ \begin{array}{ccc|ccc} AR + RA^T & AM & B_1 & RC_1^T & & \\ M^T A^T & 0 & 0 & M^T C_1^T & & \\ \hline B_1^T & 0 & -\gamma I & D_{11}^T & & \\ C_1 R & C_1 M & D_{11} & -\gamma I & & \end{array} \right]$$

$$\left[ \begin{array}{cc|c} \ker(R) & 0 & \\ \hline 0 & I & \end{array} \right]^T \left[ \begin{array}{ccc|ccc} AR + RA^T & B_1 & & & & \\ C_1 R & -\gamma I & D_{11} & & & \\ \hline B_1^T & D_{11}^T & -\gamma I & & & \end{array} \right] \left[ \begin{array}{cc|c} \ker(R) & 0 & \\ \hline 0 & I & \end{array} \right] < 0$$

$$\left[ \begin{array}{cc|cc|ccc} W_{12} & 0 & 0 & & & & \\ \hline -\hat{B}_2^T W_{12} & U_{12} & 0 & & & & \\ \hline 0 & 0 & I & & & & \end{array} \right]^T \left[ \begin{array}{ccc|ccc} AR + RA^T & B_1 & & & & \\ C_1 R & -\gamma I & D_{11} & & & \\ \hline B_1^T & D_{11}^T & -\gamma I & & & \end{array} \right] \left[ \begin{array}{cc|cc|ccc} W_{12} & 0 & 0 & & & & \\ \hline -\hat{B}_2^T W_{12} & U_{12} & 0 & & & & \\ \hline 0 & 0 & I & & & & \end{array} \right] < 0$$



## **Preface**

The research described in this final report was performed at The Boeing Company, Saint Louis, Missouri, under Contract F49620-96-C-0011, entitled "Nonlinear Control of Fighter Aircraft." The program was managed by Dr. Marc Q. Jacobs of the Dynamics and Control Branch, Directorate of Mathematical and Computer Sciences, Air Force Office of Scientific Research, Bolling Air Force Base, DC.

Boeing's program manager and principal investigator was Dr. Kevin A. Wise. The research described herein was performed by Dr. Kevin A. Wise, Dr. Jackson L. Sedwick, Dr. Yutaka Ikeda, Dr. Rowena L. Eberhardt, and Mr. Joseph S. Brinker.

The research reported here was conducted during the period June 1996 through June 1999.

(Blank Page)

TABLE OF CONTENTS

Section	Title	Page
1	Introduction	1
1.1	Research Objectives, Accomplishments, and Transitions	1
1.2	Organization of the Report	4
1.3	Chapter 1 References	4
2	Tailless Fighter Flight Control Design Using LMIs	6
2.1	Introduction	6
2.2	$H_2$ Controller Design Using LMIs	6
2.2.1	$H_2$ -Norm Minimization	6
2.2.2	LMIs For Standard LQR Problems	9
2.2.3	$H_2$ -Norm Minimization For Linear Time Varying Systems	11
2.2.4	$H_2$ Controller Design and Simulation Results	12
2.3	$H_\infty$ Controller Design Using LMIs	14
2.3.1	State Feedback ARE $H_\infty$ Controller Formulas	24
2.3.2	$H_\infty$ Controller LMI Problem	25
2.3.3	$H_\infty$ Controller LMI Problem With Lower Bound Constraint	27
2.3.4	Methods Used To Improve Numerical Accuracy And Conditioning	28
2.3.5	An $H_\infty$ Controller LMI Problem With Gain Conditioning	30
2.3.6	$H_\infty$ Controller LMI Problem For LTV Systems Caused By Gain Scheduling	31
2.3.7	$H_\infty$ Controller Design and Simulation Results	34
2.4	Chapter 2 References	36
3	Stability Analysis Of Gain Scheduled and Reconfigurable Control Systems Using LMIs	38
3.1	Introduction	38
3.2	Tailless Fighter Model With Battle Damage	40
3.3	Gain Scheduled Flight Control Design	46
3.4	Stability Analysis Using LMIs	50
3.5	Tailless Fighter Analysis Results	57
3.6	Chapter 3 Conclusions	67
3.7	Chapter 3 References	67
4	Aeroservoelastic Filter Optimization using LMIs	69
4.1	Introduction	69
4.2	ASE Compensation Filter Design	69
4.3	Optimization of ASE Filter Coefficients	73
4.4	Conclusions	76
4.5	Chapter 4 References	76
Appendix A	Boeing Tailless Advanced Fighter Aircraft	77
A.1	Mass Properties Models	79
A.2	Aerodynamics Models	80

A.2.1	Aerodynamic Flexibility Effects	86
A.3	Propulsion Model	87
A.4	Rigid Body Dynamics	92
A.5	Flexible Vehicle (Structural) Dynamics	98
A.6	Actuator Models	104
A.7	Sensor Models	109
A.8	Flight Control System Digital Effects	110
A.9	Loads Model	111
A.10	Atmosphere Model	113
A.10.1	Atmospheric Conditions	113
A.10.2	Wind and Turbulence	114

LIST OF PAGES

Title Page

i-viii

1-122

LIST OF FIGURES

Figure	Title	Page
Figure 2.1	$H_2$ Controller Step Acceleration Command Simulation Response	14
Figure 2.2	Controller Design Model	15
Figure 2.3	$H_\infty$ Controller LMI $\gamma$ Optimization	26
Figure 2.4	$H_\infty$ Controller LMI $\gamma$ Optimization With Lower Bound Constraint	28
Figure 2.5	Bounding $L(\gamma, R)$ With $\epsilon$	29
Figure 2.6	Surface Fit To Optimal $\gamma$	33
Figure 2.7	$H_\infty$ Controller Step Acceleration Command Simulation Response	36
Figure 3.1	Polynomial Approximation Of The A Matrix	44
Figure 3.2	Polynomial Approximation Of The B Matrix	45
Figure 3.3	Longitudinal controller structure.	47
Figure 3.4	Pitch Controller Output Feedback Gains	48
Figure 3.5	Point Design Flying Qualities Analysis	49
Figure 3.6	LMI bounds on the state transition matrix.	56
Figure 3.7	Category II stability analysis results.	60
Figure 3.8	Category III stability analysis results.	65
Figure 3.9	Category IV stability analysis results.	66
Figure 4.1	TAFAs ASE Compensation Filters	70
Figure 4.2	Open Loop Frequency Response Analysis to Validate ASE Compensation Filter Design	72
Figure 4.3	200 Hz Filter Design Bounds	74
Figure 4.4	200 Hz Filter Frequency Response	75
Figure A.1:	Three-View of TAFAs Aircraft	77
Figure A.2:	Block Diagram of TAFAs Analysis / Simulation Model	79
Figure A.3:	TAFAs Aerodynamic Control Increments	84
Figure A.4:	TAFAs Aerodynamic Flexibility Effect Model	87
Figure A.5:	TAFAs Propulsion System Data	88
Figure A.6:	Relationship Between Engine and Nozzle Axes	89
Figure A.7:	Frequency Response of Longitudinal Axis Flexible Vehicle Dynamics Model for Low Altitude Ingress / Egress Flight Condition	104
Figure A.8:	TAFAs Control Effector Sign Conventions	104
Figure A.9:	High Fidelity Actuator Model Torque-Speed Curve	106
Figure A.10:	TAFAs Sensor Model	109
Figure A.11:	TAFAs Loads Model Definitions	112
Figure A.12:	Linear Wind Shear Model Definitions	116
Figure A.13:	Logarithmic Wind Shear Model	117
Figure A.14:	Vector Wind Shear Model	117
Figure A.15:	Dryden Turbulence Spectra and Continuous Weighting Filter Implementation	118
Figure A.16:	Medium / High Altitude Turbulence Intensities	120
Figure A.17:	MIL-SPEC Discrete Gust Profile	121
Figure A.18:	One Minus Cosine Discrete Gust Model	122

## LIST OF TABLES

<b>Table</b>	<b>Title</b>	<b>Page</b>
Table A.1:	TAFAs Mass Properties Models	80
Table A.2:	TAFAs Airframe Geometry Constants	85
Table A.3:	TAFAs Propulsion Model Constants	92
Table A.4:	Grid Points Used in Development of TAFAs Structural Dynamics Model	101
Table A.5:	Mass Properties of TAFAs Control Effectors	102
Table A.6:	Offset Between cg and Pivot Point of TAFAs Control Effectors	102
Table A.7:	Moment of Inertia of TAFAs Control Effectors	103
Table A.8:	TAFAs Actuator Dynamics	105
Table A.9:	TAFAs Low Fidelity Actuator Model Position and Rate Limits	105
Table A.10:	TAFAs High Fidelity Actuator Model Parameters	108
Table A.11:	TAFAs Hinge Moment Model Parameters	109
Table A.12:	TAFAs Sensor Model Parameters	110
Table A.13:	Turbulence Model Parameters	120

## LIST OF ACRONYMS

<b>Acronym</b>	<b>Description</b>
AFOSR	Air Force Office Of Scientific Research
AOA	Angle of Attack
ARE	Algebraic Riccati Equation
ARI	Algebraic Riccati Inequality
ASE	Aeroservoelastic
FIR	Finite Impulse Response
IRAD	Independent Research And Development
LDI	Linear Differential Inclusion
LMI	Linear Matrix Inequality
LPV	Linear Parameter Varying
LO	Low Observable
LOES	Low Order Equivalent System
LQR	Linear Quadratic Elevator
LTI	Linear Time Invariant
LTV	Linear Time Varying
NAIC	National Air Intelligence Center
TAFAs	Tailless Advanced Fighter Aircraft

## Chapter 1

### Introduction

New aircraft systems are being designed to satisfy requirements for a low radar signature, low infrared signature, and low visible signature. "Low observability" (LO) will be central to all future fighter aircraft. The design of LO air combat systems is a multidisciplinary problem in aerodynamics, control, electromagnetics, and structural design. Critical flight control research problems for these kind of aircraft exist in nonlinear and adaptive control, reconfigurable control, multivariable control, performance optimizing control, tailless aircraft control, and thrust vectoring for envelope expansion. New control system design, analysis, and optimization tools are needed to address the challenges of controlling these highly nonlinear aircraft.

The *Nonlinear Control of Fighter Aircraft* research was focused on exploiting recent developments in the use of Linear Matrix Inequalities (LMIs) for tailless fighter control system design, analysis, and optimization. Specific progress was made in the following three areas:

- Tailless Fighter Flight Control Design
- Stability Analysis Of Gain Scheduled and Reconfigurable Flight Control Systems
- Aeroservoelastic Filter Optimization

#### 1.1 Research Objectives, Accomplishments and Transitions

Our research objectives in flight control design addressed the challenges associated with tailless fighter system modeling, design, and analysis. Tailless fighters have aerodynamics that are very nonlinear, and they are typically unstable in multiple axes. Our flight control design research objectives in tailless fighter flight control system design address this nonlinear flight control design problem using a linear parameter varying (LPV) approach, and using LMIs, design  $H_2$  and  $H_\infty$  optimal control systems within this context, using the LPV models to represent the nonlinear control system (including gain scheduling).

The research objectives in stability analysis focused on using LMIs for analyzing conventional gain scheduled control systems (currently used in fighter aircraft) as well as

reconfigurable flight control systems. In industry, fighter aircraft flight control systems are analyzed using conventional linear analysis methods on aircraft models representing a trimmed flight condition. These analyses do not address the gain scheduling and time varying parameters (some slowly varying, some fast) that are actually present in the flight control system implementation and aircraft dynamics.

In recent years, reconfigurable flight control systems have emerged and are being flight tested in research aircraft. In transitioning reconfigurable flight control systems to production aircraft, engineers will need analysis tools to assess stability margins. By modeling reconfigurable flight control systems as a gain scheduled LPV system, LMIs can be used to assess system stability. The development of this capability was addressed under this research program.

The research objectives in aeroservoelastic (ASE) filter design focused on using LMIs to design filter coefficients over a range of flight conditions. The rate and acceleration measurements used in flight control systems are corrupted by flexible body motion. Filters are designed to remove these signals so that they are not amplified by the control system feedback. Typically, notch filters combined with low pass filters are used. These filters must be robust to the aircraft's varying mass properties, stores (weapons), and flight conditions. Robustness, typically built into the design by using wide notch filters, usually results in large amounts of phase lag near the loop gain crossover frequency. For tailless fighters that are unstable in multiple axes, this phase lag may be unacceptable. Our research objectives in this area were focused on developing tools for ASE filter design to improve upon this time consuming and difficult problem.

The following paragraphs briefly summarize the research objective, accomplishments made, and transitions on the technology in each area. The LMI software used to perform this research was transitioned from Stanford University (Stephen Boyd) to Boeing. Journal papers [1-3] and conference papers [4-8] disseminating this research are listed at the end of this chapter in the references.

### **Tailless Fighter Flight Control Design**

The research objective was to develop LMI based design tools for tailless fighter flight control design. Accomplishments include: 1) Deriving a new LQR based approach for pitch plane flight control system design, integrating the approach into an automated design tool, and transitioning this tool to the National Air Intelligence Center (NAIC) in Dayton; 2) Developing design models and LMI software for  $H_2$  and  $H_\infty$  optimal control system design. Seventeen different  $H_2$  and  $H_\infty$  optimal control system designs formulations were implemented. Chapter 2 summarizes the LMI design problems. These tools have been transitioned to Boeing's Guidance and Control Technology IRAD for further maturation and application to aircraft flight control system design problems.

### **Stability Analysis Of Gain Scheduled and Reconfigurable Flight Control Systems**

The research objective was to develop a LMI based proof of stability tool for reconfigurable flight control systems. Accomplishments include development of LPV based models for modeling gain scheduled and reconfigurable flight control systems, formulation of the LMI for stability analysis, and application of the approach to Boeing's Tailless Advanced Fighter Aircraft (TAFA). The LMI analysis was applied to a gain scheduled control system and was used to assess system stability in the presence of gain scheduling and time varying model parameters. The LMI analysis was also applied to a reconfigurable flight control system designed to accommodate battle damage, and was used to assess system stability during reconfiguration of the flight control system. These tools were also transitioned to Boeing's Guidance and Control Technology IRAD for further maturation and application to aircraft flight control system design problems.

### **Aeroservoelastic Filter Optimization**

The research objective was to develop an LMI based tool for optimizing ASE filter designs to minimize phase lag at frequencies near the loop gain crossover frequency subject to constraints on providing a minimum gain attenuation at the flexible body modes. This tool must also accommodate the aircraft's varying mass properties, weapons load out, and flight

conditions. Our accomplishments include the preliminary development of an LMI tool for designing these filters, and application of the tool to Boeing's TAFE aircraft model. It was found during this research that the LMI problems grew to extremely large size, saturating the memory on our workstations. This problem caused limited success in this area. Chapter 4 discusses the problem set up and our results.

## 1.2 Organization of the Report

Chapter 2 presents theory for  $H_2$  and  $H_\infty$  optimal flight control system design, application of these design methods to the Boeing TAFE aircraft, and linear simulation results comparing conventional and LMI designs. A detailed description of the Boeing TAFE aircraft is presented in this report in Appendix A, as well as linear models at key flight conditions (also in the appendices). Each Chapter contains at its end the references used in the chapter.

Chapter 3 details the development and application of LMIs for stability analysis of gain scheduled and/or reconfigurable flight control systems.

Chapter 4 summarizes our progress in developing a LMI based tool for ASE filter optimization.

## 1.3 Chapter 1 References

1. K. A. Wise and D. Broy, "Agile Missile Dynamics and Control," *Journal of Guidance, Control, and Dynamics*, Vol. 21, No. 3, 1998, pp. 441-449.
2. K. A. Wise, "Fighter Aircraft Control Challenges and Technology Transition," *Systems and Control in the Twenty-First Century*, Birkhauser, 1996.
3. K. A. Wise and J. S. Brinker, "Stability and Flying Qualities Robustness of a Dynamic Inversion Aircraft Control Law," *Journal of Guidance, Control, and Dynamics*, Vol. 19, No. 6, 1996, pp. 1270-1278.
4. K. A. Wise and J. S. Brinker, "Nonlinear Simulation Analysis of a Tailless Advanced Fighter Aircraft Reconfigurable Flight Control Law," to be published in the Proc. of the AIAA GNC Conference, Portland, OR, August, 1999.
5. K. A. Wise and J. S. Brinker, "Reconfigurable Flight Control for a Tailless Advanced Fighter Aircraft," Proc. of the AIAA GNC Conference, Boston, MA, August, 1998, pp. 75-87.

6. K. A. Wise and J. L. Sedwick, "Stability Analysis of Reconfigurable and Gain Scheduled Flight Control Systems Using LMIs," Proc. of the AIAA GNC Conference, Boston, MA, August, 1998, pp.118-126.
7. K. A. Wise and J. L. Sedwick, "Nonlinear Control Of Agile Missiles Using State Dependent Riccati Equations, Proc. Of the 1997 ACC, Albuquerque NM, June 1997, pp. 379-380.
8. K. A. Wise and D. Broy, "Agile Missile Dynamics and Control," AIAA paper No. 96-3912, presented at the AIAA GNC Conference, San Diego CA, August 1996.

## Chapter 2

### Tailless Fighter Flight Control System Design Using LMIs

#### 2.1 Introduction

This chapter presents derivations of  $H_2$  and  $H_\infty$  LMIs for controller design and applies them to a tailless aircraft at a single flight condition. The theoretical results presented in this chapter build the foundation for using LMIs in analyzing stability for a reconfigurable (gain scheduled) control system that is presented later in Chapter 3.

In general,  $H_2$  and  $H_\infty$  controller design is easily accomplished using control system design and analysis packages like MATRIXx and Matlab by solving Riccati equations. The difficult problem that these tools do not address is the stability analysis of gain scheduled and/or reconfigurable control systems addressed later in Chapter 3. Modeling these systems using LPV models and posing the stability question in a LMI framework gives the engineer a new tool in the analysis of complicated flight control systems. The derivation of controller design formulas presented in this chapter aid in the set up and understanding of the material presented in Chapter 3. The controller design formulas are presented for LTI systems, then followed by time varying systems. The time varying models represent models typically used for gain scheduled flight control systems.

#### 2.2 $H_2$ Controller Design Using LMIs

This section contains the derivation and LMI problems for minimizing the  $H_2$  norm between an exogenous variable  $w$  and the regulated variable  $z$  applied to a linear time invariant (LTI) system. Included is the LMI problem for solving the standard regulator problem, and LMI problems for linear time varying systems.

##### 2.2.1 $H_2$ -Norm Minimization

Consider the plant described by

$$\begin{aligned} \dot{x} &= Ax + B_1 w + B_2 u \\ z &= C_1 x + D_{11} w + D_{12} u \end{aligned} \quad (2.1)$$

where  $E\{w(\tau)w^T(\zeta)\} = I\delta(\tau - \zeta)$ , and with the state feedback control  $u = -Kx$ . The controller design problem is to select the feedback gain matrix  $K$  to minimize the  $H_2$ -norm between  $w$  and  $z$ . This problem is described by

$$\min_K E \left\{ \int_0^{\infty} z^T(\tau)z(\tau)d\tau \right\}. \quad (2.2)$$

Define

$$P(t) \triangleq E\{x(t)x^T(t)\} > 0$$

then, using Eq. (2.1)

$$E\{zz^T\} = (C_1 - D_{12}K)P(C_1 - D_{12}K)^T + D_{11}D_{11}^T.$$

Using  $z^T z = \text{Tr}(zz^T) = \sum_i z_i^2 = \|z\|_2^2$  we have

$$\begin{aligned} E\{z^T z\} &= \text{Tr}(zz^T) \\ &= \text{Tr}(C_1 P C_1^T - D_{12} K P C_1^T - C_1 P K^T D_{12}^T - D_{12} K P K^T D_{12}^T - D_{11} D_{11}^T) \\ &= \text{Tr}(C_1^T C_1 P) - \text{Tr}(C_1^T D_{12} K P) - \text{Tr}(P K^T D_{12}^T C_1) + \text{Tr}(D_{12} K P K^T D_{12}^T) + \text{Tr}(D_{11} D_{11}^T) \end{aligned}$$

Defining

$$Y \triangleq KP$$

and the slack variables

$$\begin{aligned} X &\triangleq D_{12} K P K^T D_{12}^T \geq 0 \\ &= D_{12} K P P^{-1} P K^T D_{12}^T \geq 0. \\ &= D_{12} Y P^{-1} Y^T D_{12}^T \geq 0 \end{aligned}$$

Then, using the Schur complement, this matrix inequality can be written as

$$\begin{aligned} \begin{bmatrix} I & D_{12}Y \\ 0 & P \end{bmatrix} \begin{bmatrix} 0 & 0 \\ 0 & P^{-1} \end{bmatrix} \begin{bmatrix} I & 0 \\ Y^T D_{12}^T & P \end{bmatrix} &= \begin{bmatrix} 0 & D_{12}YP^{-1} \\ 0 & I \end{bmatrix} \begin{bmatrix} I & 0 \\ Y^T D_{12}^T & P \end{bmatrix} \geq 0 \\ &= \begin{bmatrix} D_{12}YP^{-1}Y^T D_{12}^T & D_{12}Y \\ Y^T D_{12}^T & P \end{bmatrix} \geq 0 \\ &= \begin{bmatrix} X & D_{12}Y \\ Y^T D_{12}^T & P \end{bmatrix} \geq 0 \end{aligned}$$

Now,

$$\begin{aligned} E\{\|z\|_2^2\} &= \text{Tr}(zz^T) \\ &= \text{Tr}(C_1^T C_1 P) - 2\text{Tr}(C_1^T D_{12} K P) + \text{Tr}(X) + \text{Tr}(D_{11} D_{11}^T) \end{aligned}$$

The state transition  $\Phi(t)$  satisfies

$$\dot{\Phi} = (A - B_2 K)\Phi, \quad \Phi(0) = I$$

with

$$x(t) = \Phi(t)x_0 + \Phi(t) \int_0^t \Phi^{-1}(\tau) B_1 w(\tau) d\tau.$$

Assuming  $x_0 = 0$ ,

$$\begin{aligned} P(t) &= E\{x(t)x^T(t)\} \\ &= \Phi(t) \int_0^t \int_0^t \Phi^{-1}(\tau) B_1 w(\tau) w^T(\zeta) B_1^T \Phi^{-T}(\zeta) d\tau d\zeta \Phi^T(t) \\ &= \Phi(t) \int_0^t \Phi^{-1}(\tau) B_1 B_1^T \Phi^{-T}(\tau) d\tau \Phi^T(t) \end{aligned}$$

Differentiating yields

$$\dot{P} = (A - B_2 K)P + P(A - B_2 K)^T + B_1 B_1^T$$

or

$$-\dot{P} + AP - B_2 Y + PA^T - Y^T B_2^T + B_1 B_1^T = 0$$

For stability, we have

$$\dot{P} - AP - PA^T + B_2 Y + Y^T B_2^T - B_1 B_1^T \geq 0.$$

The controller design problem in Eq. (2.2) can now be reformulated as the following LMI problem.

### $H_2$ Controller LMI Problem

$$\min_{P, X, Y} \int_0^T \text{Tr}(C_1^T C_1 P) - 2\text{Tr}(C_1^T D_{12} K P) + \text{Tr}(X) + \text{Tr}(D_{11} D_{11}^T) dt \quad (2.3)$$

subject to

$$\begin{aligned} \dot{P} - AP - PA^T + B_2 Y + Y^T B_2^T - B_1 B_1^T &\geq 0 \\ \begin{bmatrix} X & D_{12} Y \\ Y^T D_{12}^T & P \end{bmatrix} &\geq 0 \end{aligned}$$

with  $K = YP^{-1}$ .

### 2.2.2 LMIs For Standard LQR Problems

A special case of the above  $H_2$  design problem is the familiar LQR problem that minimizes

$$E \left\{ \int_0^T (x^T Q x + u^T R u) dt \right\}$$

with  $Q^T = Q \geq 0$  and  $R^T = R > 0$  for the LTI plant  $\dot{x} = Ax + Bu$ . For this special case

$$z = \begin{bmatrix} Q^{1/2} & 0 \\ 0 & R^{1/2} \end{bmatrix} \begin{bmatrix} x \\ u \end{bmatrix}.$$

Then,

$$C_1 = \begin{bmatrix} Q^{1/2} \\ 0 \end{bmatrix}, \quad D_{11} = \begin{bmatrix} 0 \\ 0 \end{bmatrix}, \quad D_{12} = \begin{bmatrix} 0 \\ R^{1/2} \end{bmatrix}$$

$$C_1^T C_1 = Q, \quad C_1^T D_{12} = 0, \quad D_{11}^T D_{11} = 0, \quad D_{12}^T Y = \begin{bmatrix} 0 \\ R^{1/2} Y \end{bmatrix}$$

$$X = \begin{bmatrix} 0 & 0 \\ 0 & R^{1/2} K P K^T R^{1/2} \end{bmatrix}$$

$$\begin{bmatrix} X & D_{12} Y \\ Y^T D_{12}^T & P \end{bmatrix} = \left[ \begin{array}{cc|c} 0 & 0 & 0 \\ 0 & R^{1/2} K P K^T R^{1/2} & R^{1/2} Y \\ \hline 0 & Y^T R^{1/2} & P \end{array} \right]$$

This last expression implies that

$$\begin{bmatrix} R^{1/2} K P K^T R^{1/2} & R^{1/2} Y \\ Y^T R^{1/2} & P \end{bmatrix} \geq 0.$$

Also, that  $Tr(X) = Tr(R^{1/2} K P K^T R^{1/2})$ . The following LMI problem solves for the feedback gain matrix  $K$ .

#### LQR LMI Problem

$$\min_{P, X, Y} Tr(QP) + Tr(X) \tag{2.4}$$

subject to

$$-AP - PA^T + BY + Y^T B^T - W > 0$$

$$\begin{bmatrix} X & R^{1/2} Y \\ Y^T R^{1/2} & P \end{bmatrix} > 0$$

with  $P = P^T$ ,  $X = X^T$ ,  $K = YP^{-1}$ , and  $W > 0$  given.

### 2.2.3 $H_2$ -Norm Minimization For Linear Time Varying Systems

Another variation of the above  $H_2$ -norm minimization problem is to consider a linear time varying (LTV) plant where the time variations are introduced by gain scheduling. Consider the LTV plant described by

$$\begin{aligned}\dot{x} &= A(t)x + B(t)u + w \\ z &= Q^{1/2}(t)x + R^{1/2}(t)u\end{aligned}\tag{2.5}$$

with the state feedback control  $u = -K(t)x$ . The controller design problem is to select the time varying feedback gain matrix  $K(t)$  to minimize the  $H_2$ -norm between  $w$  and  $z$  over a time interval  $[t_{\min}, t_{\max}]$ . The following LMI problem solves for the feedback gain matrix  $K(t)$ .

#### LTV LMI Problem

$$\min_{P(t), X(t), Y(t)} \int Tr(Q(t)P) + Tr(X(t)) dt\tag{2.6}$$

subject to

$$\begin{aligned}\dot{P}(t) - A(t)P(t) - P(t)A^T(t) + B(t)Y(t) + Y^T(t)B^T(t) - W(t) &> 0 \\ \begin{bmatrix} X(t) & R^{1/2}(t)Y(t) \\ Y^T(t)R^{1/2}(t) & P(t) \end{bmatrix} &> 0\end{aligned}$$

with  $P(t) = P^T(t)$ ,  $X(t) = X^T(t)$ ,  $K(t) = Y(t)P^{-1}(t)$ ,  $t_{\min} < t < t_{\max}$ , and  $W(t) > 0$  given.

In addition to solving this LMI problem, the control designer can minimize the  $\|z\|_2$  and keep this norm above a prescribed level. Consider the LTV plant described by

$$\begin{aligned}\dot{x} &= A(t)x + B(t)u + w \\ z &= Q^{1/2}(t)x + R^{1/2}(t)u\end{aligned}$$

with the state feedback control  $u = -K(t)x$ . The controller design problem is to select the time varying feedback gain matrix  $K(t)$  to minimize the  $H_2$ -norm between  $w$  and  $z$  over a time interval keeping the  $\|z\|_2$  above  $\bar{\gamma}(t)$ . The following LMI problem solves for the feedback gain matrix  $K(t)$ .

**LTV LMI Problem For Prescribed Level Of  $\|z\|_2$**

$$\min_{\gamma(t), P(t), X(t), Y(t); \gamma_{\max}} \gamma_{\max} \tag{2.7}$$

subject to

$$\begin{aligned} \gamma(t) - \bar{\gamma}(t) &> 0 \\ \gamma_{\max} - \gamma(t) + \bar{\gamma}(t) &> 0 \\ \gamma_{\max} - \text{Tr}(Q(t)P(t)) - \text{Tr}(X(t)) &> 0 \\ \dot{P}(t) - A(t)P(t) - P(t)A^T(t) + B(t)Y(t) + Y^T(t)B^T(t) - W(t) &> 0 \\ \begin{bmatrix} X(t) & R^{1/2}(t)Y(t) \\ Y^T(t)R^{1/2}(t) & P(t) \end{bmatrix} &> 0 \end{aligned}$$

with  $P(t) = P^T(t)$ ,  $X(t) = X^T(t)$ ,  $K(t) = Y(t)P^{-1}(t)$ ,  $t_{\min} < t < t_{\max}$ ,  $\bar{\gamma}(t) > 0$ , and  $W(t) > 0$  given.

**2.2.4  $H_2$  Controller Design and Simulation Results**

In this section the  $H_2$  LMI controller design problem is applied to the Boeing Tailless Advanced Fighter Aircraft (TAFA) model described in Appendix A. A pitch rate command flight control system was designed using the LMI standard LQR formulation, and for comparison, a robust servomechanism flight control system [7] was also designed.

LQR Plant matrices

$$A = \begin{bmatrix} -4.281534e+00 & 1.022817e+01 & -7.686167e+01 & 0.0 \\ 1.029299e+00 & -1.889328e+00 & 5.527753e-03 & 2.089781e-01 \\ 0.0 & 0.0 & 0.0 & 1.0 \\ 0.0 & 0.0 & -3.457440e+03 & -9.643200e+01 \end{bmatrix}$$



$$B = \begin{bmatrix} 0.0 \\ 0.0 \\ 0.0 \\ 3.457440e+03 \end{bmatrix}$$

The LQR LMI problem is

$$\min_{P,X,Y} Tr(QP) + Tr(X)$$

subject to

$$-AP - PA^T + BY + Y^T B^T - W > 0$$

$$\begin{bmatrix} X & R^{1/2}Y \\ Y^T R^{1/2} & P \end{bmatrix} > 0$$

with  $P = P^T$ ,  $X = X^T$ ,  $K = YP^{-1}$ , and  $W > 0$  given. The resulting LMI controller gains are

$$K_{LMI} = [-2.176814e-01 \quad -4.819290e-02 \quad -9.456374e-02].$$

The Robust Servo feedback gains are

$$K_{RS} = [-2.685933e-01 \quad -5.909616e-02 \quad -1.102195e-01]$$

Figure 2.1 illustrates a step response comparing the two designs. Both flight control designs produce similar responses.

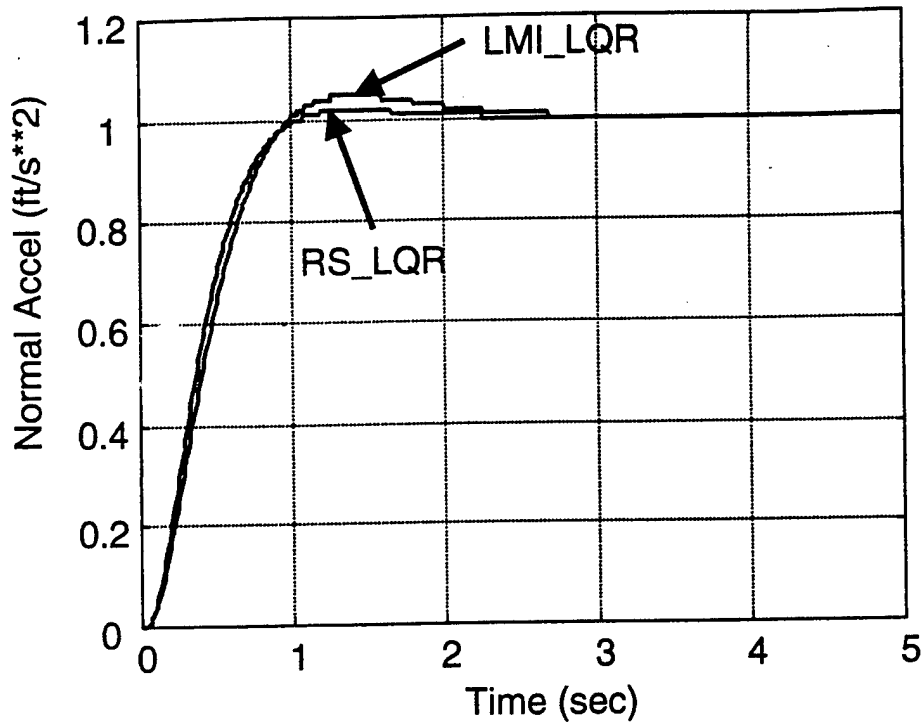


Figure 2.1  $H_2$  Controller Step Acceleration Command Simulation Response

### 2.3 $H_\infty$ Controller Design Using LMIs

In this section LMI problems are formulated for minimizing the  $H_\infty$  norm between an exogenous variable  $w$  and the regulated variable  $z$  applied to a linear time invariant (LTI) systems and for linear time varying systems.

Consider the plant shown in Figure 2.2, described by

$$\begin{aligned} \dot{x} &= Ax + B_1 w + B_2 u \\ z &= C_1 x + D_{11} w + D_{12} u \\ y &= C_2 x + D_{21} w \end{aligned} \tag{2.8}$$

with controller given by

$$\begin{aligned} \dot{x}_k &= A_k x_k + B_k y \\ u &= C_k x_k + D_k y \end{aligned}$$

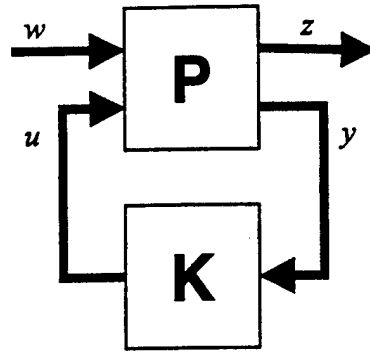


Figure 2.2 Controller Design Model

Substituting for  $y$  in Eq. (2.8) results in

$$\begin{aligned}\dot{x}_k &= A_k x_k + B_k C_2 x + B_k D_{21} w \\ u &= C_k x_k + D_k C_2 x + D_k D_{21} w\end{aligned}$$

Closing the loop with the plant model (Eq. (2.8)) yields

$$\begin{aligned}\dot{x} &= Ax + B_1 w + B_2 (C_k x_k + D_k C_2 x + D_k D_{21} w) \\ \dot{x}_k &= A_k x_k + B_k C_2 x + B_k D_{21} w \\ z &= C_1 x + D_{11} w + D_{12} (C_k x_k + D_k C_2 x + D_k D_{21} w)\end{aligned}\tag{2.9}$$

Expressing Eq. (2.9) in matrix form defines the closed loop system matrices  $(A_{cl}, B_{cl}, C_{cl}, D_{cl})$  as

$$\begin{aligned}\begin{bmatrix} \dot{x} \\ \dot{x}_k \end{bmatrix} &= \underbrace{\begin{bmatrix} A + B_2 D_k C_2 & B_2 C_k \\ B_k C_2 & A_k \end{bmatrix}}_{A_{cl}} \begin{bmatrix} x \\ x_k \end{bmatrix} + \underbrace{\begin{bmatrix} B_1 + B_2 D_k D_{21} \\ B_k D_{21} \end{bmatrix}}_{B_{cl}} w \\ z &= \underbrace{\begin{bmatrix} C_1 + D_{12} D_k C_2 & D_{12} C_k \end{bmatrix}}_{C_{cl}} \begin{bmatrix} x \\ x_k \end{bmatrix} + \underbrace{\begin{bmatrix} D_{11} + D_{12} D_k D_{21} \end{bmatrix}}_{D_{cl}} w\end{aligned}$$

To formulate the controller design problem within the LMI framework we would like to write the closed loop system matrices such that the controller matrix parameters  $(A_k, B_k, C_k, D_k)$  appear affinely in the description of closed loop system. Let

$$\Theta = \begin{bmatrix} A_k & B_k \\ C_k & D_k \end{bmatrix}$$

and let

$$A_0 = \begin{bmatrix} A & 0 \\ 0 & 0 \end{bmatrix} \quad B_0 = \begin{bmatrix} B_1 \\ 0 \end{bmatrix} \quad C_0 = [C_1 \quad 0]$$

$$B = \begin{bmatrix} 0 & B_2 \\ I & 0 \end{bmatrix} \quad C = \begin{bmatrix} 0 & I \\ C_2 & 0 \end{bmatrix} \quad \mathcal{D}_{12} = [0 \quad D_{12}] \quad \mathcal{D}_{21} = \begin{bmatrix} 0 \\ D_{21} \end{bmatrix}$$

Then

$$A_{cl} = A_0 + B\Theta C$$

$$B_{cl} = B_0 + B\Theta \mathcal{D}_{21}$$

$$C_{cl} = C_0 + \mathcal{D}_{12}\Theta C$$

$$D_{cl} = D_{11} + \mathcal{D}_{12}\Theta \mathcal{D}_{21}$$

The fact that the controller parameter matrices appear affinely in the closed loop system is key to using an LMI to solve for the controller that yields internal stability and provides an  $L_2$  gain from  $w$  to  $z$

$$\int z^T z d\tau \leq \frac{1}{\gamma^2} \int w^T w d\tau$$

To proceed, the Bounded Real Lemma can be used to turn the  $H_\infty$  controller design problem into a LMI.

**Lemma 1**

Consider a continuous time transfer function  $T(s)$  (not necessarily minimal) with realization

$T(s) = D + C(sI - A)^{-1}B$ . The following statements are equivalent:

i)  $\|D + C(sI - A)^{-1}B\|_\infty < \gamma$  and  $\text{Re}(\lambda_i(A)) < 0$ .

ii) There exists a symmetric positive definite solution  $X$  to the LMI

$$\begin{bmatrix} A^T X + XA & XB & C^T \\ B^T X & -\gamma I & D^T \\ C & D & -\gamma I \end{bmatrix} < 0.$$

For a proof of this lemma see references [1] and [2]. The above LMI can be shown to be equivalent to the more familiar Algebraic Riccati Inequality by using the following lemma.

**Lemma 2**

The matrix  $\begin{bmatrix} Q & S \\ S^T & R \end{bmatrix} < 0$  if and only if  $R < 0$ , and  $Q - SR^{-1}S^T < 0$ .

**Proof of Lemma 2**

$$\begin{bmatrix} Q & S \\ S^T & R \end{bmatrix} = \begin{bmatrix} I & SR^{-1} \\ 0 & I \end{bmatrix} \begin{bmatrix} Q - SR^{-1}S^T & 0 \\ 0 & R \end{bmatrix} \begin{bmatrix} I & 0 \\ R^{-1}S^T & I \end{bmatrix}$$

Now, consider the LMI stated in condition ii). Partition it as follows

$$\begin{bmatrix} A^T X + XA & XB & \vdots & C^T \\ B^T X & -\gamma I & \vdots & D^T \\ \dots & \dots & \dots & \dots \\ C & D & \vdots & -\gamma I \end{bmatrix} < 0$$

which is equivalent to

$$\begin{bmatrix} A^T X + XA & XB \\ B^T X & -\gamma I \end{bmatrix} - \begin{bmatrix} C^T \\ D^T \end{bmatrix} \frac{1}{-\gamma} [C \ D] < 0.$$

Combining results in

$$\begin{bmatrix} A^T X + XA + \gamma^{-1} C^T C & XB + \gamma^{-1} C^T D \\ B^T X + \gamma^{-1} D^T C & \gamma^{-1} (D^T D - \gamma^2 I) \end{bmatrix} < 0$$

which is equivalent to

$$\bar{\sigma}(D) < \gamma$$

$$A^T X + XA + \gamma^{-1} C^T C + \gamma (XB + \gamma^{-1} C^T D)(\gamma^2 I - D^T D)(B^T X + \gamma^{-1} D^T C) < 0$$

which is the Algebraic Riccati Inequality associated with the Bounded Real Lemma.

Now, consider the description of the closed loop system which is affine in the controller parameter  $\Theta$ . Our approach is to solve a LMI problem to obtain  $X$  and  $\Theta$ . To proceed, consider the following lemma

**Lemma 3**

Given  $\Psi = \Psi^T \in \mathbb{R}^{m \times m}$ , and two matrices  $P$  and  $Q$  of column dimension  $m$ , find a matrix  $\Theta$  such that

$$\Psi + P^T \Theta Q + Q^T \Theta P < 0 \tag{2.10}$$

Denote  $W_P$  and  $W_Q$  as any matrices whose columns form a basis for the null space of  $P$  and  $Q$ , respectively. Then the inequality in Eq. (2.10) is solvable for  $\Theta$  if and only if

$$\begin{aligned} W_P^T \Psi W_P &< 0 \\ W_Q^T \Psi W_Q &< 0 \end{aligned}$$

For a proof of this lemma see references [2] and [3]. By combining Lemma 1 and Lemma 3, we obtain the following theorem which states the necessary and sufficient conditions for the existence of an  $H_\infty$  (suboptimal) controller.

**Theorem 1**

Consider the proper, minimal plant  $P(s)$ . Define

$$\begin{aligned} \mathcal{P} &= \begin{bmatrix} \mathcal{B} & 0 & \mathcal{D}_{12}^T \end{bmatrix} \\ \mathcal{Q} &= \begin{bmatrix} \mathcal{C} & \mathcal{D}_{21} & 0 \end{bmatrix} \end{aligned}$$

and let  $W_P$  and  $W_Q$  be two matrices whose columns span the null spaces of  $\mathcal{P}$  and  $\mathcal{Q}$ , respectively. Then the  $H_\infty$  controller can be found if and only if there exists some positive definite matrix  $X_d$  such that

$$\begin{aligned} W_P^T \Phi_{X_d} W_P &< 0 \\ W_Q^T \Psi_{X_d} W_Q &< 0 \end{aligned}$$

where

$$\Phi_{X_d} = \begin{bmatrix} A_0 X_{cl}^{-1} + X_{cl}^{-1} A_0^T & B_0 & X_{cl}^{-1} C_0^T \\ B_0^T & -\gamma I & D_{11}^T \\ C_0 X_{cl}^{-1} & D_{11} & -\gamma I \end{bmatrix}$$

$$\Psi_{X_d} = \begin{bmatrix} A_0^T X_{cl} + X_{cl} A_0 & X_{cl} B_0 & C_0^T \\ B_0^T X_{cl} & -\gamma I & D_{11}^T \\ C_0 & D_{11} & -\gamma I \end{bmatrix}$$

Proof: From Lemma 1, the controller  $K(s) = D_k + C_k (sI - A_k)^{-1} B_k$  is an  $H_\infty$  controller if and only if the LMI

$$\begin{bmatrix} A_{cl}^T X_{cl} + X_{cl} A_{cl} & X_{cl} B_{cl} & C_{cl}^T \\ B_{cl}^T X_{cl} & -\gamma I & D_{cl}^T \\ C_{cl} & D_{cl} & -\gamma I \end{bmatrix} < 0$$

holds for  $X_{cl} < 0$ . Substituting for  $(A_{cl}, B_{cl}, C_{cl}, D_{cl})$  gives

$$\begin{bmatrix} A_0^T X_{cl} + X_{cl} A_0 & X_{cl} B_0 & C_0^T \\ B_0^T X_{cl} & -\gamma I & D_{11}^T \\ C_0 & D_{11} & -\gamma I \end{bmatrix} + \begin{bmatrix} C^T \Theta^T B X_{cl} + X_{cl} A_0 & 0 & C^T \Theta^T D_{12}^T \\ D_{21}^T \Theta B^T X_{cl} & 0 & D_{21}^T \Theta^T D_{12}^T \\ 0 & 0 & 0 \end{bmatrix} + \begin{bmatrix} X_{cl} B \Theta C & X_{cl} B \Theta C & 0 \\ 0 & 0 & 0 \\ D_{12} \Theta C & D_{12} \Theta D_{21} & 0 \end{bmatrix} < 0$$

$$\underbrace{\begin{bmatrix} A_0^T X_{cl} + X_{cl} A_0 & X_{cl} B_0 & C_0^T \\ B_0^T X_{cl} & -\gamma I & D_{11}^T \\ C_0 & D_{11} & -\gamma I \end{bmatrix}}_{\Psi_{X_d}} + \underbrace{\begin{bmatrix} C^T \\ 0 \end{bmatrix}}_{\mathcal{Q}^T} \underbrace{\begin{bmatrix} B^T X_{cl} & 0 & D_{12}^T \end{bmatrix}}_{\mathcal{P}_{X_d}} + \underbrace{\begin{bmatrix} X_{cl} B \\ 0 \\ D_{12} \end{bmatrix}}_{\mathcal{P}_{X_d}^T} \underbrace{\Theta \begin{bmatrix} C & D_{21} & 0 \end{bmatrix}}_{\mathcal{Q}} < 0$$

$$\Psi_{X_d} + Q^T \Theta^T P_{X_d} + P_{X_d}^T \Theta Q < 0 \quad (2.11)$$

Note that  $P_{X_d} = \begin{bmatrix} B^T X_d & 0 & D_{12}^T \end{bmatrix}$  where  $P = \begin{bmatrix} B & 0 & D_{12}^T \end{bmatrix}$ . Thus,

$$P_{X_d} = P \begin{bmatrix} X_d & 0 & 0 \\ 0 & I & 0 \\ 0 & 0 & O \end{bmatrix}.$$

The left null space of  $P$  is related to the left nullspace of  $P_{X_d}$  by

$$W_{P_{X_d}} = \begin{bmatrix} X_d^{-1} & 0 & 0 \\ 0 & I & 0 \\ 0 & 0 & O \end{bmatrix} W_P.$$

Now, using Lemma 3, we can eliminate  $\Theta$  from Eq. (2.11) obtaining

$$\underbrace{W_P^T \begin{bmatrix} X_d^{-1} & 0 & 0 \\ 0 & I & 0 \\ 0 & 0 & O \end{bmatrix} \Psi_{X_d} \begin{bmatrix} X_d^{-1} & 0 & 0 \\ 0 & I & 0 \\ 0 & 0 & O \end{bmatrix} W_P}_{\Phi_{X_d}} < 0$$

$$W_P^T \Phi_{X_d} W_P < 0$$

and

$$W_Q^T \Psi_{X_d} W_Q < 0. \blacksquare$$

Theorem 1 says that the set of  $H_\infty$  controllers is non-empty if and only if there exists a matrix  $X_d$  satisfying  $W_P^T \Phi_{X_d} W_P < 0$  and  $W_Q^T \Psi_{X_d} W_Q < 0$ . This characterization involves both  $X_d$  and its inverse  $X_d^{-1}$ . These conditions can be reduced to the more familiar  $H_\infty$  Riccati equations as follows.

**Theorem 2**

Consider the proper, minimal, plant  $P(s)$  of order  $n$ . Let  $W_{12}$  and  $W_{21}$  denote null spaces of  $(I - D_{12}^+ D_{12})B_2^T$  and  $(I - D_{21} D_{21}^+)C_2$ , respectively. Then, the  $H_\infty$  controller (for fixed  $\gamma$ ) is solvable if and only if

i)  $\max\{\bar{\sigma}(\hat{D}_{11}), \bar{\sigma}(\tilde{D}_{11})\} < \gamma$

ii) There exists symmetric positive definite matrices  $R$  and  $S$  such that

$$W_{12}^T \left( \hat{A}R + R\hat{A}^T - \gamma \hat{B}_2 \hat{B}_2^T + \begin{bmatrix} \hat{C}_1 R \\ \hat{B}_1^T \end{bmatrix}^T \begin{bmatrix} \gamma I & -\hat{D}_{11} \\ -\hat{D}_{11}^T & \gamma I \end{bmatrix} \begin{bmatrix} \hat{C}_1 R \\ \hat{B}_1^T \end{bmatrix} \right) W_{12} < 0 \quad (2.12)$$

$$W_{21}^T \left( \tilde{A}^T S + S\tilde{A} - \gamma \tilde{C}_2^T \tilde{C}_2 + \begin{bmatrix} \tilde{B}_1^T S \\ \tilde{C}_1 \end{bmatrix}^T \begin{bmatrix} \gamma I & -\tilde{D}_{11}^T \\ -\tilde{D}_{11} & \gamma I \end{bmatrix} \begin{bmatrix} \tilde{B}_1^T S \\ \tilde{C}_1 \end{bmatrix} \right) W_{21} < 0 \quad (2.13)$$

$$\lambda_{\min}(RS) \geq 1$$

where

$$\hat{B}_2 = B_2 D_{12}^+ \quad \hat{A} = A - \hat{B}_2 C_1 \quad \hat{B}_1 = B_1 - \hat{B}_2 D_{11}$$

$$\hat{C}_1 = (I - D_{12} D_{12}^+) C_1 \quad \hat{D}_{11} = (I - D_{12} D_{12}^+) D_{11}$$

$$\tilde{C}_2 = D_{12}^+ C_2 \quad \tilde{A} = A - B_1 \tilde{C}_2 \quad \tilde{C}_1 = C_1 - D_{11} \tilde{C}_2$$

$$\tilde{B}_1 = B_1 (I - D_{21}^+ D_{21}) \quad \tilde{D}_{11} = D_{11} (I - D_{21}^+ D_{21})$$

and  $\text{rank}(I - RS) \leq k$  (where  $k$  is the order of the controller). Using  $X = \lambda R^{-1}$  and  $Y = \gamma S^{-1}$ , along with the simplifying assumptions

$$D_{11} = 0 \quad D_{12}^T [D_{12} \quad C_1] = [I \quad 0] \quad D_{21} [D_{21}^T \quad B_1^T] = [I \quad 0]$$

the above Algebraic Riccati Inequalities (ARIs) can be written as

$$\begin{aligned} A^T X + X A + X(\gamma^{-2} B_1 B_1^T - B_2 B_2^T) X + C_1^T C_1 &< 0 \\ A Y + Y A^T + Y(\gamma^{-2} C_1^T C_1 - C_2^T C_2) Y + B_1 B_1^T &< 0 \\ X > 0 \quad Y > 0 \quad \rho(XY) &\leq \gamma^2 \end{aligned}$$

which are the more familiar  $H_\infty$  Riccati expressions.

The proof of Theorem 2 is based upon Theorem 1 and introduces notation and algebra common to much of the published literature on LMIs.

Proof: From Theorem 1 the set of  $H_\infty$  controllers is non empty if and only if  $W_p^T \Phi_{x_d} W_p < 0$  and  $W_q^T \Psi_{x_d} W_q < 0$  for some  $X_{cl} > 0$  of dimension  $(n+k) \times (n+k)$  ( $k$  is the order of the controller). To express these inequalities in terms of the plant state space model, partition  $X_{cl}$  and  $X_{cl}^{-1}$  as

$$X_{cl} = \begin{bmatrix} S & N \\ N^T & * \end{bmatrix} \text{ and } X_{cl}^{-1} = \begin{bmatrix} R & M \\ M^T & * \end{bmatrix}.$$

Substituting these into  $\Phi_{x_d}$  yields

$$\Phi_{x_d} = \begin{bmatrix} AR + RA^T & AM & B_1 & RC_1^T \\ M^T A^T & 0 & 0 & M^T C_1^T \\ B_1^T & 0 & -\gamma I & D_{11}^T \\ C_1 R & C_1 M & D_{11} & -\gamma I \end{bmatrix}$$

with  $\mathcal{P} = \begin{bmatrix} 0 & I_k & 0 & 0 \\ B_2^T & 0 & 0 & D_{12}^T \end{bmatrix}$ . The nullspace of  $\mathcal{P}$ ,  $\ker(\mathcal{P})$ , has the form

$$W_p = \begin{bmatrix} W_1 & 0 \\ 0 & 0 \\ 0 & I \\ W_2 & 0 \end{bmatrix}$$

where  $\ker(\mathcal{P}) = \begin{bmatrix} W_1 \\ W_2 \end{bmatrix}$ , i.e.,  $\begin{bmatrix} B_2^T & D_{12}^T \end{bmatrix} \begin{bmatrix} W_1 \\ W_2 \end{bmatrix} = \begin{bmatrix} 0 & 0 \end{bmatrix}$ . Noting that the second row of  $W_{\mathcal{P}}$  is zero, the condition  $W_{\mathcal{P}}^T \Phi_{x_d} W_{\mathcal{P}} < 0$  reduces to

$$\begin{bmatrix} W_1 & 0 \\ 0 & I \\ W_2 & 0 \end{bmatrix}^T \begin{bmatrix} AR + RA^T & B_1 & RC_1^T \\ B_1^T & -\gamma I & D_{11}^T \\ C_1 R & D_{11} & -\gamma I \end{bmatrix} \begin{bmatrix} W_1 & 0 \\ 0 & I \\ W_2 & 0 \end{bmatrix} < 0$$

Re-arranging results in

$$\begin{bmatrix} \ker(R) & 0 \\ 0 & I \end{bmatrix}^T \left[ \begin{array}{cc|c} AR + RA^T & RC_1^T & B_1 \\ C_1 R & -\gamma I & D_{11} \\ \hline B_1^T & D_{11}^T & -\gamma I \end{array} \right] \begin{bmatrix} \ker(R) & 0 \\ 0 & I \end{bmatrix} < 0$$

The next step consists of expressing  $\ker(R)$  in terms of the plant matrices.

$$\ker(R) = \begin{bmatrix} W_{12} & 0 \\ -\hat{B}_2^T W_{12} & U_{12} \end{bmatrix} = \begin{bmatrix} I_n & 0 \\ -\hat{B}_2^T & U_{12} \end{bmatrix} \begin{bmatrix} W_{12} & 0 \\ 0 & I \end{bmatrix}$$

where  $\hat{B}_2 = B_2 D_{12}^+$ , then  $\hat{B}_2 U_{12} = B_2 D_{12}^+ U_{12} = 0$ . Next, we see that

$$\begin{aligned} \begin{bmatrix} B_2^T & D_{12}^T \end{bmatrix} \ker(R) &= \begin{bmatrix} B_2^T & D_{12}^T \end{bmatrix} \begin{bmatrix} I_n & 0 \\ -\hat{B}_2^T & U_{12} \end{bmatrix} \begin{bmatrix} W_{12} & 0 \\ 0 & I \end{bmatrix} \\ &= \begin{bmatrix} B_2^T - D_{12}^T \hat{B}_2^T & D_{12}^T U_{12} \end{bmatrix} \begin{bmatrix} W_{12} & 0 \\ 0 & I \end{bmatrix} \\ &= \begin{bmatrix} B_2^T - D_{12}^T D_{12}^{+T} \hat{B}_2^T & D_{12}^T U_{12} \end{bmatrix} \begin{bmatrix} W_{12} & 0 \\ 0 & I \end{bmatrix} \\ &= \begin{bmatrix} (I - D_{12}^T D_{12}^{+T}) B_2^T & D_{12}^T U_{12} \end{bmatrix} \begin{bmatrix} W_{12} & 0 \\ 0 & I \end{bmatrix} \\ &= \begin{bmatrix} 0 & 0 \end{bmatrix} \end{aligned}$$

Substituting for  $\ker(R)$  gives

$$\left[ \begin{array}{cc|c} W_{12} & 0 & 0 \\ -\hat{B}_2^T W_{12} & U_{12} & 0 \\ \hline 0 & 0 & I \end{array} \right]^T \left[ \begin{array}{cc|c} AR+RA^T & RC_1^T & B_1 \\ \hline C_1 R & -\gamma I & D_{11} \\ B_1^T & D_{11}^T & -\gamma I \end{array} \right] \left[ \begin{array}{cc|c} W_{12} & 0 & 0 \\ -\hat{B}_2^T W_{12} & U_{12} & 0 \\ \hline 0 & 0 & I \end{array} \right] < 0$$

Combining terms results in

$$\left[ \begin{array}{ccc} W_{12}^T (\hat{A}R + R\hat{A}^T - \gamma \hat{B}_2 \hat{B}_2^T) W_{12} & W_{12}^T R C_1^T U_{12} & W_{12}^T B_1 \\ U_{12}^T C_1 R W_{12} & -\gamma U_{12}^T U_{12} & U_{12}^T D_{11} \\ B_1^T W_{12} & D_{11}^T U_{12} & -\gamma I \end{array} \right] < 0$$

Further simplification can be made by using  $U_{12} U_{12}^T = I - D_{12} D_{12}^*$ , resulting in

$$\left[ \begin{array}{ccc} W_{12}^T (\hat{A}R + R\hat{A}^T - \gamma \hat{B}_2 \hat{B}_2^T) W_{12} & W_{12}^T R \hat{C}_1^T & W_{12}^T \hat{B}_1 \\ \hat{C}_1 R W_{12} & -\gamma I & \hat{D}_{11} \\ B_1^T W_{12} & D_{11}^T & -\gamma I \end{array} \right] < 0$$

which is equivalent to Eq. (2.12). A similar proof is constructed for Eq. (2.13). ■

The following sections summarize  $H_\infty$  controller design formulas, followed by design results applying the  $H_\infty$  LMI controller to the Boeing TAFA aircraft.

### 2.3.1 State Feedback ARE $H_\infty$ Controller Formulas

The  $H_\infty$  controller formulas presented in this section solve an algebraic Riccati Equation (ARE) formulas to yield a state feedback control  $u = -Kx$ . Consider the following LTI plant

$$\begin{aligned} \dot{x} &= Ax + B_1 w + B_2 u \\ z &= C_1 x + D_{11} w + D_{12} u \end{aligned}$$

The control is obtained by solving the ARE for  $P$

$$\tilde{A}^T P + P \tilde{A} + \tilde{Q} - P \tilde{R} P = 0. \quad (2.14)$$

The feedback gain matrix is

$$K = (R_{11}B_2^T + R_{12}B_1^T)P + (R_{11}D_{12}^T + R_{12}D_{11}^T)C_1 \quad (2.15)$$

where

$$\begin{aligned} R_{12} &= -D^+ D_{11} Z & D^+ &= D_{12}^{-1} & \hat{B}_1 &= B_1 - \hat{B}_2 D_{11} \\ R_{11} &= D^+ D^{*T} + R_{12} Z^{-1} R_{12}^T & \hat{B}_2 &= B_2 D^+ & U &= I - D_{12} D^+ \\ & & \hat{A} &= A - \hat{B}_2 C_1 & \hat{C}_1 &= U C_1 \\ \hat{D}_{11} &= U D_{11} & \tilde{Q} &= \hat{C}_1^T (I - \hat{D}_{11} Z \hat{D}_{11}^T) \hat{C}_1 \\ Z^{-1} &= \hat{D}_{11}^{-1} \hat{D}_{11} - \gamma^2 I & \tilde{R} &= \hat{B}_2 \hat{B}_2^T + \hat{B}_1 Z \hat{B}_1^T \\ \tilde{A} &= \hat{A} - \hat{B}_1 Z \hat{D}_{11}^T \hat{C}_1 \end{aligned}$$

### 2.3.2 $H_\infty$ Controller LMI Problem

The LMI problem summarized here solves for the optimal  $\gamma$  and forms the state feedback control  $u = -Kx$ . This problem is similar to the LMI controller design problem posed by Gahinet and Apkarian in [2]. This problem set up is applicable to extensions made in applying LMIs to gain scheduled systems.

Consider the LTI plant described by

$$\begin{aligned} \dot{x} &= Ax + B_1 w + B_2 u \\ z &= C_1 x + D_{11} w + D_{12} u \end{aligned} \quad (2.16)$$

The controller design problem is to select the feedback gain matrix  $K$  to minimize the  $H_\infty$ -norm between  $w$  and  $z$ .

### $H_\infty$ Controller LMI Problem

$$\min_{R, \gamma} \gamma \quad (2.17)$$

subject to

$$\begin{bmatrix} -\hat{A}R - R\hat{A}^T + \gamma \hat{B}_2 \hat{B}_2^T & -R\hat{C}_1^T & -\hat{B}_1 \\ -\hat{C}_1 R & \gamma I_{n_r} & -\hat{D}_{11} \\ -\hat{B}_1^T & -\hat{D}_{11}^T & \gamma I_{n_w} \end{bmatrix} > 0$$

$R > 0$

$$K = (R_{11} B_2^T + R_{12} B_1^T) R + (R_{11} D_{12}^T + R_{12} D_{11}^T) C_1$$

with

$$\begin{aligned} R_{12} &= -D^+ D_{11} Z & D^+ &= D_{12}^{-1} & \hat{B}_1 &= B_1 - \hat{B}_2 D_{11} \\ R_{11} &= D^+ D^{+T} + R_{12} Z^{-1} R_{12}^T & \hat{B}_2 &= B_2 D^+ & U &= I - D_{12} D^+ \\ & & \hat{A} &= A - \hat{B}_2 C_1 & \hat{C}_1 &= U C_1 \end{aligned}$$

$$\begin{aligned} \hat{D}_{11} &= U D_{11} \\ Z^{-1} &= \hat{D}_{11}^{-1} \hat{D}_{11} - \gamma^2 I \end{aligned}$$

Consider the following graphic illustrating the optimization software's convergence to the optimal  $\gamma$ .

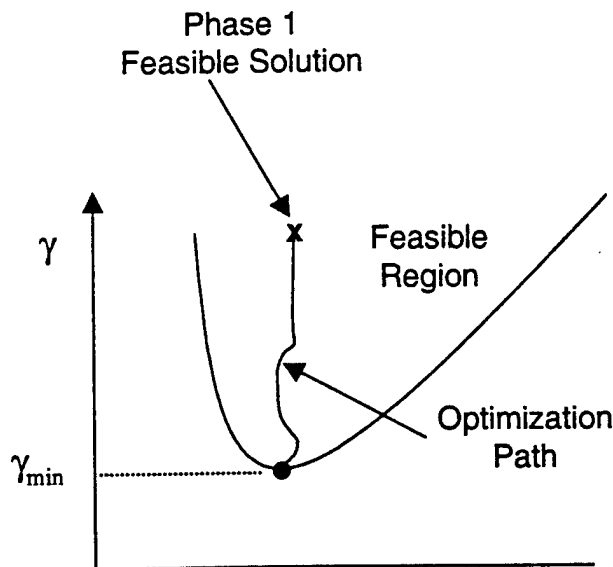


Figure 2.3  $H_\infty$  Controller LMI  $\gamma$  Optimization

The LMI optimization software begins by finding a feasible solution within the feasible region, denoted by  $\mathbf{x}$  in Figure 2.3, and then converges to the optimal  $\gamma_{\min}$ . As  $\gamma$  approaches  $\gamma_{\min}$  this often leads to ill conditioning in the  $H_{\infty}$  problem, where very small numerical changes in  $\gamma$  produce very large changes in the magnitude of the feedback gains.  $H_{\infty}$  practitioners [4] then back off on the numerical value for  $\gamma$ , making it larger, thus making the feedback gains reasonable (for implementation) leading to a sub-optimal control. The next LMI problem setup addresses this fact within the LMI framework.

### 2.3.3 $H_{\infty}$ Controller LMI Problem With Lower Bound Constraint

The LMI problem summarized here solves for a sub-optimal  $\gamma$  along the optimization path (shown in Figure 2.3) and forms the state feedback control  $u = -Kx$ . Consider the LTI plant described by

$$\begin{aligned} \dot{x} &= Ax + B_1 w + B_2 u \\ z &= C_1 x + D_{11} w + D_{12} u \end{aligned} \tag{2.18}$$

The controller design problem is to select the feedback gain matrix  $K$  to minimize the  $H_{\infty}$ -norm between  $w$  and  $z$ .

#### $H_{\infty}$ Controller LMI Problem

$$\min_{R, \gamma} \gamma \tag{2.19}$$

subject to

$$\begin{bmatrix} -\hat{A}R - R\hat{A}^T + \gamma\hat{B}_2\hat{B}_2^T & -R\hat{C}_1^T & -\hat{B}_1 \\ -\hat{C}_1 R & \gamma I_{n_z} & -\hat{D}_{11} \\ -\hat{B}_1^T & -\hat{D}_{11}^T & \gamma I_{n_w} \end{bmatrix} > 0$$

$$R > 0$$

$$\gamma - \bar{\gamma} > 0$$

$$K = (R_{11}B_2^T + R_{12}B_1^T)R + (R_{11}D_{12}^T + R_{12}D_{11}^T)C_1$$

with

$$\begin{aligned}
 R_{12} &= -D^+ D_{11} Z & D^+ &= D_{12}^{-1} & \hat{B}_1 &= B_1 - \hat{B}_2 D_{11} \\
 R_{11} &= D^+ D^{+T} + R_{12} Z^{-1} R_{12}^T & \hat{B}_2 &= B_2 D^+ & U &= I - D_{12} D^+ \\
 & & \hat{A} &= A - \hat{B}_2 C_1 & \hat{C}_1 &= U C_1 \\
 \\
 \hat{D}_{11} &= U D_{11} \\
 Z^{-1} &= \hat{D}_{11}^{-1} \hat{D}_{11} - \gamma^2 I
 \end{aligned}$$

and  $\bar{\gamma} > 0$  given as the desired sub-optimal gain.

Figure 2.4 illustrates the solution from this LMI problem. In this LMI problem the software minimizes  $\gamma$  along the optimization path subject to the constraint that  $\gamma - \bar{\gamma} > 0$ .

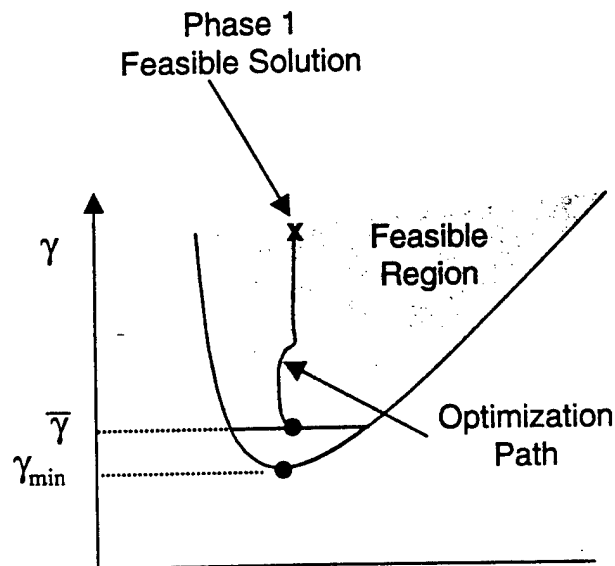


Figure 2.4  $H_\infty$  Controller LMI  $\gamma$  Optimization With Lower Bound Constraint

Here the optimization software is constrained in the minimization of  $\gamma$  to keep  $\gamma - \bar{\gamma} > 0$ . The resulting controller using this design has feedback gains that are much smaller in size, and as a result does not amplify sensor noise. We refer to this as gain conditioning.

### 2.3.4 Methods Used To Improve Numerical Accuracy And Conditioning

This section discusses an additional constraint that was added to the LMI problem in order to satisfy the LMI constraint in Eq. (2.17) to within an  $\epsilon I$ , and a weighting matrix added to improve numerical conditioning in solving for the  $H_\infty$  controller.

Let

$$L(\gamma, R) = \begin{bmatrix} -\hat{A}R - R\hat{A}^T + \gamma\hat{B}_2\hat{B}_2^T & -R\hat{C}_1^T & -\hat{B}_1 \\ -\hat{C}_1R & \gamma I_{n_2} & -\hat{D}_{11} \\ -\hat{B}_1^T & -\hat{D}_{11}^T & \gamma I_{n_1} \end{bmatrix}.$$

The LMI problem in Eq. (2.17) uses the constraint that  $L(\gamma, R) > 0$ . Figure 2.5 illustrates bounding  $L(\gamma, R) > 0$  by a hypersphere of radius  $\epsilon$ , i.e.  $0 < L(\gamma, R) < \epsilon I$ .

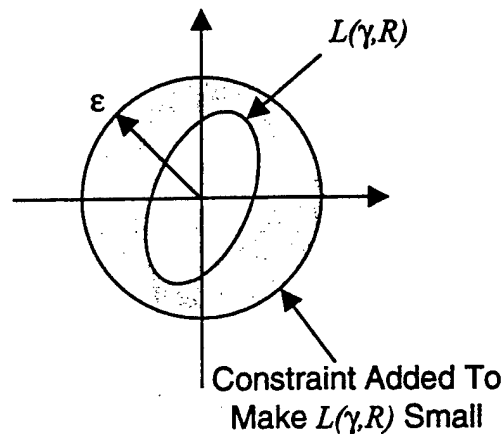


Figure 2.5 Bounding  $L(\gamma, R)$  With  $\epsilon I$

When using an ARE (Eq. (2.14)) to form the control gain matrix one can put the solution matrix  $P$  back into the ARE to see how well the ARE is satisfied (usually the ARE produces a matrix that is not zero). To improve how well the inequality is satisfied, we investigated constraining  $L(\gamma, R)$  by adding  $0 < L(\gamma, R) < \epsilon I$  as an additional constraint in the LMI problem. We found this had no effect on improving how well the inequality was satisfied.

In addition to investigating the above constraint, we also examined various scaling matrices to eliminate ill conditioning in the  $R$  matrix. The scaling was added to the LMI constraint in Eq. (2.17) as  $GL(\gamma, R)G^T > 0$ . Eigenvalues of the  $R$  matrix were examined to scale the matrix to improve the condition number. Like before, we found that this had no effect on the numerical accuracy in satisfying the LMI constraints.

### 2.3.5 An $H_\infty$ Controller LMI Problem With Gain Conditioning

The LMI problem summarized here optimizes  $\gamma$ , while at the same time incorporates a lower bound constraint on  $\gamma$  by using a bias  $\Delta\gamma$ . (This LMI problem incorporates gain conditioning in the LMI problem setup as discussed previously in Section 2.3.3.

Consider the LTI plant described by

$$\begin{aligned} \dot{x} &= Ax + B_1 w + B_2 u \\ z &= C_1 x + D_{11} w + D_{12} u \end{aligned} \tag{2.20}$$

The controller design problem is to select the feedback gain matrix  $K$  to minimize the  $H_\infty$ -norm between  $w$  and  $z$ .

#### $H_\infty$ Controller LMI Problem

$$\min_{R, R_m, \gamma} \gamma \tag{2.21}$$

subject to

$$\begin{aligned} & \begin{bmatrix} -\hat{A}R - R\hat{A}^T + \gamma\hat{B}_2\hat{B}_2^T & -R\hat{C}_1^T & -\hat{B}_1 \\ -\hat{C}_1 R & \gamma I_{n_z} & -\hat{D}_{11} \\ -\hat{B}_1^T & -\hat{D}_{11}^T & \gamma I_{n_w} \end{bmatrix} > 0 \\ & R > 0 \\ & \begin{bmatrix} -\hat{A}R_m - R_m\hat{A}^T + \Delta\gamma\hat{B}_2\hat{B}_2^T & -R_m\hat{C}_1^T & -\hat{B}_1 \\ -\hat{C}_1 R_m & \Delta\gamma I_{n_z} & -\hat{D}_{11} \\ -\hat{B}_1^T & -\hat{D}_{11}^T & \Delta\gamma I_{n_w} \end{bmatrix} > 0 \\ & \gamma - \bar{\gamma} = \Delta\gamma \end{aligned}$$

$$K = (R_{11}B_2^T + R_{12}B_1^T)R_m + (R_{11}D_{12}^T + R_{12}D_{11}^T)C_1$$

with

$$\begin{aligned}
 R_{12} &= -D^+ D_{11} Z & D^+ &= D_{12}^{-1} & \hat{B}_1 &= B_1 - \hat{B}_2 D_{11} \\
 R_{11} &= D^+ D^{+T} + R_{12} Z^{-1} R_{12}^T & \hat{B}_2 &= B_2 D^+ & U &= I - D_{12} D^+ \\
 & & \hat{A} &= A - \hat{B}_2 C_1 & \hat{C}_1 &= U C_1 \\
 \\ 
 \hat{D}_{11} &= U D_{11} \\
 Z^{-1} &= \hat{D}_{11}^{-1} \hat{D}_{11} - \gamma^2 I
 \end{aligned}$$

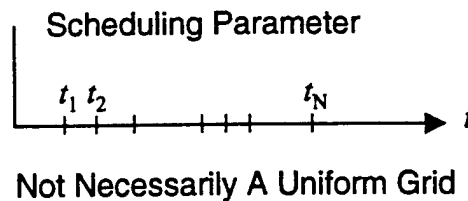
and  $\bar{\gamma} > 0$  given.

Note that the feedback gain matrix  $K$  is calculated using the matrix  $R_m$ . This problem set up accomplishes the goal of making the feedback gain magnitudes reasonable. Unfortunately, it makes the LMI problem size very large.

### 2.3.6 $H_\infty$ Controller LMI Problem For LTV Systems Caused By Gain Scheduling

In Packard and Becker [5,6] the problem of designing gain scheduled  $H_\infty$  controllers was addressed. In this work the problem was made simple by assuming that a constant global  $\gamma$  could be found that would apply over the entire flight envelope. This is a poor assumption for flight control systems because the desired dynamics/response (for an aircraft or missile) greatly varies with speed and altitude.

Consider the problem of scheduling the control gain matrix with a parameter  $t$  as follows:



This requires gridding the parameter space. At each grid point a  $H_\infty$  controller is designed using an optimal control ( $\gamma_{\min}$ ) and solution matrix  $R$  good at each grid point. In the implementation the control is no longer optimal because of  $\gamma$  and  $\dot{R}$  variations caused by the scheduling. From the LTI case, Eq. (2.17),  $R = \gamma P^{-1}$  with  $\dot{R} = 0$ . Now,

$$\begin{aligned}\dot{R} &= \dot{\gamma} P^{-1} + \gamma \frac{d}{dt}(P^{-1}) \\ &= \dot{\gamma} P^{-1} + \gamma P^{-1} \dot{P} P^{-1}\end{aligned}$$

This leads to

$$\begin{aligned}\gamma P^{-1} \dot{P} P^{-1} &= \dot{\gamma} P^{-1} - \dot{R} \\ &= \frac{\dot{\gamma}}{\gamma} R - \dot{R}\end{aligned}\tag{2.22}$$

The LMI problem of calculating the optimal control for linear time varying systems requires including the variations due to the scheduling. This leads to the following LMI problem:

### $H_\infty$ Controller LMI Problem

$$\min_{R, \gamma} \gamma\tag{2.23}$$

subject to

$$\begin{bmatrix} \dot{R} - \frac{\dot{\gamma}}{\gamma} R - \hat{A}R - R\hat{A}^T + \gamma \hat{B}_2 \hat{B}_2^T & -R\hat{C}_1^T & -\hat{B}_1 \\ -\hat{C}_1 R & \gamma I_{n_r} & -\hat{D}_{11} \\ -\hat{B}_1^T & -\hat{D}_{11}^T & \gamma I_{n_r} \end{bmatrix} > 0\tag{2.24}$$

$$R > 0$$

$$K = (R_{11} B_2^T + R_{12} B_1^T) R + (R_{11} D_{12}^T + R_{12} D_{11}^T) C_1$$

with

$$\begin{aligned}R_{12} &= -D^+ D_{11} Z & D^+ &= D_{12}^{-1} & \hat{B}_1 &= B_1 - \hat{B}_2 D_{11} \\ R_{11} &= D^+ D^{+T} + R_{12} Z^{-1} R_{12}^T & \hat{B}_2 &= B_2 D^+ & U &= I - D_{12} D^+ \\ & & \hat{A} &= A - \hat{B}_2 C_1 & \hat{C}_1 &= U C_1\end{aligned}$$

$$\begin{aligned}\hat{D}_{11} &= U D_{11} \\ Z^{-1} &= \hat{D}_{11}^{-1} \hat{D}_{11} - \gamma^2 I\end{aligned}$$

In Packard [5,6] the  $\dot{\gamma}$  term in Eq. (2.24) is assumed to be zero because  $\gamma$  is global, and then basis functions are used to approximate  $\dot{R}$ . This simplifies the problem. In this research this term is included.

In aircraft and missile applications, the following process is recommended for developing flight control designs. First, develop point designs over the flight envelope by gridding the scheduling parameter space. Next, fit a surface to the resulting optimal  $\gamma$  designed at each discrete point as shown in Figure 2.6

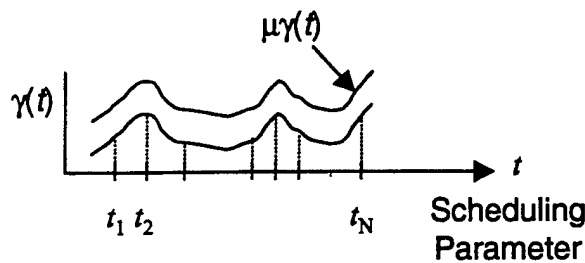


Figure 2.6 Surface Fit To Optimal  $\gamma$

This surface models the relative “size” of the  $\gamma$ ’s, and the variations caused by the scheduling parameters. Next, scale this surface by the scalar parameter  $\mu$ , also shown in Figure 2.6. Now, use polynomials as basis functions to represent  $R$  and  $\gamma$  as follows ( $\alpha$  is the scheduling variable):

$$R = R_0 + R_1\alpha + R_2\alpha^2 + \dots + R_5\alpha^5$$

$$\dot{R} = R_1 + 2R_2\alpha + \dots + 5R_5\alpha^4$$

$$\gamma = \gamma_0 + \gamma_1\alpha + \gamma_2\alpha^2$$

$$\dot{\gamma} = \gamma_1 + 2\gamma_2\alpha$$

The LMI problem becomes

$$\min_{R_0, R_1, R_2, \dots, R_5, \mu} \hat{\gamma} \tag{2.25}$$

subject to

$$\begin{bmatrix} \dot{R} - \frac{\hat{\gamma}}{\gamma} R - \hat{A}R - R\hat{A}^T + \hat{\gamma}\hat{B}_2\hat{B}_2^T & -R\hat{C}_1^T & -\hat{B}_1 \\ -\hat{C}_1 R & \hat{\gamma}I_{n_z} & -\hat{D}_{11} \\ -\hat{B}_1^T & -\hat{D}_{11}^T & \hat{\gamma}I_{n_z} \end{bmatrix} > 0 \quad (2.26)$$

$$R > 0$$

$$K(t) = (R_{11}B_2^T + R_{12}B_1^T)R + (R_{11}D_{12}^T + R_{12}D_{11}^T)C_1$$

Now the LMI optimization variables are  $\mu$  and  $R_0, R_1, R_2, \dots, R_5$ . The term  $\frac{\hat{\gamma}}{\gamma}$  in Eq. (2.26) is now a known function, capturing the variations introduced by the flight envelope.

### 2.3.7 $H_\infty$ Controller Design and Simulation Results

In this section a pitch rate command flight control system was designed using the  $H_\infty$  LMI controller design problem stated in Section 2.3.2. The design problem was applied to the Boeing Tailless Advanced Fighter Aircraft (TAFA) model described in Appendix A. For comparison, the standard ARE approach using  $\gamma$ -iteration was used to design a  $H_\infty$  flight control system (presented in Section 2.3.1). The design results showed that both controllers performed the same.

Plant matrices

$$A = \begin{bmatrix} -4.281534e+00 & 1.022817e+01 & -7.686167e+01 & 0.0 & 0.0 & 0.0 \\ 1.029299e+00 & -1.889328e+00 & 5.527753e-03 & 2.089781e-01 & 0.0 & 0.0 \\ 0.0 & 0.0 & 0.0 & 1.0 & 0.0 & 0.0 \\ 0.0 & 0.0 & -3.457440e+03 & -9.643200e+01 & 0.0 & 0.0 \\ -1.354691e+00 & 0.0 & 0.0 & 0.0 & -1.275106e-03 & 0.0 \\ 1.507771e+03 & 0.0 & 0.0 & 0.0 & 0.0 & 4.018092e+02 \end{bmatrix}$$

$$B_1 = \begin{bmatrix} 0.0 \\ 0.0 \\ 0.0 \\ 3.457440e+03 \\ 0.0 \\ 0.0 \end{bmatrix} \quad B_2 = \begin{bmatrix} 0.0 \\ 0.0 \\ 0.0 \\ 0.0 \\ 1.354691e+00 \\ 0.0 \end{bmatrix}$$

$$C = \begin{bmatrix} -9.010294e-01 & 0.0 & 0.0 & 0.0 & 1.503492e+00 & 0.0 \\ 7.557224e+01 & 0.0 & 0.0 & 0.0 & 0.0 & 1.995138e+01 \\ 0.0 & 0.0 & -3.457440e+02 & -9.643200e+00 & 0.0 & 0.0 \end{bmatrix}$$

$$D_1 = \begin{bmatrix} 0.0 \\ 0.0 \\ 3.457440e+02 \end{bmatrix} \quad D_2 = \begin{bmatrix} 9.010294e-01 \\ 0.0 \\ 0.0 \end{bmatrix}$$

The LMI controller gains are

$$K_{LMI} = [-2.283433e+01 \quad -2.242353e+01 \quad 1.840982e+02 \quad 8.538090e+00 \quad 5.152192e+01 \quad -5.398792e-01]$$

The  $H_\infty$  ARE feedback gains are

$$K_{ARE} = [-7.916660e-01 \quad -7.164470e-01 \quad 4.918770e+00 \quad 2.491234e-01 \quad 1.639036e+00 \quad -3.169201e-05]$$

Figure 2.7 illustrates a step response comparing the two designs. Both flight control designs produce similar responses.

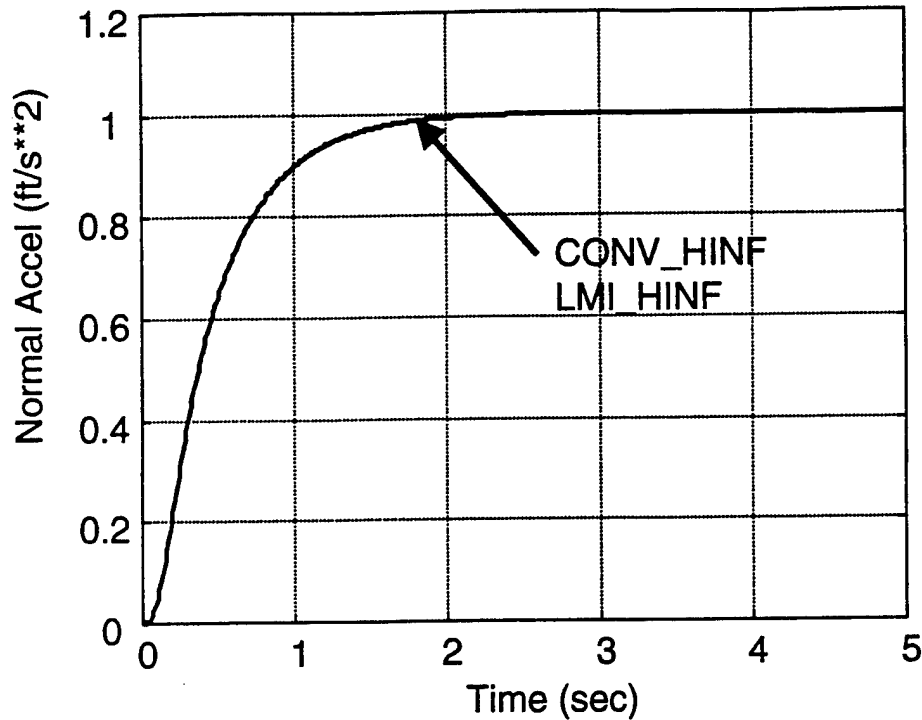


Figure 2.7  $H_{\infty}$  Controller Step Acceleration Command Simulation Response

#### 2.4 Chapter 2 References

1. E. Feron, V. Balakrishnan, S. Boyd, L. El Ghaoui, "Numerical Methods For  $H_2$  Related Problems," Proc. of the American Control Conference, Chicago, IL., June 1992.
2. Gahinet, P. and P. Apkarian, "A Linear Matrix Inequality Approach To  $H_{\infty}$  Control," Int. Journal of Robust and Nonlinear Control, Vol. 4, pp. 421-448, 1994.
3. S. Boyd, L. El Ghaoui, E. Feron, and V. Balakrishnan, *Linear Matrix Inequalities in System and Control Theory*, SIAM, Philadelphia PA, 1994.
4. Wise, K. A., and E. Hamby, " $H_{\infty}$  Missile Autopilot Design With and Without Imaginary Axis Zeros," Proc. of the ACC, Baltimore MD, June 1994, pp. 1670-1674.
5. A. Packard, G. Becker, D. Philbrick, and G. Balas, "Control of Parametrically-Dependent Linear Systems: Applications To  $H_{\infty}$  Gain Scheduling," Proc. Of the 1<sup>st</sup> IEEE Regional Conference on Aerospace Control Systems, Westlake Village CA, May 1993, pp. 329-333.

6. G. Becker, A. Packard, D. Philbrick, and G. Balas, "Control of Parametrically-Dependent Linear Systems: A Single Quadratic Lyapunov Approach," Proc. of the ACC, San Francisco CA, June 1993, pp. 2795-2799.
7. Wise, K. A. and J. Brinker "Linear Quadratic Flight Control For Ejection Seats," Journal of Guidance, Control, and Dynamics, Vol. 19, No. 1, 1996, pp. 15-22.

## **Chapter 3**

# **Stability Analysis Of Reconfigurable and Gain Scheduled Flight Control Systems Using LMIs**

### **3.1 Introduction**

Stability analysis methods currently used by industry for analyzing gain scheduled flight control systems do not address the time varying parameter dependence of the models used in the analysis. The proof of stability for these conventional control laws is provided by linear analyses (gain and phase margins) at discrete points in the flight envelope and by extensive numerical simulation in non-real-time and real-time simulators. However, proving stability by numerical simulation may not find all the flight conditions where the aircraft's stability and flying qualities fail to meet requirements. This approach can also be very expensive in manpower and schedule. The development of a proof-of-stability tool capable of analyzing gain scheduled control laws, as well as reconfigurable flight control laws, will significantly reduce development costs and will provide confidence that the control laws will work.

In addition to providing normal mode operation, fly-by-wire digital flight control systems are being designed to be reconfigurable and damage adaptive [1]. This capability, once matured, will greatly improve flight safety. However, it complicates the analysis of the flight control laws. In this paper the reconfigurable control laws are designed to be similar to gain scheduled control laws. This is not true for all reconfigurable control law designs, and the analysis methods developed here may or may not apply to all reconfigurable flight control systems. In our case the reconfigurable control laws are scheduled with parameters that, if known, would stabilize the aircraft and provide the pilot with control over its trajectory.

Conventional linear stability analysis (point designs with linear analysis) of reconfigurable or gain scheduled flight control laws always raises the a question of validity due to the transient/time varying nature of the problem. For gain scheduled flight control laws the gains are often scheduled with angle-of-attack, which may not be slowly varying in modern fighter aircraft. For reconfigurable controls, the control laws often change very quickly with the

identification of a failure or damage. If these systems can be adequately modeled using time-varying parameter dependent models, then linear matrix inequalities (LMIs) can be used to analyze stability.

There has been much recent progress made in using LMIs for control system analysis and design [2-7]. For the past few years the CDC and ACC conferences both have had special sessions and workshops in which LMIs have played a central role. Doyle [7] appropriately refers to these developments as a "postmodern control theory." Virtually all aspects of control are being developed: optimal realizations; controller synthesis; norm scaling; multiplier synthesis, and robustness analysis/synthesis for real parameter variations. Boyd [4] outlines many of the control synthesis problems which can be posed as LMI problems.

The following table lists four categories we have used to describe the scheduling parameters for parameter dependent models:

Category	Scheduling Parameters	
I	Known	Slow
II	Known	Not Slow
III	Inaccurate	Slow
IV	Inaccurate	Not Slow

Category I models contain systems whose parameters are known and do not vary with time. This is the analysis model that is assumed for conventional gain scheduled flight control systems used in industry. Issues for this category include: 1) Implementation of the gain schedule (rates) and the finite approximation of a continuum (interpolation strategy); 2) Accuracy of local stability analysis based upon point design and analysis.

Category II contains systems whose parameters are known and vary with time. Here the gain scheduling parameter space is gridded and at each grid point there is a polytope of parameter rates. If parameter dependent Lyapunov functions are used for analysis, the derivative of the Lyapunov matrix ( $\dot{P}$ ) must be included. This creates a partial differential inequality analysis problem, requiring approximation methods for solution.

Category III contains systems whose parameters are not precisely known or measurable and do not vary with time. For this problem one could set up a polytopic linear matrix inequality,

and prove stability by finding a Lyapunov function that, when using the control gains at a fixed grid point (the centroid), is valid within a convex region about the centroid grid point as well.

Category IV contains systems whose parameters are not precisely known or measurable and vary with time. This problem can be addressed by coupling the techniques used to address Category II and III systems.

In this research we are trying to exploit the recent developments using LMIs for parameter dependent systems to produce a method/tool that can be used to analyze the stability characteristics of reconfigurable flight control systems. Our approach requires modeling the closed loop system dynamics in such a way that LMIs can be applied. This approach is very similar to the ongoing research of Packard, Becker, Balas, Gahinet, Apkarian [2,3] and others who are developing algorithms for linear parameter varying gain scheduled control system design. To proceed we must develop a model of the aircraft that is parameterized with the amount of battle damage sustained. A coupled pitch-roll-yaw model is developed in Section 2 that is parameterized with wing damage. In Section 3, a gain scheduled control law for the pitch-plane is designed and scheduled with the damage parameter. In Section 4, our approach for analyzing stability using LMIs is presented. Two tutorial examples using linear time invariant systems are presented illustrating the stability guarantees from the LMI analysis. The approach is then applied to the tailless fighter model using a control that is gain scheduled with the amount of wing damage. To reduce the computational burden associated with the LMI problems to be solved, only the pitch-plane is analyzed. The final section discusses conclusions.

### **3.2 Tailless Fighter Model With Battle Damage**

High fidelity nonlinear simulations are often used to produce linear models of the aircraft's dynamics. Once in linear form, control laws are designed and analyzed, and are then "scheduled" with parameters that describe the operating point or flight condition. The idea here is to create a *set* of linear models for the aircraft's dynamics and control laws, based upon these scheduling parameters. The control laws will then be designed in a conventional way, based upon point-wise models, but the set (using a closed loop system) will be used for analysis.

Consider the linear differential inclusion (LDI) [4] given by

$$\dot{x} = \Omega x \quad x(0) = x_0 \quad (3.1)$$

where  $\Omega \subseteq R^{n \times n}$ . The LDI can be thought of as describing a family of linear time varying (LTV) systems. Specific LDIs of interest include linear time invariant (LTI) systems, where  $\Omega$  is a singleton. For LTI systems, the LDI reduces to

$$\begin{aligned} \dot{x} &= Ax + B_u u + B_w w \\ z &= Cx + D_{zu} u + D_{zw} w \end{aligned} \quad (3.2)$$

with

$$\Omega = \left\{ \begin{bmatrix} A & B_u & B_w \\ C & D_{zu} & D_{zw} \end{bmatrix} \right\}$$

When  $\Omega$  is a polytope, the LDI is a polytopic LDI (PLDI), with  $\Omega$  described by a list of its vertices in the form

$$\Omega = Co \left\{ \begin{bmatrix} A_1 & B_{u,1} & B_{w,1} \\ C_1 & D_{zu,1} & D_{zw,1} \end{bmatrix}, \dots, \begin{bmatrix} A_L & B_{u,L} & B_{w,L} \\ C_L & D_{zu,L} & D_{zw,L} \end{bmatrix} \right\}$$

This characterization of the LDI Eq. (3.1) is used in our approach. In Boyd [4] the idea of using LDIs to analyze nonlinear systems of the form

$$\begin{aligned} \dot{x} &= f(x, u, w, t) \\ z &= g(x, u, w, t) \end{aligned} \quad (3.3)$$

is discussed. If, for each  $(x, u, w, t)$  there is a  $G(x, u, w, t) \in \Omega$  such that

$$\begin{bmatrix} f(x, u, w, t) \\ g(x, u, w, t) \end{bmatrix} = G(x, u, w, t) \begin{bmatrix} x \\ u \\ w \end{bmatrix}, \quad (3.4)$$

then certain important properties about the nonlinear system can be inferred from analysis of the LDI (such as the trajectories converging to zero, etc.). Conditions for the existence of  $G$  are  $f(0,0,0,0) = 0$ ,  $g(0,0,0,0) = 0$ , and

$$\begin{bmatrix} \frac{\partial f}{\partial x} & \frac{\partial f}{\partial u} & \frac{\partial f}{\partial w} \\ \frac{\partial g}{\partial x} & \frac{\partial g}{\partial u} & \frac{\partial g}{\partial w} \end{bmatrix} \in \Omega \quad \forall x, u, w, t..$$

Aircraft and missile models (Eq. (3.3)) are typically modeled using forms similar to Eq.(3.4). Here we are proposing to model the aircraft dynamics using Eq. (3.4), under battle damage, and form a linear parameter dependent model of the dynamics.

The aircraft under study is the Boeing Tailless Advanced Fighter Aircraft (TAFA) model. Brinker [1] contains more descriptions of the baseline TAFA aircraft, control laws, control effectors, and damage models.

A high fidelity six degree-of-freedom (6DOF) simulation of the TAFA was constructed in MATRIXx. Using the "trim" and "linearization" features of MATRIXx, 1 g linear models were extracted from the 6DOF with varying levels of battle damage (wing missing). The linear parameter dependent model presented in this section is a model of the coupled pitch-roll-yaw dynamics at a low altitude high speed flight condition ( $h=0$  ft., Mach = 0.9) with battle damage (wing missing).

The battle (wing) damage was parameterized by the variable  $\rho_D \in [0, 1]$ , where 0 represents a healthy aircraft, and 1 represents a severe damage mode with the entire right wing missing. Intermediate values of  $\rho_D$ , say 0.1, represents the outer 10% of the wing missing. The linear parameter dependent state space model is given by:

$$\dot{x} = A(\rho_D)x + B(\rho_D)u.$$

Using increments of 0.1 for  $\rho_D$ , eleven models were extracted from the 6DOF for different levels of wing damage. The elements of the  $A$  and  $B$  matrices were then fit using polynomials in  $\rho_D$ . Linear, cubic, and quintic polynomials were used to model the matrix elements. For the quintic polynomial, the matrices are reconstructed as follows:

$$\hat{A} = A_0 + A_1\rho_D + A_2\rho_D^2 + A_3\rho_D^3 + A_4\rho_D^4 + A_5\rho_D^5$$
$$\hat{B} = B_0 + B_1\rho_D + B_2\rho_D^2 + B_3\rho_D^3 + B_4\rho_D^4 + B_5\rho_D^5$$

To determine which polynomial model to use, the polynomial approximations were compared with the matrices obtained from the 6DOF. Error matrices were formed for each polynomial model using  $E = A - \hat{A}$ , and the norm of the error matrix was calculated. The  $\|E\|_1$ ,  $\|E\|_2$ ,  $\|E\|_\infty$ , and  $\|E\|_F$  norms were all used to measure the accuracy. Figures 3.1 and 3.2 show numerical results comparing linear, cubic, and quintic polynomials as a function of wing damage parameter  $\rho_D$ .

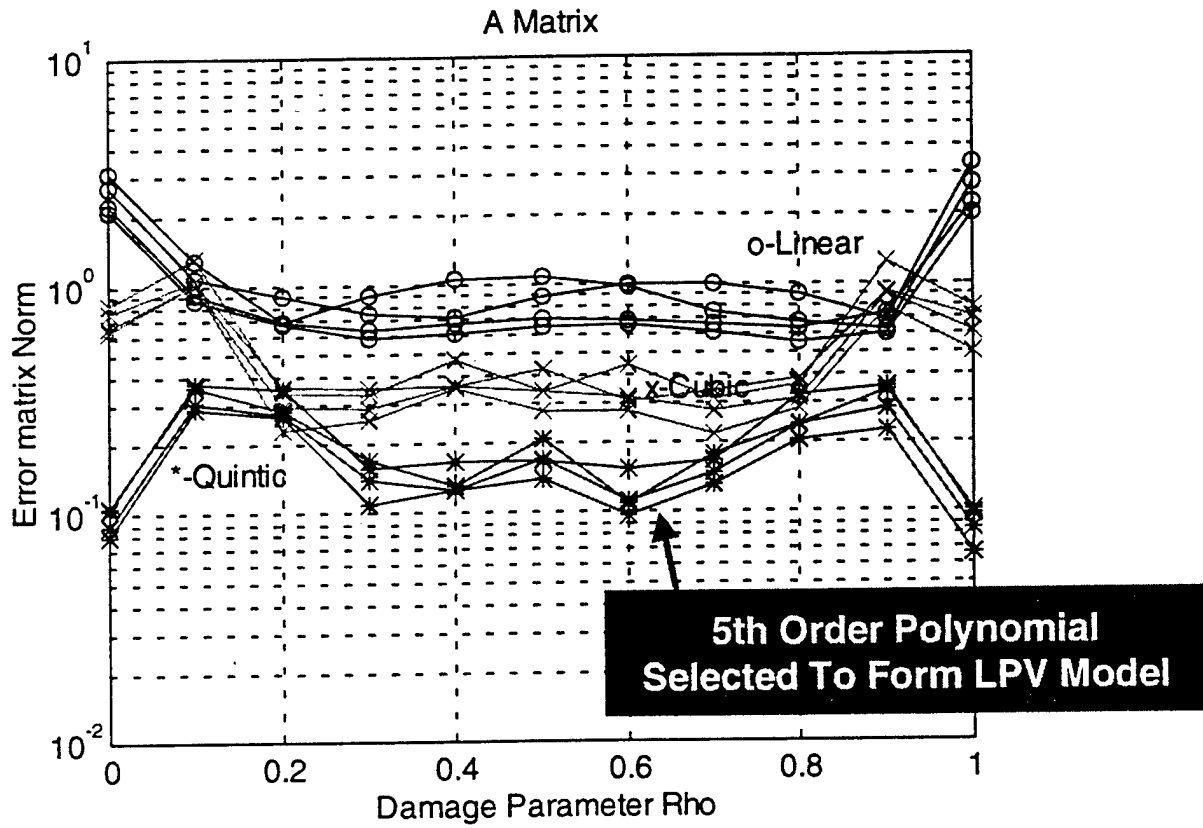


Figure 3.1 Polynomial Approximation Of The A Matrix

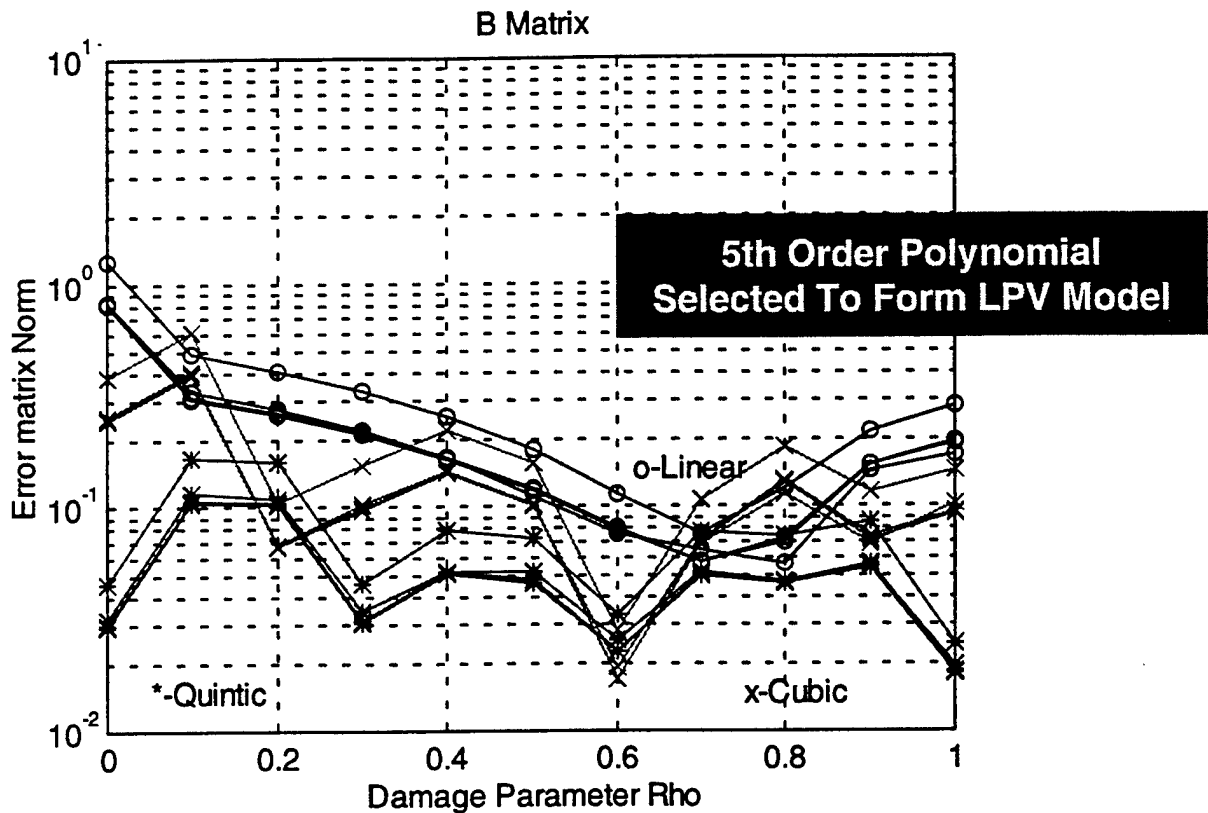


Figure 3.2 Polynomial Approximation Of The B Matrix

Figure 3.1 shows that the linear and cubic polynomials in  $\rho_D$  do not adequately model the  $A$  matrix (at  $\rho_D$  close to zero and at unity). The quintic polynomial maintains the norm of the error less than 0.5, and was selected to model the dynamics. Figure 3.2 shows that the wing damage parameter  $\rho_D$  enters linearly into the  $B$  matrix. As a result, the linear polynomial adequately models the wing damage control powers. Numerical values for the quintic polynomial coefficients can be obtained electronically by contacting the first author at [kevin.a.wise@boeing.com](mailto:kevin.a.wise@boeing.com).

### **3.3 Gain Scheduled Flight Control Design**

A pitch rate command flight control design was developed to accommodate the varying levels of wing damage based on the Robust Servo Linear Quadratic Regulator (RSLQR) formulation [8]. The RSLQR is based on a linear time invariant (LTI) optimal control solution that produces a constant gain state feedback controller which is then gain scheduled with the amount of wing damage  $\rho_D$ . To produce an output feedback implementation, projective control theory [9] is used to project the dominant eigenstructure of the state feedback RSLQR design into an output feedback design.

Figure 3.3 illustrates the pitch rate command controller architecture. This controller architecture uses pitch rate and normal acceleration feedback. Integral control is employed on the pitch rate command error to provide zero steady state error to a step command. An aircraft with multiple longitudinal plane control effectors can be accommodated via a predefined control mixing, in which the mixing can also vary with flight condition. This approach ensures that the control effector blending is smooth across the flight envelope, and thus prevents excessive surface motion due to gain schedule variations.

The stick shaping logic required for implementation is not designed in the RSLQR process. Instead the stick shaping is set in the 6DOF controller implementation to achieve a desired pitch response sensitivity. In the 6DOF implementation the stick actually commands normal acceleration which is then converted to an equivalent pitch rate command prior to entering the LQR command structure.

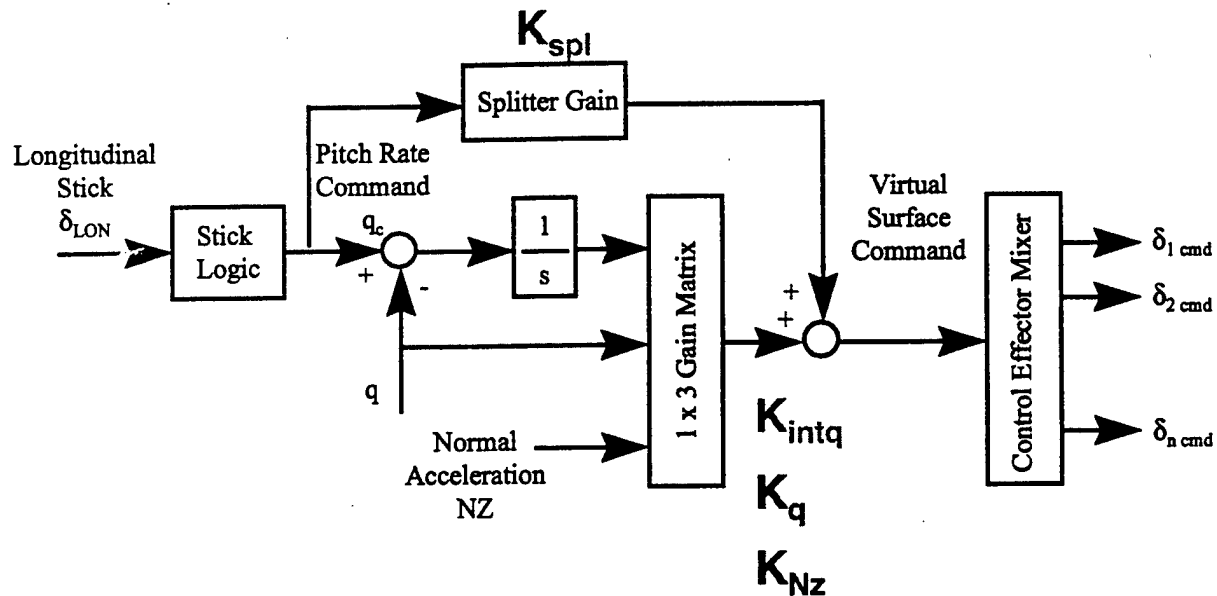


Figure 3.3 Longitudinal controller structure.

The feedback gains for this output feedback controller were designed using an automated tool that adjusts the LQR penalty matrices. The gain matrix  $\bar{K}$  for the output feedback contains 3 gains. Its location in the inner loop control architecture is shown in Figure 3.3. Figure 3.3 also shows a splitter gain used to feed-forward the command directly to the virtual actuator. This gain has proven to be very important in shaping the zero dynamics to get good flying qualities.

Figure 3.4 shows the resulting feedback gains and splitter gain plotted against the wing damage parameter  $\rho_D$ . The negative of the gains were plotted using a logarithmic scale to highlight the magnitude changes. Several of the gains have significant magnitude changes between design points.

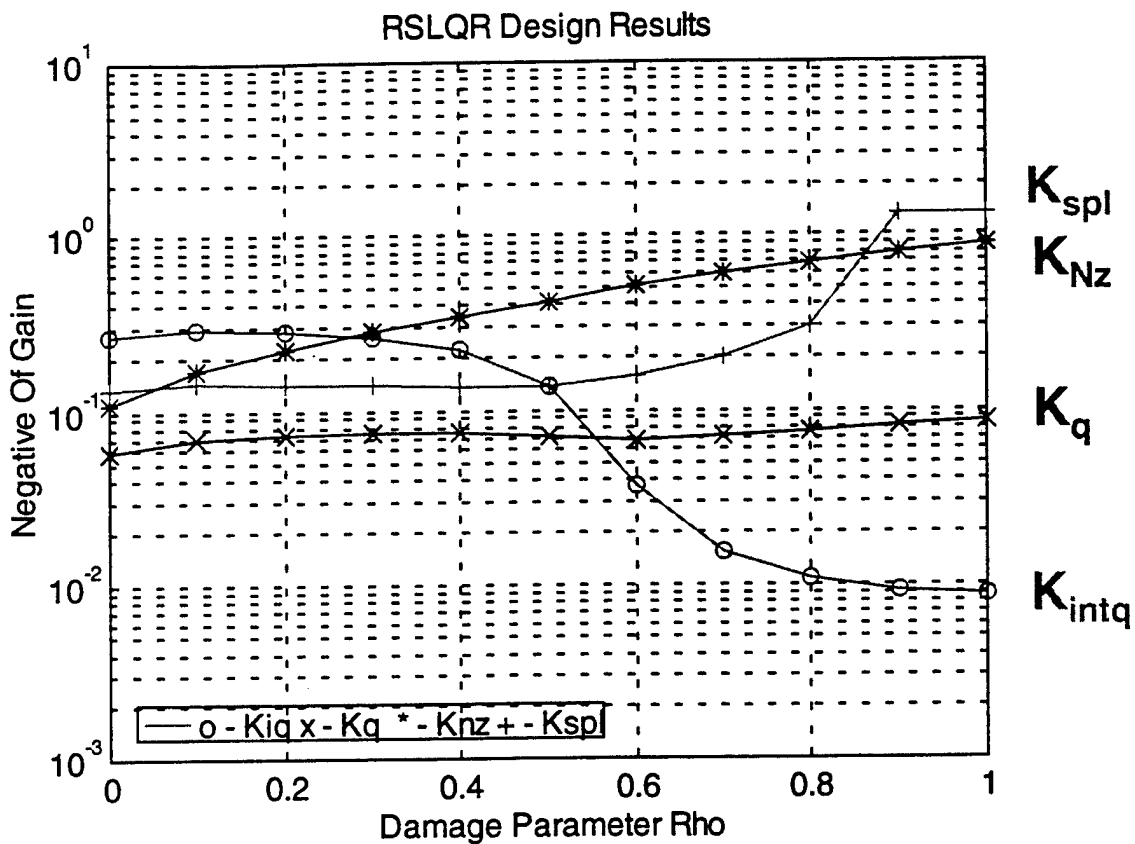


Figure 3.4 Pitch Controller Output Feedback Gains

Analysis results for each of these point designs is shown in Figure 3.5 along with the target values for the flying qualities. To evaluate the flying qualities a low order equivalent system (LOES) was fit to the closed loop frequency response. The LOES model is

$$\frac{q}{\delta_{Stick}} = \frac{K(s + L_{\alpha})e^{T_s s}}{s^2 + 2\zeta_{sp}\omega_{sp}s + \omega_{sp}^2}$$

A maximum likelihood tuning algorithm was used to adjust the model parameters. The tuning algorithm used the error in matching the target parameters ( $\omega_{sp}$ ,  $\zeta_{sp}$ ,  $L_{\alpha}$ ), a minimum stability margin requirement (6 dB and 45 deg. phase), and number of iterations (10) as stopping criteria.

The analysis results show that the LQR tuning algorithm was able to obtain identical flying qualities as the healthy aircraft for values of  $\rho_D < 0.5$ , but did not converge (using a strict set of criteria) for larger values of  $\rho_D$ . At the larger values of  $\rho_D$  the phase margin requirement terminated the design process. Further trade studies could be performed relaxing requirements to further improve the match with the target flying qualities.

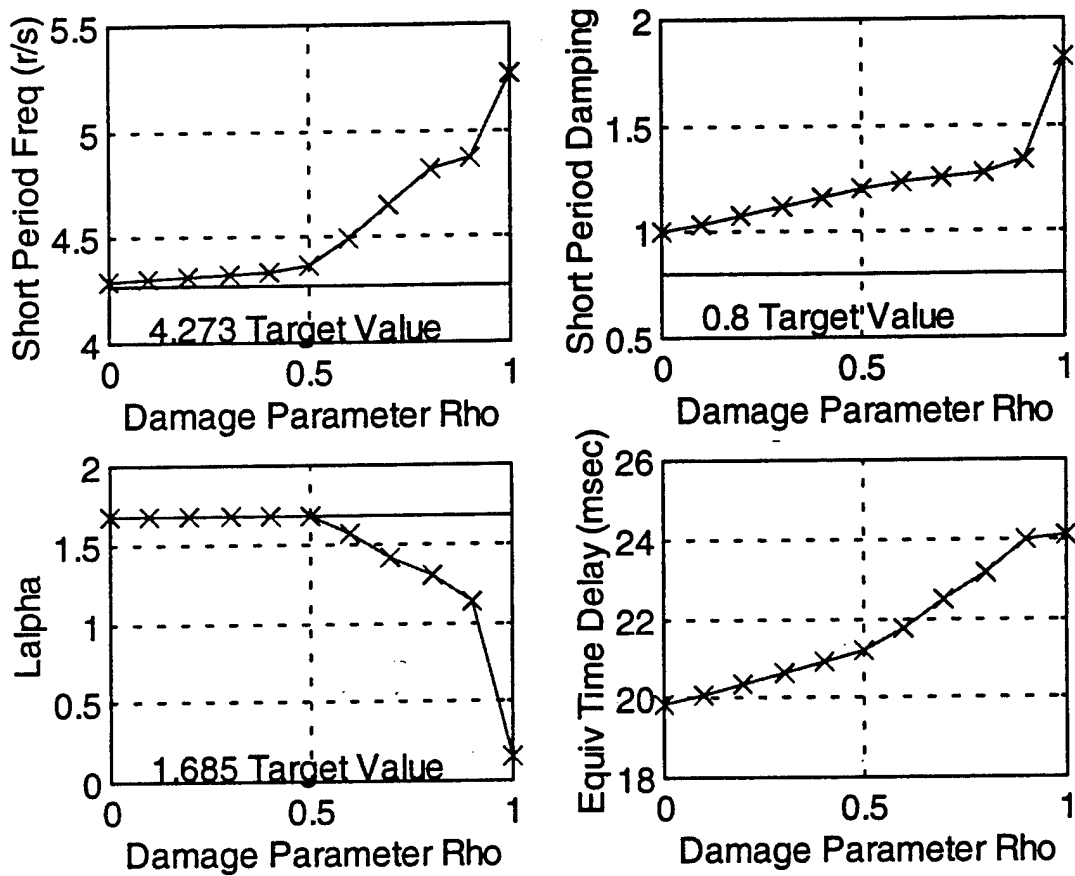


Figure 3.5 Point Design Flying Qualities Analysis

### 3.4 Stability Analysis Using LMIs

The key to using LMIs for proving stability is to model the system as a linear parameter varying (LPV) system and to use a standard Lyapunov argument for proving exponential stability. First, consider the linear system given by

$$\dot{x}(t) = A(t)x(t). \quad (3.5)$$

Trajectories for Eq. (3.5) can be expressed using its state transition matrix as

$$x(t) = \Phi(t, \tau)x(\tau). \quad (3.6)$$

For quadratic stability considerations, the Lyapunov function is given as

$$V(t) = x^T(t)P(t)x(t) \quad (3.7)$$

where  $P(t) > 0 \quad \forall t > 0$ . Substituting Eq. (3.6) into (3.7) yields

$$V(t) = x^T(\tau)\Phi^T(t, \tau)P(t)\Phi(t, \tau)x(\tau)$$

Differentiating yields

$$\begin{aligned} \dot{V}(t) &= x^T(\tau)\Phi^T(t, \tau)[A^T(t)P(t) + P(t)A(t) + \dot{P}(t)]\Phi(t, \tau)x(\tau) \\ &= x^T(t)[\dot{P}(t) + A^T(t)P(t) + P(t)A(t)]x(t) \end{aligned} \quad (3.8)$$

If there exists positive constants  $\epsilon_1$ ,  $\epsilon_2$ , and  $\epsilon_3$  such that  $\epsilon_1 I \leq P(t) \leq \epsilon_2 I$  and

$$\dot{P}(t) + A^T(t)P(t) + P(t)A(t) \leq -\epsilon_3 I, \quad (3.9)$$

then, substituting Eq. (3.9) into Eq. (3.8) yields

$$\dot{V}(t) \leq -\frac{\epsilon_3}{\epsilon_2} \epsilon_2 x^T(t)x(t) = -\frac{\epsilon_3}{\epsilon_2} \epsilon_2 x^T(t)x(t). \quad (3.10)$$

Since  $\epsilon_1 I \leq P(t) \leq \epsilon_2 I$ ,

$$\epsilon_1 x^T(t)x(t) \leq V(t) \leq \epsilon_2 x^T(t)x(t). \quad (3.11)$$

Substituting  $V(t) \leq \epsilon_2 x^T(t)x(t)$  into Eq. (3.10) results in

$$\dot{V}(t) \leq -\frac{\epsilon_3}{\epsilon_2} V(t).$$

Integrating this expression yields

$$\begin{aligned} \ln V(t) - \ln V(\tau) &\leq -\frac{\epsilon_3}{\epsilon_2} (t - \tau) \\ \ln \left( \frac{V(t)}{V(\tau)} \right) &\leq -\frac{\epsilon_3}{\epsilon_2} (t - \tau) \\ \frac{V(t)}{V(\tau)} &\leq \exp \left( -\frac{\epsilon_3}{\epsilon_2} (t - \tau) \right) \\ V(t) &\leq V(\tau) \exp \left( -\frac{\epsilon_3}{\epsilon_2} (t - \tau) \right). \end{aligned} \quad (3.12)$$

From Eq. (3.11),  $V(\tau) \leq \epsilon_2 x^T(\tau)x(\tau)$  and  $V(t) \geq \epsilon_1 x^T(t)x(t)$ . Substituting these expressions into Eq. (3.12) results in

$$\epsilon_1 x^T(t)x(t) \leq \epsilon_2 x^T(\tau)x(\tau) \exp \left( -\frac{\epsilon_3}{\epsilon_2} (t - \tau) \right).$$

Dividing by  $x^T(\tau)x(\tau)$  and using Eq. (3.6) we have

$$\frac{x^T(t)x(t)}{x^T(\tau)x(\tau)} = \frac{x^T(\tau)\Phi^T(t,\tau)\Phi(t,\tau)x(\tau)}{x^T(\tau)x(\tau)} \leq \frac{\epsilon_2}{\epsilon_1} \exp\left(-\frac{\epsilon_3}{\epsilon_2}(t-\tau)\right)$$

Which implies that

$$\|\Phi(t,\tau)\|^2 \leq \frac{\epsilon_2}{\epsilon_1} \exp\left(-\frac{\epsilon_3}{\epsilon_2}(t-\tau)\right)$$

$$\|\Phi(t,\tau)\| \leq \sqrt{\frac{\epsilon_2}{\epsilon_1}} \exp\left(-\frac{\epsilon_3}{2\epsilon_2}(t-\tau)\right)$$

which shows that the trajectories of Eq. (3.5) are bounded exponentially.

Like the previous linear system in Eq. (3.5), stability for reconfigurable or gain scheduled control laws modeled using a LPV model described by

$$\dot{x} = A(\rho)x(t) \tag{3.13}$$

can be guaranteed by establishing that a Lyapunov inequality can be satisfied everywhere within a region  $\rho \in \mathcal{P}$  of parameter values, that is to say that there exists a  $P \geq 0$  such that

$$\dot{P} + A^T(\rho)P + PA(\rho) \leq 0 \quad \forall \rho \in \mathcal{P}$$

This analysis however does not give any measure of the degree of stability nor the amount of stability sacrificed by requiring stability over a wide range of parameter values.

To this end we utilize the standard Lyapunov argument which says that if there exists an  $\epsilon_1 > 0, \epsilon_2 > 0, \epsilon_3 > 0$  and a  $\mathcal{W}$  such that

$$\varepsilon_1 I \leq W \leq \varepsilon_2 I, \quad (3.14)$$

and

$$\dot{W} + A^T W + W A \leq -\varepsilon_3 I$$

then the state transition matrix  $\Phi(t, \tau)$  satisfies

$$\|\Phi(t, \tau)\| \leq \sqrt{\frac{\varepsilon_2}{\varepsilon_1}} e^{-\frac{\varepsilon_3}{2\varepsilon_2}(t-\tau)}$$

Letting  $\gamma = \frac{\varepsilon_3}{\varepsilon_2}$  and  $P = \frac{W}{\varepsilon_2}$  this leads to the following inequalities

$$P > 0, \quad P \geq I, \quad \dot{P} + A^T P + P A \leq -\gamma I$$

and with  $\gamma > 0$ , this implies

$$\|\Phi(t, \tau)\| \leq \frac{1}{\sqrt{\underline{\lambda}(P)}} e^{-\frac{\gamma}{2}(t-\tau)}$$

where  $\underline{\lambda}(P)$  denotes the minimum eigenvalue of  $P$ . This leads to the following LMI problem (letting  $\mu = -\gamma$ ) which is the focus of this paper.

#### LMI Problem

$$\begin{aligned} & \min \quad \mu \\ & \mu, P(\rho) \end{aligned} \quad (3.15)$$

subject to

$$P(\rho) > 0 \quad (i)$$

$$I - P(\rho) \geq 0 \quad (ii)$$

$$\mu I - \dot{P}(\rho) - A^T(\rho)P(\rho) - P(\rho)A(\rho) \geq 0 \quad (iii)$$

for all  $\rho \in \mathbf{P}$ . Then if  $\mu < 0$ , the system is stable and

$$\|\Phi(t, \tau)\| \leq \frac{1}{\sqrt{\lambda(P)}} e^{\frac{\mu}{2}(t-\tau)} \quad (3.16)$$

The parameter  $\mu$  can be used as a measure of the degree of stability. The inequality (ii) has been introduced to scale the problem, otherwise the optimization problem would be homogenous in  $\mu$  and  $P(\rho)$ . The following examples illustrate its use.

### Example 1

Consider the linear system described by  $\dot{x} = Ax$  with

$$A = \begin{bmatrix} -5 & 1 \\ 1 & -5 \end{bmatrix}$$

Since this is a LTI system the LMI problem described in Eq. (3.15) does not contain a  $\dot{P}$  term. Also, since it is LTI it is very easy to determine stability ( $\lambda_i(A) = -4, -6$ ). However, this simple example will clearly indicate how  $\mu$  in Eq. (3.16) can be used as a measure of stability, and the bound on the state transition matrix can be determined analytically and computationally (as a LMI optimization problem). The constraints in Eq. (3.15) restrict the  $P$  matrix as follows: Let

$$P = \begin{bmatrix} p_1 & p_2 \\ p_2 & p_3 \end{bmatrix} \quad (3.17)$$

From constraint (i) we have:  $p_1 > 0$ ,  $p_3 > 0$ , and  $p_1 p_3 - p_2^2 > 0$ . From constraint (ii) we have:  $1 - p_1 \geq 0$ ,  $1 - p_3 \geq 0$ , and  $(1 - p_1)(1 - p_3) - p_2^2 \geq 0$ . Let

$$\begin{bmatrix} m_1 & m_2 \\ m_2 & m_3 \end{bmatrix} = A^T P + P A = \begin{bmatrix} -10p_1 + 2p_2 & p_1 - 10p_2 + p_3 \\ \times & 2p_2 - 10p_3 \end{bmatrix}$$

From the constraint (iii) we have:  $\mu - m_1 \geq 0$ ,  $\mu - m_3 \geq 0$ , and  $(\mu - m_1)(\mu - m_3) - m_2^2 \geq 0$ . To minimize  $\mu$  by selecting  $p_1$ ,  $p_2$ , and  $p_3$ , we can infer from the symmetry that  $p_1 = p_3$ . Then,

$$(1 - p_1)(1 - p_3) - p_2^2 = (1 - p_1)^2 - p_2^2 \geq 0$$

For the problem of minimizing  $\mu$ , the above inequality is an equality, reducing to  $p_2^2 = (1 - p_1)^2$ .

Using  $p_1 > 0$  and  $1 - p_1 > 0$  we have  $p_2 = 1 - p_1$ . Thus minimizing  $\mu$  also leads to

$$(\mu - m_1)(\mu - m_3) - m_2^2 = 0. \text{ Substituting yields}$$

$$\mu^2 - (4 - 24p_1)\mu + (-96 + 192p_1) = 0$$

which has a minimum at  $\mu = -8$  no matter what  $p_1$  is. Using  $0 < p_1 \leq 1$ ,  $p_2 = 1 - p_1$ , and  $p_3 = p_1$ , the eigenvalues of  $P$  are at  $\lambda_1 = 2p_1 - 1$  and  $\lambda_2 = 1$ . The minimum eigenvalue of  $P$  gives the tightest bound ( $p_1 = 1$ ),  $P = I$ , which gives

$$\frac{1}{\sqrt{\lambda_2(P)}} e^{\frac{\mu}{2}(t-\tau)} = e^{-4t} \tag{3.18}$$

(note that  $-4$  is the right most  $\lambda_i(A)$ ). Figure 3.6 (a) plots the actual norm of the state transition matrix (solid) against the LMI bound in Eq. (3.18). For this example they are identical.

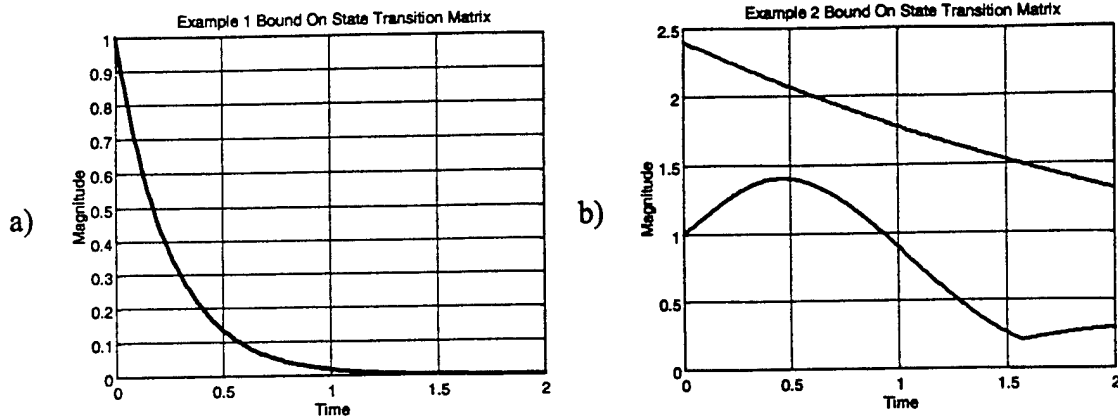


Figure 3.6 LMI bounds on the state transition matrix.

**Example 2**

Consider the linear system described by  $\dot{x} = Ax$  with

$$A = \begin{bmatrix} 0 & 1 \\ -5 & -2 \end{bmatrix}$$

which has eigenvalues at  $\lambda_i = -1 \pm 2j$ . Using the same procedure as in Example 1, the  $P$  matrix in Eq. (3.17) is calculated as

$$P = p_2 \begin{bmatrix} 17 & 1 \\ 1 & 3 \end{bmatrix}.$$

To minimize  $\mu$  in the LMI (Eq. (3.14)),  $p_2 = (2 - \sqrt{2})/10$ . This yields a  $\mu = -0.5858$ , and  $\lambda_i(P) = 1, 3 - 2\sqrt{2}$ . The  $\lambda_-(P) = 0.17157$ , which gives

$$\frac{1}{\sqrt{\underline{\lambda}(P)}} e^{\frac{\mu}{2}(t-\tau)} = 2.4e^{-0.3t} \quad (3.19)$$

Figure 3.6 (b) plots the norm of the state transition matrix (solid) against the LMI bound in Eq. (3.19). Note for this example the bound is somewhat conservative.

### 3.5 Tailless Fighter Analysis Results

The LMI problem described in Eq. (3.15) was used to analyze the tailless fighter reconfigurable / gain scheduled flight control system. The scheduling parameter used was the wing damage parameter  $\rho_D$ . Results are presented using the category definitions described in the Introduction.

The LMI convex optimization produces the optimal  $\mu$  and  $P$  matrix for Eq. (3.15) at the polytope vertices used in defining the analysis problem. The proof of stability uses the  $\mu$  and the minimum eigenvalue of  $P$ ,  $\underline{\lambda}(P)$ , to bound the state transition. Since the scheduling problem is infinite dimensional and gridding of the parameter space is used to make the problem finite dimensional, one must still check how well the constraints in Eq. (3.15) are satisfied between the grid points.

#### Stability Analysis For Category I Systems

Category I systems are linear systems whose scheduling parameters are known and do not vary with time. A conventional linear analysis on each discrete flight condition is valid and is typically used to analyze stability.

The LMI analysis method in Eq. (3.15) was applied to the pitch-plane tailless fighter system described in Section 3 at each discrete value of  $\rho_D$ , assuming that  $\dot{\rho}_D = 0$ . Here each discrete flight condition is analyzed separately. Solving the 11 LMI problems produces the following results:

$\rho_D$	$\max(\text{Re}(\lambda(A(\rho_D)))$	$\mu$ From Eq. (4.21)	$\underline{\lambda}(P)$
0.0	-2.4972	-0.04161	$2.2573 \times 10^{-4}$
0.1	-2.4048	-0.03984	$2.1643 \times 10^{-4}$
0.2	-2.2151	-0.03845	$2.0933 \times 10^{-4}$
0.3	-1.9608	-0.03708	$2.0222 \times 10^{-4}$
0.4	-1.6196	-0.03577	$1.0528 \times 10^{-4}$
0.5	-0.9905	-0.03466	$1.8897 \times 10^{-4}$
0.6	-0.2471	-0.03258	$1.7671 \times 10^{-4}$
0.7	-0.0918	-0.02940	$1.5978 \times 10^{-4}$
0.8	-0.0584	-0.02616	$1.4250 \times 10^{-4}$
0.9	-0.0447	-0.02294	$1.2523 \times 10^{-4}$
1.0	-0.0393	-0.01991	$1.0893 \times 10^{-4}$

The first column is the wing damage parameter. The second column is the maximum real part of the eigenvalues for the closed loop system matrix using the gain scheduled control. The third and fourth columns form the exponential bound described in Eq. (3.16). The LMI analysis shows that the system is stable, but conservatively bounds the state transition matrix. Here LMI analysis is not really necessary since the examination of the eigenvalues of the closed loop system matrix suffices to prove stability.

### Stability Analysis For Category II Systems

Category II systems are linear systems whose scheduling parameters are known and vary with time. A conventional linear analysis at each discrete flight design point ignores the fact that the scheduling parameters can vary with time. Here, polytope vertices are introduced to accommodate the time varying scheduling parameter.

Rates of change of parameters will produce a  $\dot{P}$  term in the Lyapunov inequality in the LMI (Eq. (3.15)) which can be described by

$$\dot{P} = \sum_{\rho \in P} \frac{\partial P}{\partial \rho} \dot{\rho}$$

If we assume that the rates of the parameter variations  $\dot{\rho}$  are known, the problem becomes determining the partial derivatives  $\partial P / \partial \rho$ . The presence of these terms creates a linear partial differential inequality. In the LMI problem we must find a  $\mu$  valid for the entire range of parameter values  $0 \leq \rho \leq 1$ . To solve this problem we use basis functions (similar to [5,6]) in which we model  $P(\rho)$  using polynomials. The polynomial model is

$$P(\rho) = \sum_{i=0}^{D_p} P_i \rho^i$$

where  $D_p$  is the order of the polynomial. Then,

$$\frac{\partial P}{\partial \rho} = \sum_{i=0}^{D_p} i P_i \rho^{i-1}$$

Polytope vertices are then formed at the min and max rates for  $\rho_D$ . Since we can not add the wing back on, the min rate is modeled as  $\dot{\rho}_D = 0$ . The maximum rate was varied to determine the impact on the LMI analysis.

Figure 3.7 shows the LMI stability analysis results for the Category II system model. The four curves represent results using different max rates ( $\dot{\rho}_{\max} = 0.02, 10$ ) and different order polynomials for  $P(\rho)$ , ( $D_p = 5, 3$ ). The optimal  $\mu$  determined from the convex optimization was  $\mu = -0.01991$ , and was the same for all four cases. The plots in Figure 3.7 show how well the optimal  $P$  satisfies the LMI constraints at points in between the  $0.1 \rho_D$  grid spacing. The first plot shows the ( $P > 0$ ) constraint was satisfied. The second plot shows that the ( $I - P \geq 0$ ) constraint is violated in between  $\rho_D = 0.9$  and  $1.0$ . The third constraint in the LMI,

$\mu I - \dot{P}(\rho) - A^T(\rho)P(\rho) - P(\rho)A(\rho) \geq 0$ , was examined at the vertices where  $\dot{\rho} = 0$  and where  $\dot{\rho} = \dot{\rho}_{\max}$ . The curves show  $\underline{\lambda}(\Lambda)$  where  $\Lambda = -\dot{P}(\rho) - A^T(\rho)P(\rho) - P(\rho)A(\rho)$ , which we would like to be positive, and show that this is also violated in between  $\rho_D = 0.9$  and  $1.0$ .

However, as long as the optimal  $\mu$  is big enough to make

$\mu I - \dot{P}(\rho) - A^T(\rho)P(\rho) - P(\rho)A(\rho) \geq 0$  we have a good solution to the LMI problem. The difference between  $\mu$  and  $\underline{\lambda}(\Lambda)$  can be thought of as a "stability margin" in the analysis. Close examination of the most negative point in Figure 3.7 (lower right plot) shows that the optimal  $\mu$

$= -0.01991$  is not big enough to cover  $\underline{\lambda}(\Lambda) = -0.02273$ . This result indicates that the  $P$  matrix does not prove stability at this value of  $\rho_D$ . (Later we will show how to correct this problem.)

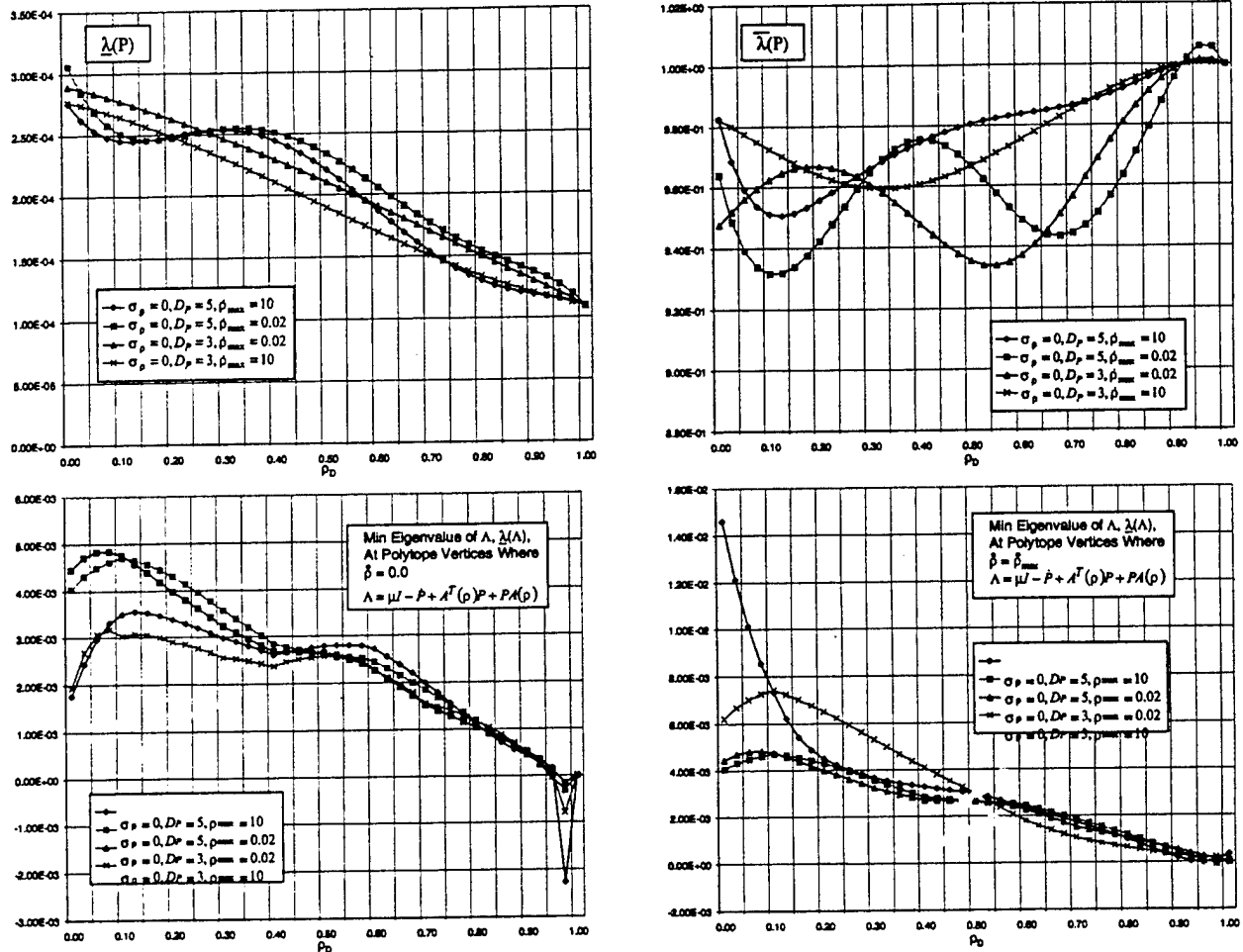
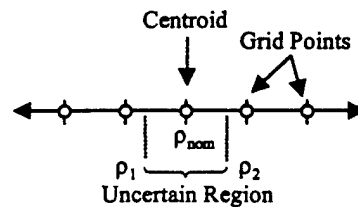


Figure 3.7 Category II stability analysis results.

### Stability Analysis For Category III Systems

Category III systems are linear systems whose scheduling parameters are not precisely known and are slowly varying with time. Since the scheduling parameters are not accurately known, the feedback gains that are scheduled with these parameters may not match the dynamics as intended. In this case we would like the gains to provide stability and performance in a convex region about the nominal or centroid grid point.

This convex region must be formed based upon estimates of the accuracy in estimating the scheduling parameters. For example, consider the following scheduling parameter centered at  $\rho_{nom}$



Feedback gains have been designed at each grid point. Estimates on the accuracy of the scheduling parameter define the uncertain region, which in this example we have assumed is smaller than the grid size. To analyze stability using the gains designed at  $\rho_{nom}$ , a convex polytope covering the uncertainty region is formed and analyzed.

Consider the parameter dependent system described by Eq. (3.13). The LMI problem for this system is infinite dimensional because of the continuous parameters used for scheduling. The problem can be made finite dimensional by densely gridding the  $\rho$  parameter space.

To include uncertainties in the parameter  $\rho$ , consider a nominal value with  $\pm 3\sigma_\rho$  variations, described by

$$\rho_1 = \rho - 3\sigma_\rho \leq \rho \leq \rho + 3\sigma_\rho = \rho_2$$

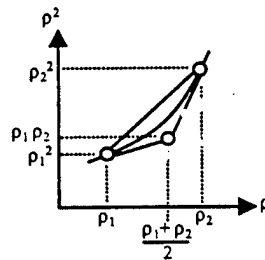
Then,

$$\rho = \theta \rho_1 + (1-\theta) \rho_2, \quad 0 \leq \theta \leq 1. \quad (3.20)$$

Consider the case where the system matrix  $A(\rho)$  can be represented as  $A(\rho) = A_0 + A_1 \rho + A_2 \rho^2$ . Using Eq. (3.20),  $\rho^2 = \theta^2 \rho_1^2 + 2\theta(1-\theta) \rho_1 \rho_2 + (1-\theta)^2 \rho_2^2$ . But we can write  $\rho = \theta^2 \rho_1 + 2\theta(1-\theta) \rho_1 \rho_2 / 2 + (1-\theta)^2 \rho_2$ . This allows us to describe  $A(\rho)$  as

$$A(\rho) = \theta^2 [A_0 + A_1 \rho_1 + A_2 \rho_1^2] + 2\theta(1-\theta) [A_0 + A_1 \frac{\rho_1 + \rho_2}{2} + A_2 \rho_1 \rho_2] + (1-\theta)^2 [A_0 + A_1 \rho_2 + A_2 \rho_2^2] \quad (3.21)$$

where the weights  $\theta^2$ ,  $2\theta(1-\theta)$ , and  $(1-\theta)^2$  are non-negative and sum to unity. This represents  $A(\rho)$  in barycentric coordinates at the point  $\rho$  between  $\rho_1$  and  $\rho_2$ . Also,  $A(\rho)$  is in the convex hull formed by the vertices of the triangle represented by the bracketed expressions in Eq. (3.21). This can be shown graphically as follows:



This can be generalized to any degree of polynomial. For system data  $A(\rho)$  represented by a polynomial of degree  $D_A$ , i.e.  $A(\rho) = \sum_{i=0}^{D_A} A_i \rho^i$ , there will be a convex polytope that has  $D_A + 1$  vertices that will enclose the system data in the interval  $[\rho_1, \rho_2]$ . Let the  $j$ th vertex be denoted as  $v_j$ . Then

$$v_j = \sum_{i=0}^{D_A} A_i r_{ij}$$

where for  $j < D_A - i$

$$r_{ij}(\rho_1, \rho_2) = \frac{1}{\binom{D_A}{j}} \sum_{k=0}^i \binom{k+D_A-i}{j} \binom{i}{k} (\rho_1 - \rho_2)^{i-k} \rho_2^k$$

and for  $j \geq D_A - i$

$$r_{ij}(\rho_1, \rho_2) = \frac{1}{\binom{D_A}{i}} \sum_{k=0}^{D_A-j} \binom{k+j}{D_A-i} \binom{D_A-j}{k} (\rho_1 - \rho_2)^{D_A-j-k} \rho_2^{k+i+j-D_A}$$

where the brackets denote binomial coefficients. It is straight forward that this procedure can be extended to any number of scheduling parameters.

Figure 3.8 shows the LMI stability analysis results for category III systems. Here, the polytope vertices are enclosed using the above method with  $3\sigma_p = 0.1$ . The first curve listed in the legend shows results from category II ( $\sigma_p = 0, D_p = 3, \dot{\rho}_{\max} = 0.02$ ) for comparison. The next three curves use ( $\dot{\rho}_{\max} = 0.02$ ) and different order polynomials for  $P(\rho)$ , ( $D_p = 5, 3$ ). The fourth curve listed incorporates additional constraints to prevent  $\underline{\lambda}(\Lambda)$  from becoming too negative. By adding additional LMI constraints in between 0.9 and 1.0, the resulting optimal  $P$  matrix better satisfies the constraints. The cost is a larger computational LMI problem. The optimal  $\mu$  for the Category III model was  $\mu = -0.01632$ . We see from the figure that by adding the additional constraints in between  $\rho_D = 0.9$  and 1.0 the LMI analysis proves stability.

### **Stability Analysis For Category IV Systems**

Category IV systems are linear systems whose scheduling parameters are not precisely known and vary with time. Our solution approach for Category IV models combines the approaches used for Category II and III systems, forming polytope vertices based upon the uncertainty in  $\rho$  and  $\dot{\rho}$ . Figure 3.9 shows the LMI stability analysis results. Here, the polytope vertices were formed using  $3\sigma_{\rho} = 0.1$  with  $(\dot{\rho}_{\max} = 5)$ , and different order polynomials for  $P(\rho)$ ,  $(D_p = 1, 3)$ . The third curve listed in the legend added additional constraints to keep the constraints satisfied in between  $\rho_D = 0.9$  and 1.0. In calculating the fourth curve, grid points at small values of  $\rho_D$  were dropped and new grid points in between  $\rho_D = 0.9$  and 1.0 were added, where the total number of grid points was kept equal to the original problem (thus keeping the size of the LMI problem constant). The optimal  $\mu$  for each curve listed in Figure 3.9 was  $\mu = -0.01627, -0.01586, -0.01574,$  and  $-0.01632$ , respectively. The results prove stability for the gain scheduled control in the presence of time varying uncertain parameters.

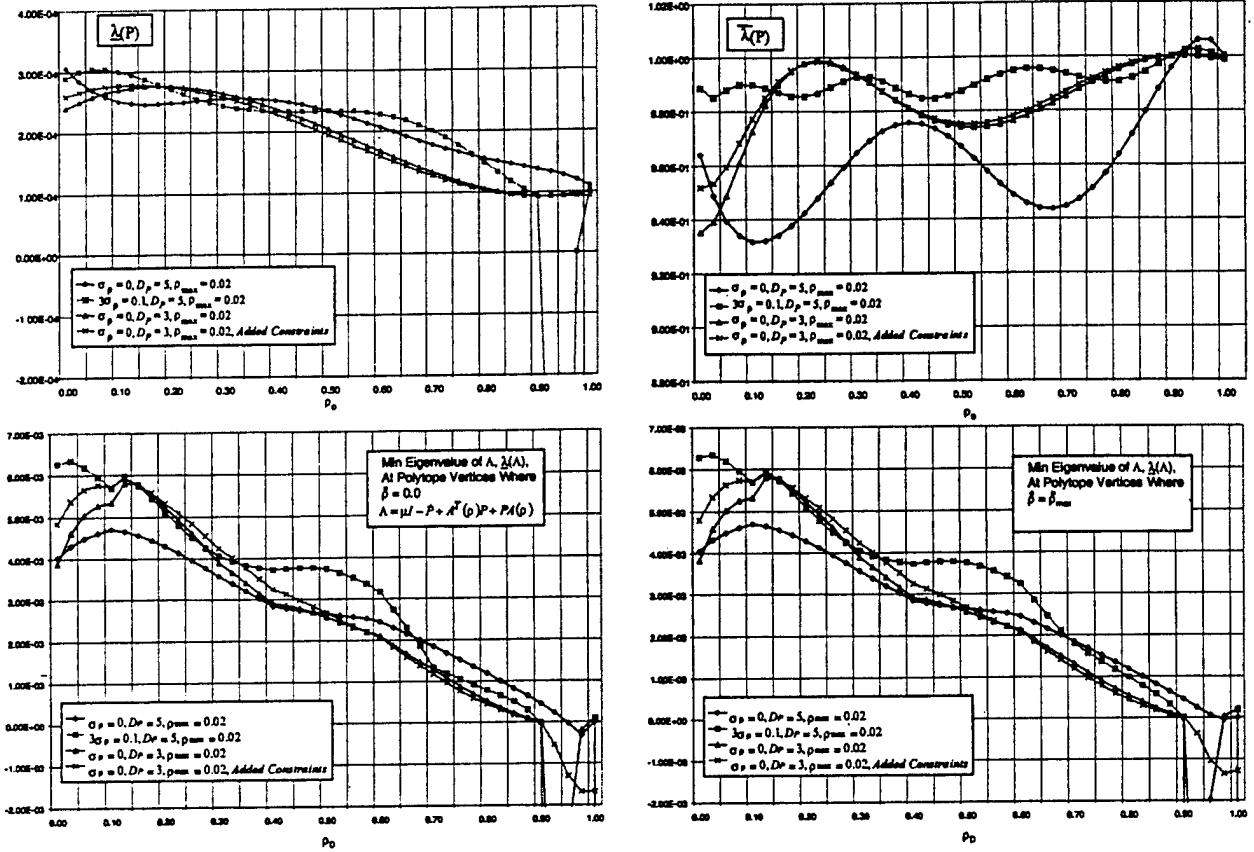


Figure 3.8 Category III stability analysis results.

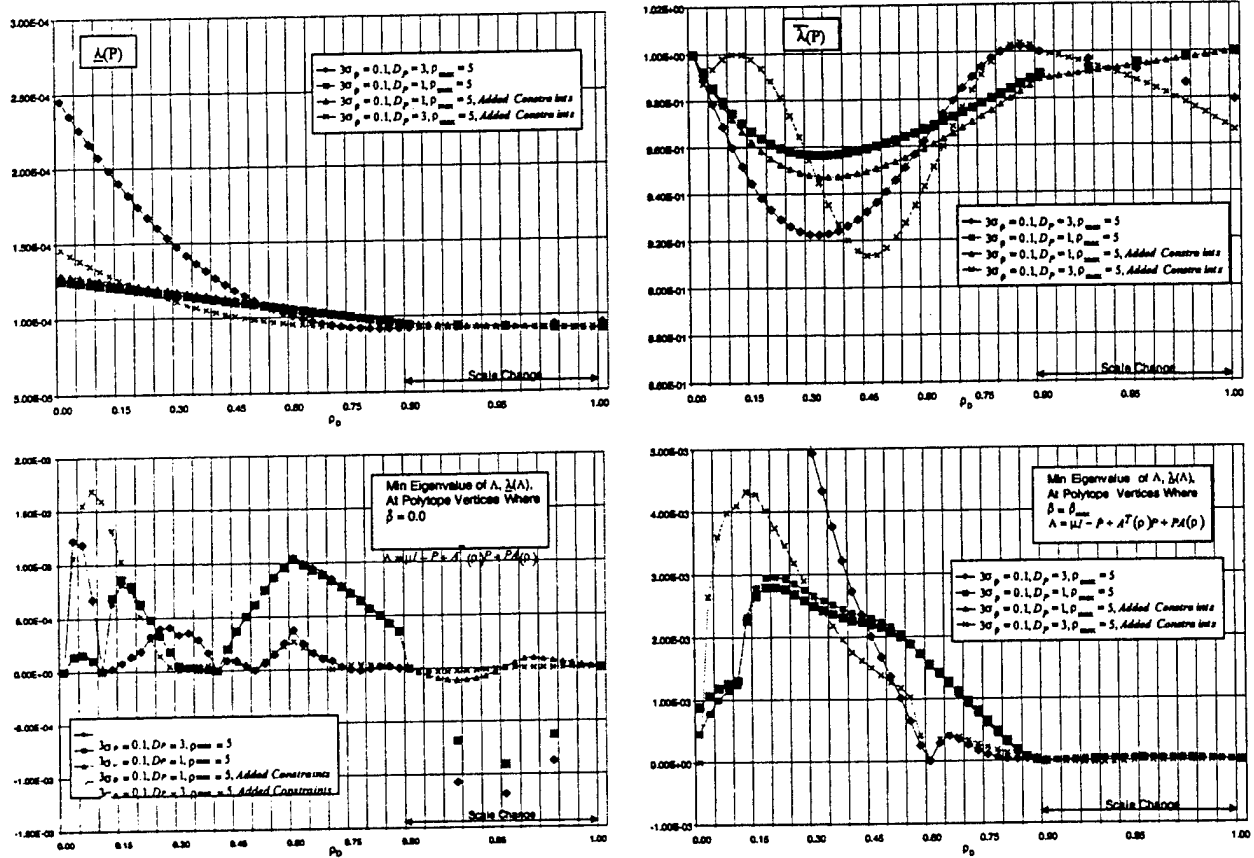


Figure 3.9 Category IV stability analysis results.

### 3.6 Chapter 3 Conclusions

A parameter dependent model of a tailless fighter with battle damage was developed to investigate methods of stability analysis for reconfigurable flight control systems. Stability analysis methods using linear matrix inequalities were presented for parameter dependent models characterized by their scheduling parameters. Four categories of scheduling parameters were discussed along with their respective analysis method. For reconfigurable control systems that can be modeled within this framework, the linear matrix inequalities approach used for stability analysis provides a proof of stability for the gain scheduled control system.

### 3.7 Chapter 3 References

1. J.S. Brinker and K.A. Wise, "Reconfigurable Flight Control for a Tailless Advanced Fighter Aircraft," Proc. Of the 1998 AIAA GNC Conference.
2. Gahinet, P. and P. Apkarian, "A Linear Matrix Inequality Approach To  $H^\infty$  Control," Int. Journal of Robust and Nonlinear Control, Vol. 4, pp. 421-448, 1994.
3. Wu, Fen, X.H. Yang, A. Packard, and G. Becker, "Induced L2-Norm Control for LPV System with Bounded Parameter Variation Rates," Int. Journal of Robust and Nonlinear Control, Vol. 4, 1994.
4. S. Boyd, L. El Ghaoui, E. Feron, and V. Balakrishnan, *Linear Matrix Inequalities in System and Control Theory*, SIAM, Philadelphia PA, 1994.
5. G. Becker, A. Packard, D. Philbrick, and G. Balas, "Control of Parametrically-Dependent Linear Systems: A Single Quadratic Lyapunov Approach," Proc. of the ACC, San Francisco CA, June 1993, pp. 2795-2799.
6. G. Becker and A. Packard, "Gain-Scheduled State-Feedback with Quadratic Stability for Uncertain Systems," IEEE CDC, pp. 2702-2703.
7. J. Doyle, A. Packard, K. Zhou, "Review of LFTs, LMIs, and  $\mu$ ," Proc. of the IEEE CDC, Brighton England, Dec. 1991, pp. 1227-1232.
8. K.A. Wise, "Bank-to-Turn Missile Autopilot Design Using Loop Transfer Recovery", AIAA Journal of Guidance, Control, and Dynamics, Vol. 13, No. 1, Jan-Feb 1990, pp. 145-152.

9. K.A. Wise and F. Deylami, "Approximating a Linear Quadratic Missile Autopilot Design Using an Output Feedback Projective Control", Proc. of the AIAA Guidance, Navigation, and Control Conference, New Orleans, LA, Aug. 1991, p 114-122, AIAA Paper No. 91-2613.

## **Chapter 4**

### **Aeroservoelastic Filter Design and Optimization Using LMIs**

#### **4.1 Introduction**

This chapter presents the development of a LMI based tool for optimizing aeroservoelastic filter coefficients used in the filtering inertial measurement signals (angular rates and translational accelerations). Limited success was obtained in developing this tool due to the extremely large sizes of the resulting LMI problems.

#### **4.2 ASE Compensation Filter Design**

The influence of the structural modes on the sensor measurements must be attenuated through the use of aeroservoelastic (ASE) compensation filters prior to use in the control law, since insufficient attenuation of these effects can lead to instability. Under the RESTORE program, linearized models of the ASE dynamics were extracted from the TAFE 6DOF at the high speed and low speed flight conditions, and were used to design ASE compensation filters for the flight control system. Under RESTORE, the ASE compensation filters were designed to gain stabilize the system at frequencies above the first structural mode by providing at least 8 dB of attenuation at these frequencies. Over design of these filters can result in excessive low frequency phase lag which degrades rigid body stability margins and flying qualities. As a result, the filters were designed to meet the high frequency attenuation goals while minimizing low frequency phase lag. The resulting filters are shown in Figure 4.1 and a corresponding frequency response in Figure 4.2.

Frequency responses of the linearized ASE dynamics showed the highest amplitude peaks in the 40-50 rad/s region with slightly lower peaks at higher frequencies. Since the highest peaks were at the lowest resonant frequencies, utilization of low pass filters to provide the required attenuation was not a viable option. A reasonably low order filter (i.e. < 4th order) would require a very low break frequency, which would lead to excessive low frequency phase lag. A notch filter provides a viable method for attenuating the low frequency peaks by concentrating the attenuation in the desired frequency range. Keeping the attenuation band of the notch filter

narrow minimizes the associated low frequency phase lag. Cascading the notch filter with a low pass filter provides attenuation above the notch filter frequency to attenuate higher frequency modes. This filter combination is commonly used in ASE filter design.

The notch - lag filter combinations designed for the TAFE airframe are provided in Figure 4.1. ASE compensation filters were made as common as possible for all signals in a given axis to prevent an adverse performance impact when the signals are blended. An example of this is the calculation of stability axis rates. If the roll rate and yaw rate are processed by filters with different bandwidths and then transformed to stability axis, the resulting signal can differ significantly from a filtered version of the true stability axis rates. Unmatched filters introduce a phase discrepancy between the signals leading to the degraded results. The lag filters used in the lateral directional axis were scheduled with Mach to gain the required structural mode attenuation at low speeds while preserving good rigid body stability margins at high speeds.

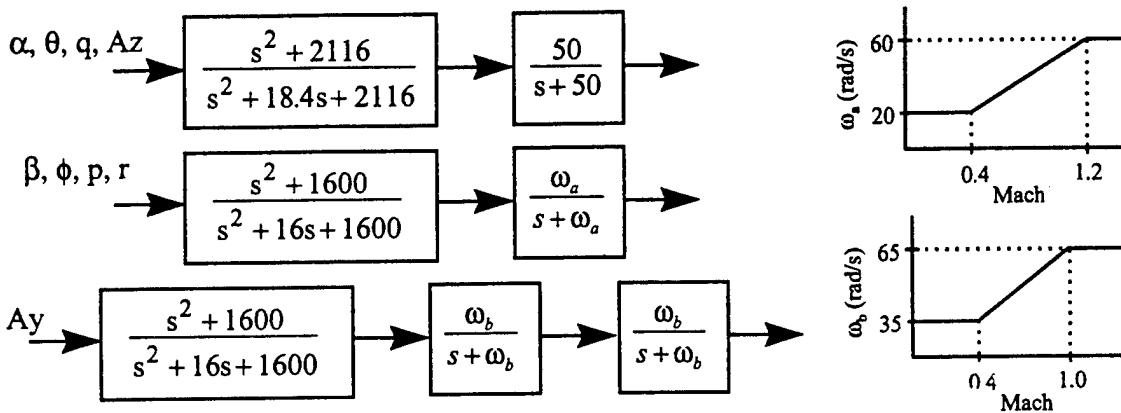


Figure 4.1 TAFE ASE Compensation Filters

An example of the frequency response analysis used to validate the ASE compensation filters is provided in Figure 4.2. This data is for the longitudinal axis at the low altitude ingress / egress flight condition described in Reference 1.

The first row of plots shows the magnitude of the frequency response relating the ASE contribution to sensed pitch rate and normal acceleration to the pitch axis control effector inputs. This data shows high frequency peaks in the frequency response curves which exceed 20 dB,

indicating the need for ASE filtering in the control law design. The highest peaks occur in the 40-50 rad/sec region as discussed above.

The second row of plots shows the open loop frequency response with the loop broken at the actuator for each of the TAFE pitch axis control effectors. The open loop model includes the rigid body and ASE dynamics, linearized TAFE baseline control law, actuator and sensor dynamics, digitization effects, and time delays. ASE compensation filtering was not included in this analysis to determine the need for filtering. The magnitude frequency responses with the loop broken in the trailing edge flap (TEF) and pitch thrust vectoring channels show resonant peaks exceeding 0 dB in the high frequency region (above 20 rad/sec). This indicates insufficient attenuation of the structural modes and the potential for instability (stability depends on the phase characteristics in this frequency band). Since the phase at these frequencies is uncertain, gain stabilization of the structural modes is desired, indicating the need for ASE compensation filtering.

The last row of plots in Figure 4.2 repeats the open loop frequency response analysis with the addition of the ASE compensation filters described in Figure 4.1. These data show that these filters provide the desired attenuation of the structural modes, while maintaining good rigid body stability margins. The loop gain at this flight condition results in no 0 dB gain crossovers, thereby yielding an infinite phase margin. The  $-180^\circ$  phase crossovers occur in the 10 - 20 rad/sec region, yielding gain margins in excess of 10 dB.

These ASE compensation filters were also integrated into the TAFE 6DOF for analysis. Nonlinear simulations with the ASE dynamics described in Appendix A was performed to verify that the closed loop system was unstable prior to incorporation of the ASE compensation filters, and that the desired low order response characteristics (flying qualities) were obtained after the filters were added.

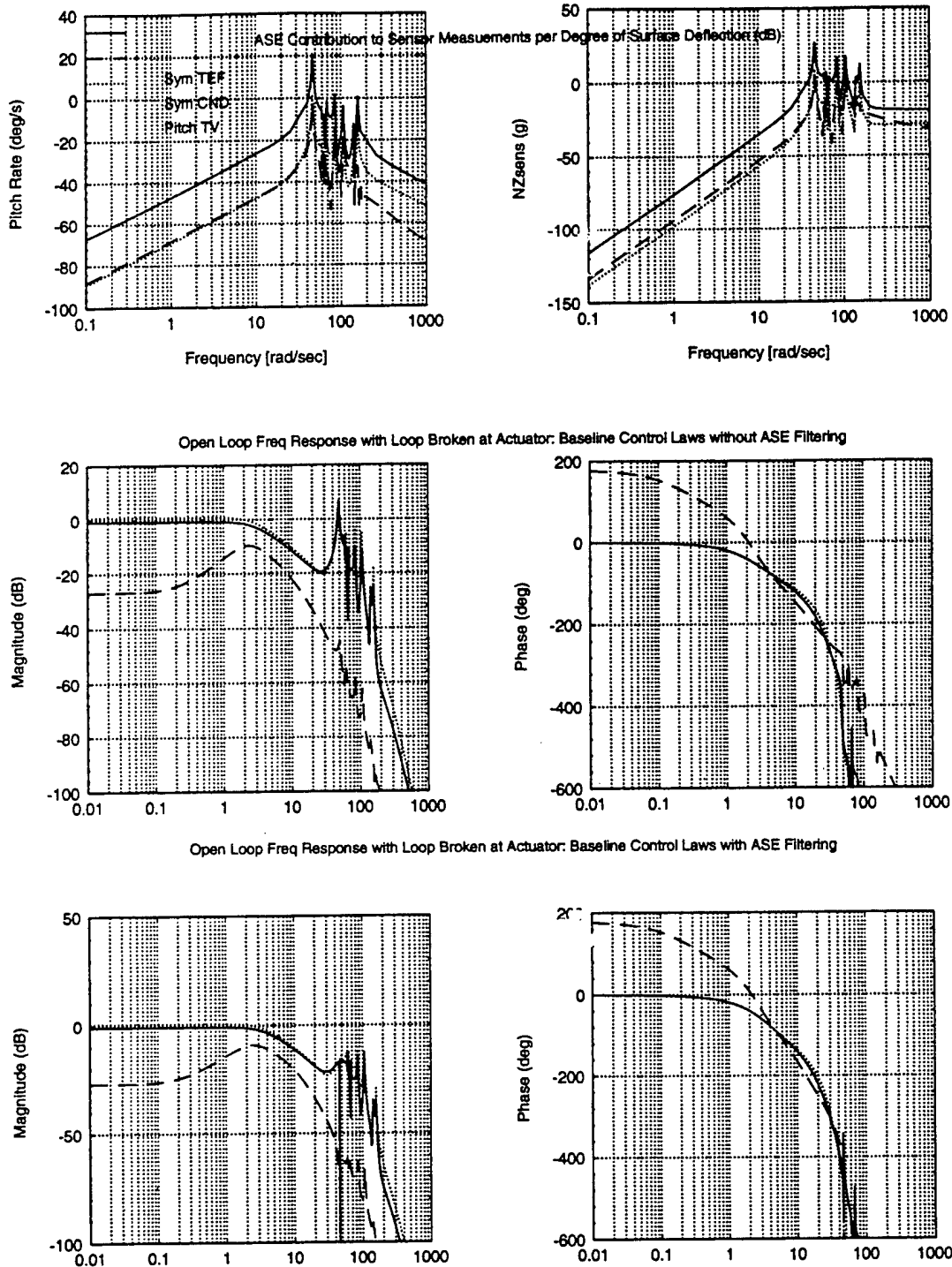


Figure 4.2 Open Loop Frequency Response Analysis to Validate ASE Compensation Filter Design

### 4.3 Optimization of ASE Filter Coefficients

In the Boeing Phantom Works, a tool called COMPASE is typically used to optimize ASE filter coefficients to minimize phase lag at low frequencies, subject to satisfying gain attenuation constraints at the flexible body modes. The input to COMPASE is a worst-case magnitude frequency response built over a range of flight conditions, store loadings, and mass properties. These filters are designed to be robust to the aircraft's configuration so that control law changes are not required when different weapons are loaded onto the aircraft.

COMPASE is a conjugate gradient based optimization tool. It optimizes ASE filter coefficients to provide gain attenuation at the flexible body modes while minimizing phase lag at low frequencies. It is time consuming to use, and sometimes has difficulty in convergence.

The design of ASE filters are in the critical path for developing an aircraft's control laws. Using analytical models for the flexible dynamics, these filters are designed and integrated into the control laws. After completion of ground vibration testing and structural mode testing, these filters are often re-designed based on measured frequency response data. Tool improvements in this area could significantly reduce the costs and schedule associated with the design of the ASE filters.

Boyd [2,3] investigated using LMIs to design finite impulse response filter. Instead of designing the frequency response  $X(\omega)$  of the filter directly, the power spectrum

$R(\omega) = |X(\omega)|^2$  is designed, leading to

find  $R(\omega)$

such that  $L^2(\omega_i) \leq R(\omega_i) \leq U^2(\omega_i)$ ,  $i = 1, \dots, M$

$R(\omega) \geq 0$ ,  $\omega \in \Omega \subseteq [0, 2\pi]$

where  $L(\omega)$  and  $U(\omega)$  are magnitude bounds for the filter,  $L(\omega_i) \leq |X\omega_i| \leq U(\omega_i)$ ,

$i = 1, \dots, M$ . This approach requires  $M$  to be sufficiently large.

The ASE filters for TAFE (Appendix A) are implemented at 600 Hz, which is the rate that the IMU provides data to the flight control system. This data is buffered and processed at 100 Hz to form the feedback measurements for flight control. The high sample rate (600 Hz) creates

a large number of frequencies,  $M$ . As a result the size of the LMI problem grew too large for numerical optimization.

If the sample rate for implementation is lowered, the problem size does become implementable. Figure 4.3 shows the upper bound  $U(\omega)$  and lower bound  $L(\omega)$  frequency responses for a 200 Hz filter design using 52 frequency points ( $M = 52$ ).

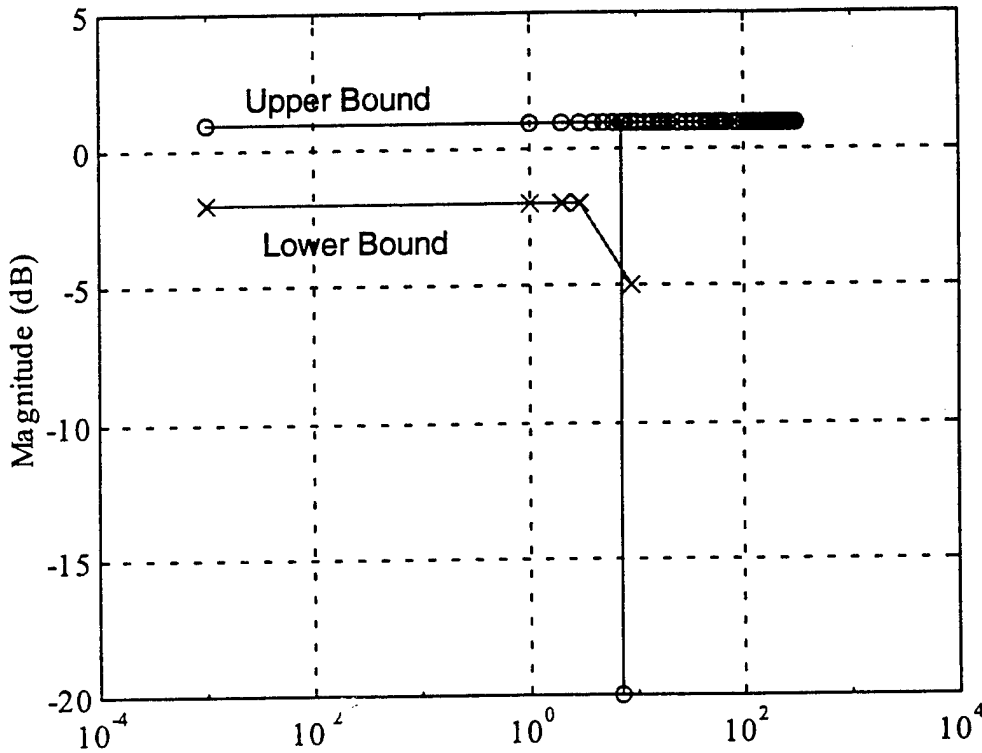


Figure 4.3 200 Hz Filter Design Bounds

The spike at 7.32 inputs the notch required to attenuate the first bending mode. Using these design constraints, the LMI problem was solved optimizing the filter tap coefficients. For a filter with 21 tap coefficients the results were

```
x[0]=0.789425
x[1]=-0.320252
x[2]=0.241448
x[3]=-0.148961
```

```
x[4]=0.060187  
x[5]=-0.027118  
x[6]=0.026300  
x[7]=-0.023576  
x[8]=0.066692  
x[9]=-0.021337  
x[10]=0.026092  
x[11]=0.027752  
x[12]=0.006417  
x[13]=0.058977  
x[14]=0.026731  
x[15]=0.106196  
x[16]=0.011379  
x[17]=0.303340  
x[18]=-0.077172  
x[19]=0.555990  
x[20]=-0.569076
```

Figure 4.4 shows the resulting frequency response.

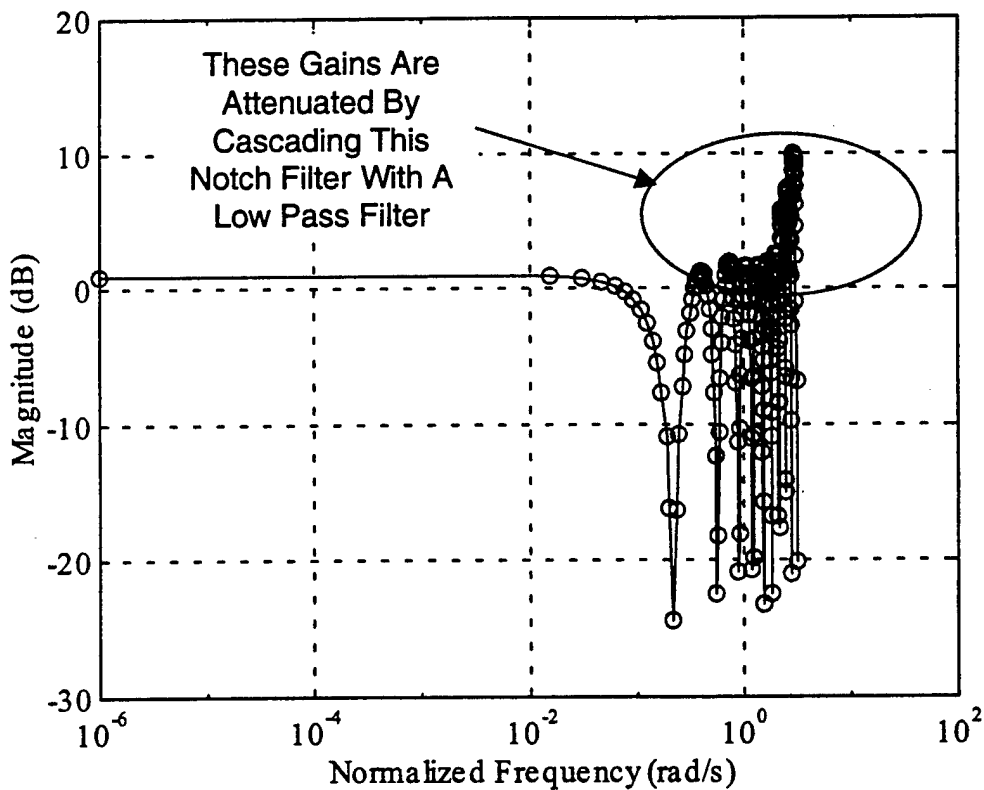


Figure 4.4 200 Hz Filter Frequency Response

Here the notch filter shown in Figure 4.4 would be combined with a low pass filter to roll off the larger gains at the upper frequencies.

#### **4.6 Chapter 4 Conclusions**

Our research in this area has shown that designing FIR filters using LMI tools is feasible. Our application to designing ASE filter coefficients is probably not the best application for this theory. The resulting LMI problems become very large in size and easily exceed the memory of most common work stations. As a result, this does not improve the toolset for the control system designer.

#### **4.7 Chapter 4 References**

1. Reconfigurable Systems For Tailless Fighter Aircraft- RESTORE, Scientific and Technical Reports, Systems Requirements Report, McDonnell Douglas Aerospace, 15 April, 1997.
2. S. Boyd, L. El Ghaoui, E. Feron, and V. Balakrishnan, *Linear Matrix Inequalities in System and Control Theory*, SIAM, Philadelphia PA, 1994.
3. S. Wu, S. Boyd, and L. Vandenberghe, "FIR Filter Design via Semidefinite Programming," Proc. of the ACC, 1996.

## Appendix A

### Boeing Tailless Advanced Fighter Aircraft

The Boeing Tailless Advanced Fighter Aircraft (TAFE), illustrated in Figure A.1, is a conceptual design of an advanced fighter configuration which blends an extensive suite of conventional and innovative control effectors to achieve high agility in a low observable design. The TAFE is a single engine, single seat fighter designed for air to air or air to ground missions.

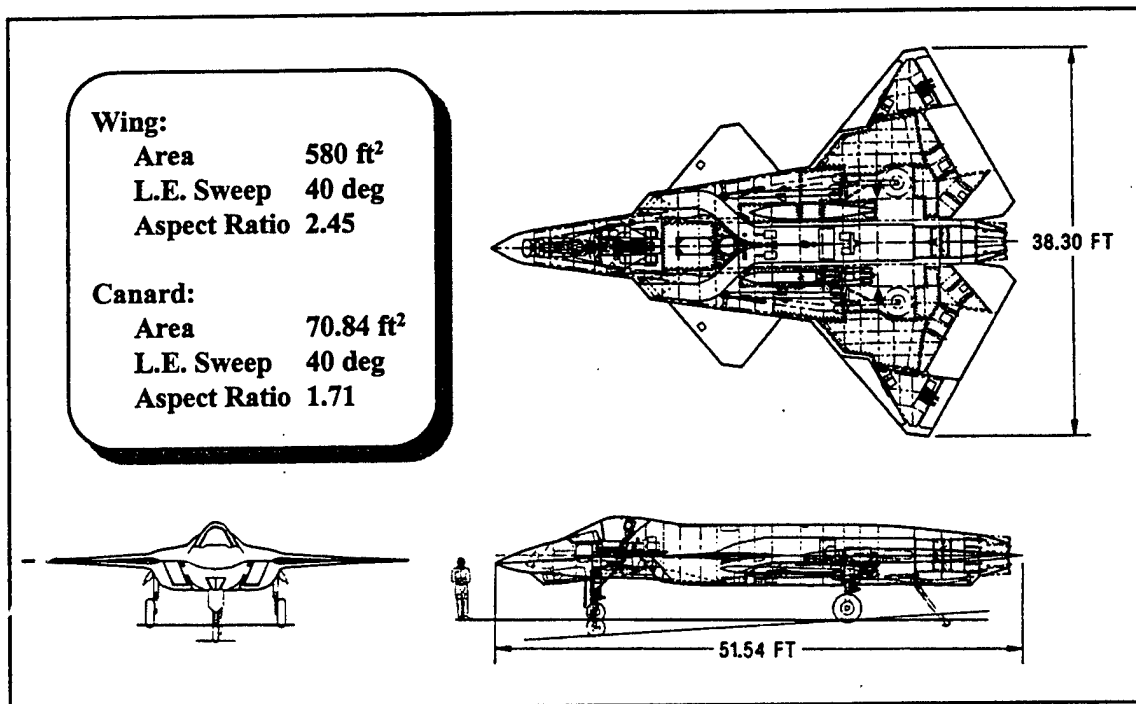


Figure A.1: Three-View of TAFE Aircraft

The TAFE airframe is characterized by a chined forebody, symmetric air inlets, and the lack of a vertical tail. The wing and all moving canard are thin and feature a moderate aft sweep with no dihedral. The wing is equipped with leading edge passive porosity that can be used as a low rate roll control device during covert maneuvers. The passive porosity strip consists of a series

of valves which can be opened to reduce the lift on one wing of the aircraft, thereby producing a roll maneuver.

The trailing edge of the wing features ailerons, trailing edge flaps and aft body split flaps. The trailing edge flaps provide a powerful pitch control effector which can also be deflected differentially to augment the ailerons during rolling maneuvers. If necessary, the flaps and ailerons can be deflected in opposing directions to generate yawing moments without inducing roll. The aft body split flaps are "clamshell" devices which consist of two panels on each side of the aircraft. One panel opens above the wing and the other below the wing to produce yawing moments while inducing very little roll. The all moving canards are used as a low rate trim device for performance optimization, but also provide supplementary yaw control power through differential deflections. In addition, the canards generate substantial nose down control capability to help meet control margin requirements at high angles of attack.

The TAFE is powered by a moderate bypass ratio turbofan engine equipped with axisymmetric thrust vectoring. The pitch and yaw thrust vectoring enhance maneuvering capabilities and stability augmentation. In addition, compressor bleed air is routed to forebody ports for pneumatic control. The ports are mounted to serve as a yaw control device.

The TAFE is designed for fly-by-wire control using hydraulically and electromechanically actuated control effectors. Movable surfaces utilize hydraulic actuators while the pneumatic forebody blowing and leading edge passive porosity employ electromechanical actuators. The system is designed to be tri-redundant on all flight critical sensors and control effectors.

In order to support design, analysis, and simulation of reconfigurable control laws for the TAFE aircraft, a math model was created using the structure shown in Figure A.2. The structure of this model is used for both linear analysis and nonlinear simulation. All components are used for linear analysis. Some of the high frequency effects are excluded from the nonlinear simulation to reduce throughput requirements.

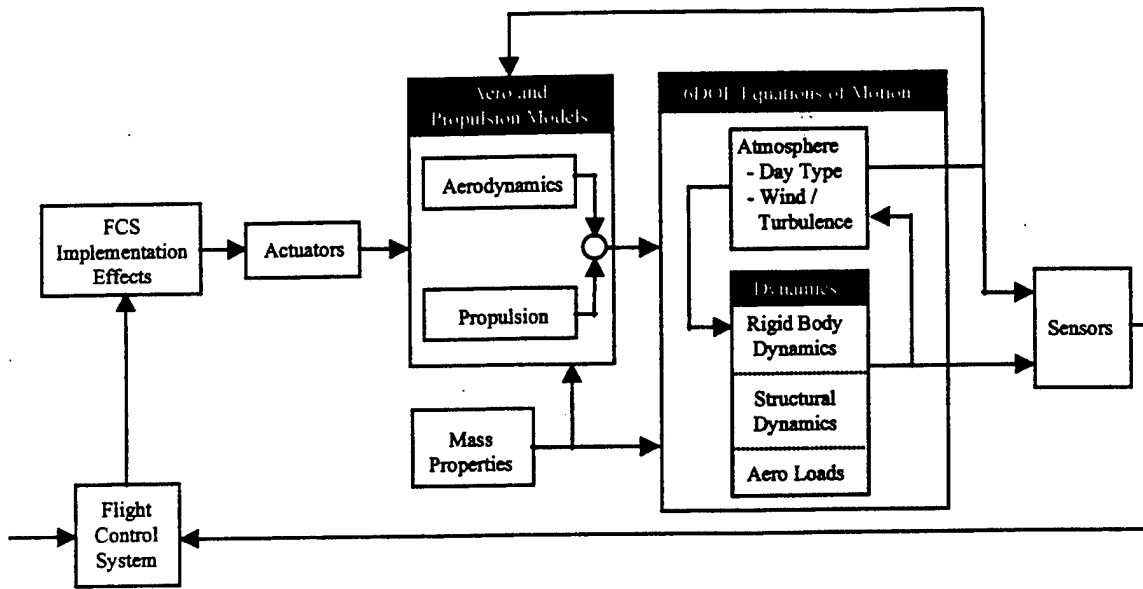


**Figure A.2: Block Diagram of TAFE Analysis / Simulation Model**

The components of Figure A.2, with the exception of the flight control system, describe the TAFE airframe and hardware subsystems. Descriptions of these models are provided in the following sections.

### A.1 Mass Properties Models

The TAFE mass properties model generates the vehicle weight, inertia matrix, center of gravity, and inverse inertia matrix for use by the aerodynamics, propulsion, and equations of motion modules. A static model (i.e. mass properties do not change with fuel burn) is used.

The model supports a variety of vehicle configurations representing different stores and fuel loadings. These are useful in evaluating a flight control design's sensitivity to knowledge of the vehicle's mass properties. The mass property models for the TAFE were taken from the Boeing ASTOVL program, where a similar configuration was explored. The TAFE mass property models are provided in Table A.1.

Configuration	Weight (lb)	I <sub>xx</sub>	I <sub>yy</sub>	I <sub>zz</sub> (slug-ft <sup>2</sup> )	I <sub>xz</sub>	FSeg	BLeg (in)	WLcg
Clean, 2 AIM-9 & 2 AIM-120 internal carry	28064	14578	93604	103855	559	373.5	0	100
VL with 6 AIM-120	30494	22329	97090	114520	-234	379	0	100
Take Off, 2 AIM-9, 2 AIM-120	39684	28154	110616	134103	994	386	0	100
Take Off, 2 GBU-24	43714	45624	115963	115963	-1502	393	0	100
VL, 1 HARM	28448	19195	95202	109372	90	376	-3.23	100
CTOL, 1 1200 lb store	28664	19785	95282	110000	36	377	-4.95	100
Combat Wt, 2 AIM-9, 2 AIM-120, 60% fuel	34569	19245	99692	114355	682	379	0	100

**Table A.1: TAFE Mass Properties Models**

The center of gravity parameters are given in terms of a fuselage station (FS), butt line station (BL) and waterline station (WL). These quantities are measured positive aft from the nose, out the right wing, and up, respectively.

## A.2 Aerodynamics Models

The TAFE aerodynamics model computes the body axis aerodynamic forces and moments acting on the vehicle. Non-dimensional aerodynamic coefficients are computed and dimensionalized based on the vehicle's flight condition and geometry to create the forces and moments. The non-dimensional coefficients are a function of the vehicle's rigid body states, atmospheric conditions, and control surface positions. The moment coefficients are translated to the vehicle's center of gravity. Reductions in control surface effectiveness due to structural flexibility are also modeled.

The TAFE aerodynamics model is based on Boeing wind tunnel testing of a tailless ASTOVL configuration. Control increments for the leading edge passive porosity and forebody blowing were estimated from test data derived on other Boeing programs. The resulting database provides a six degree of freedom aerodynamics model that covers the complete range of flight operations from Mach 0 to 2.5, altitude from 0 to 80,000 ft, angles of attack from -2 to 48 deg, and sideslip angles from -20 to 20 deg. The nonlinear database includes static, dynamic

coupling and control surface effectiveness terms. The aerodynamic effects of external stores are not modeled.

The baseline aerodynamics model computes the non-dimensional force and moment coefficients at the reference center of gravity using Equation (A.1).

$$C_{(\ )} = C_{(\ )_0}(M, \alpha, \beta) + \sum_i C_{(\ )_{\delta_i}}(M, \alpha, \delta_i) K_{F/R_i} + \sum_{i,j} C_{(\ )_{\delta_i \delta_j}}(M, \alpha, \delta_i, \delta_j) + \frac{1}{2V} C_{(\ )_{DYN}} \quad (A.1)$$

The form of this equation is the same for the force and moment coefficients, and thus the ( ) subscript denotes any selected force or moment coefficient: x,y,z, for the axial, lateral, and vertical forces,  $\ell, m, n$  for the roll, pitch, and yaw moments. The terms in Eq. (A.1) are looked up from tables using multi-dimensional linear interpolation.

In Equation (A.1),  $C_{(\ )_0}(M, \alpha, \beta)$  is the controls neutral term which represents the static forces and moments acting on the vehicle when all of the control effectors are at their zero positions. This term is a function of the vehicle's mach  $M$ , angle of attack  $\alpha$  and sideslip  $\beta$ .

The  $\sum_i C_{(\ )_{\delta_i}}(M, \alpha, \delta_i) K_{F/R_i}$  term represents the aerodynamic forces and moments due to deflections of the individual control effectors. The control increments are modeled in terms of individual surface deflections (e.g. left and right) rather than collective and differential deflections to support subsequent integration of failure and damage models. The control increments are scaled by a factor  $K_{F/R_i}$  which represents a loss in control effectiveness due to structural flexibility of the surface and supporting structure. This effect will be discussed in detail in the following section.

An additional term,  $\sum_{i,j} C_{(\ )_{\delta_i \delta_j}}(M, \alpha, \delta_i, \delta_j)$ , models the forces and moments induced by the interaction between control effectors. The deflection of one surface may alter the airflow over another surface, thus altering its effectiveness. This effect is modeled by the controls interaction term.

The final term in the aerodynamic coefficient build up is the dynamic term, which consists of the aerodynamic damping derivatives (e.g.  $C_{n_r}$ ) scaled by their respective rotational rates (e.g.

$r$ ). These terms are scaled by  $l/2V$ , where  $l$  is the reference length and  $V$  is the vehicle's airspeed. The reference length is the mean aerodynamic chord  $\bar{c}$  for the longitudinal plane, and the wing span  $b$  for the lateral directional plane.

The control powers of the various effectors are compared in Figure A.3 at a subsonic flight condition (Mach 0.6). In these plots, the line types (solid, dashed, dotted) on the plots correspond to the order that the effectors are listed in the y-axis label of the plot.

The first row of plots compares the nose up and nose down pitch control power of the trailing edge flaps and canards as a function of angle of attack. The pitching moment increment produced by each control effector is plotted for maximum surface deflections. The trailing edge flaps provide more nose up control power across the angle of attack regime due to the small positive deflection limit on the canard. On the other hand, the canard provides more nose down control power than the trailing edge flap over most of the angle of attack envelope.

The second row of plots compares the roll control power of the ailerons, trailing edge flaps, and leading edge passive porosity. The ailerons and trailing edge flaps are used differentially in this case. The first plot compares the rolling moment coefficient increment generated by maximum deflection of each effector as a function of angle of attack. The trailing edge flaps have the most control power; however, this analysis assumes that all of the deflection capability is available for roll. In reality, the differential trailing edge flap deflection capability may be limited based on the collective deflection utilized for pitch (i.e. the axis prioritization assigned to the control effector). The aileron provides more roll control power than the leading edge passive porosity. At angles of attack above 10 deg, the leading edge passive porosity provides up to half of the aileron control power, thus making it a viable low rate roll device. The second plot compares the linearity of the control powers as a function of deflection (percentage of maximum) at a fixed angle of attack. The aileron and trailing edge flap control powers are piecewise linear with a reduced control derivative at higher deflections. The leading edge passive porosity control power is linear with deflection.

The third row of Figure A.3 compares the yaw control power of the aft body split flaps, canards, and forebody blowing. The canards are used differentially in this case. The first plot compares the yawing moment coefficient increment generated by maximum deflection of each effector as a function of angle of attack. The aft body split flaps are most effective at low angles

of attack, while the forebody blowing is most effective at high angles of attack. The second plot compares the linearity of the control powers as a function of deflection (percentage of maximum) at a fixed angle of attack. The aft body split flap and forebody blowing control powers are linear with deflection, while the differential canard control derivative varies with deflection. The largest control derivative occurs in the low to moderate deflection region.

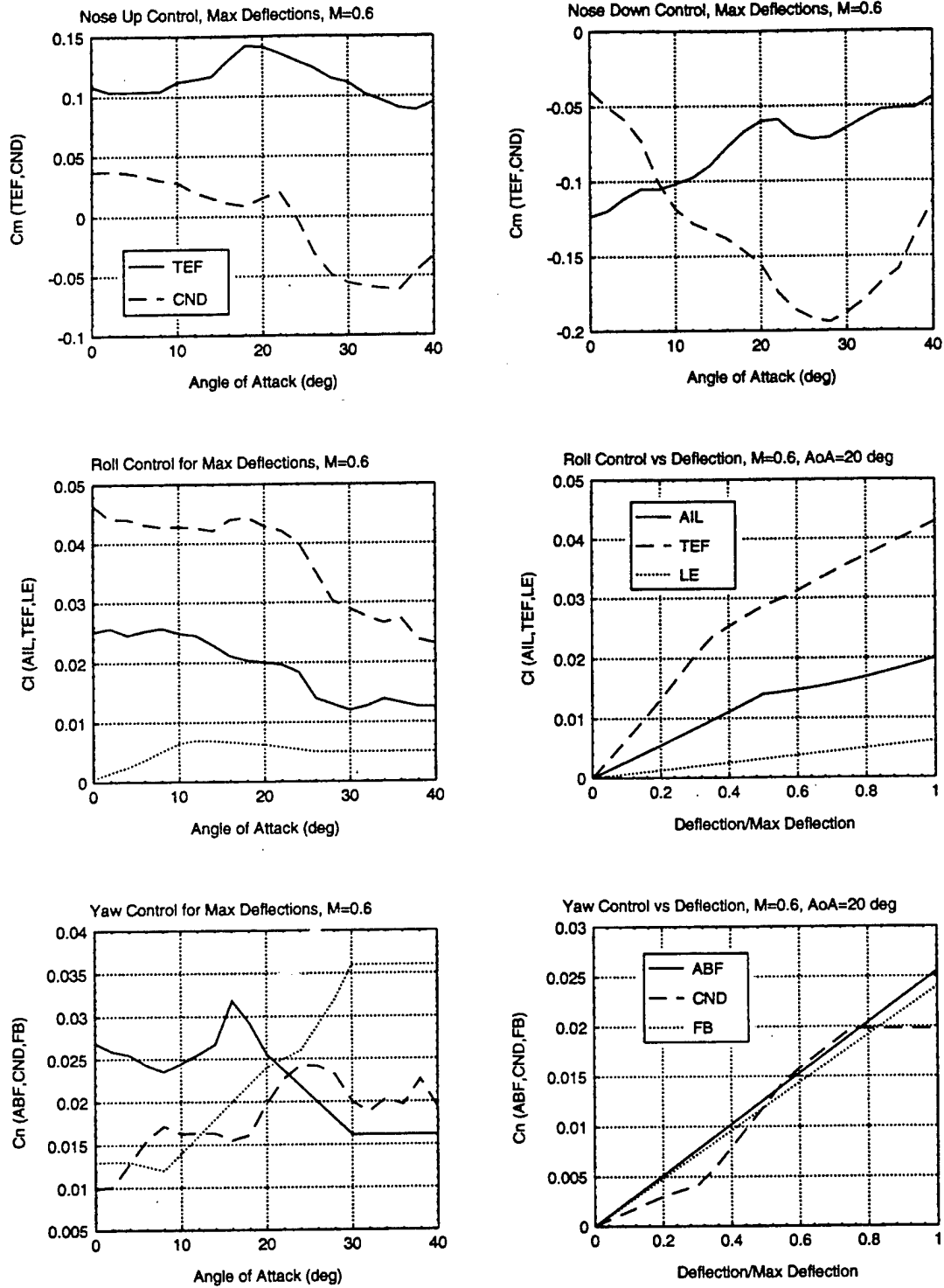


Figure A.3: TAFE Aerodynamic Control Increments

Once the aerodynamic force and moment coefficients are computed at the reference center of gravity, the aerodynamics moments are translated to the actual center of gravity of the vehicle. This consists of calculating the incremental moments induced by the aerodynamic forces acting through a point displaced from the center of gravity. The computation is shown in Equation (A.2).

$$\begin{bmatrix} C_l \\ C_m \\ C_n \end{bmatrix} = \begin{bmatrix} C_l \\ C_m \\ C_n \end{bmatrix}_{\text{ref}} + \begin{bmatrix} 1/b & 0 & 0 \\ 0 & 1/\bar{c} & 0 \\ 0 & 0 & 1/b \end{bmatrix} \left\{ \begin{bmatrix} (FS_{cg} - FS_{ref})/12 \\ -(BL_{cg} - BL_{ref})/12 \\ (WL_{cg} - WL_{ref})/12 \end{bmatrix} \times \begin{bmatrix} C_x \\ C_y \\ C_z \end{bmatrix} \right\} \quad (\text{A.2})$$

The aerodynamic force and moment coefficients are then dimensionalized to form forces and moments using the vehicle geometry and dynamic pressure. The force and moment equations are summarized in Equation (A.3).

$$\begin{aligned} F_x &= \bar{q}SC_x & L &= \bar{q}SbC_l \\ F_y &= \bar{q}SC_y & M &= \bar{q}S\bar{c}C_m \\ F_z &= \bar{q}SC_z & N &= \bar{q}SbC_n \end{aligned} \quad (\text{A.3})$$

The forces ( $F_x, F_y, F_z$ ) are in lbs, and the moments ( $L, M, N$ ) are in ft-lbs.

The airframe geometry constants for the TAFE aircraft are provided in Table A.2.

TAFE Airframe Geometry Constants	
$FS_{ref} = 382 \text{ in}$	$S = 590 \text{ ft}^2$
$BL_{ref} = 0 \text{ in}$	$b = 37.98 \text{ ft}$
$WL_{ref} = 100 \text{ in}$	$\bar{c} = 19.415 \text{ ft}$

Table A.2: TAFE Airframe Geometry Constants

### **A.2.1 Aerodynamic Flexibility Effects**

The aerodynamic flexibility effects model a reduction in control effectiveness due to structural flexibility of the control surface and supporting structure. Derivation of these effects requires a detailed analysis of the aerodynamics loads and the structural characteristics of the vehicle. This data was not available for the TAFE aircraft and thus the aerodynamic flexibility effects from the F-15 ACTIVE aircraft were used.

The aerodynamic flexibility model reduces the control effectiveness as a result of wing / surface flexure under the aerodynamic loads. The actuator takes the surface to its commanded position; however, the "effective" position (relative to the air stream) is less due to flexing of the wing and/or surface. This effect is modeled as a scale factor on the control surface aerodynamic increments.

For the TAFE platform, the aerodynamic flexibility effects are most prominent on the trailing edge flap and aileron effectors. The aft body split flaps consist of two panels (on each side of the aircraft), one of which opens above the wing and the other below the wing. The panels tend to produce torsional moments on the wing in opposite directions. These torsional moments cancel each other to nullify wing flexure due to their aerodynamic loads on the aft body split flap panels. Aerodynamic flexibility of the canards is not expected to be significant due to their low aspect ratio and moderate leading edge sweep. These factors tend to produce a small angular deviation of the elastic axis of the surface from the vehicle centerline, thus minimizing changes in the local angle of attack of the surface due to flexure. Aerodynamic flexibility does not affect the leading edge passive porosity or forebody blowing since these effectors since they do not utilize hinged surfaces operating in the air stream.

As a result, the aerodynamic flexibility effects are applied to the trailing edge flaps and ailerons only. The control power reduction is reflected in all axes, and is characterized by the flex-to-rigid scale factor ( $K_{F/R}$ ) shown in Figure A.4. The scale factor is commonly a function of mach and altitude to reflect movement in the surface center of pressure with mach, as well as variations in loads with changes in dynamic pressure.

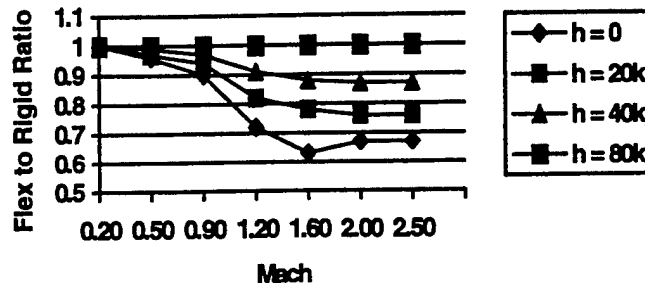


Figure A.4: TAFE Aerodynamic Flexibility Effect Model

### A.3 Propulsion Model

The TAFE propulsion system model computes the body axis forces and moments induced by the engine's gross thrust, the ram drag of the engine inlet, and the nozzle thrust vectoring angles. The model is static and is a function of the power lever angle (PLA), the aircraft rigid body states (rotational rate, angle of attack, sideslip, and velocity), and the aircraft mass properties and geometry data. Nozzle dynamics are modeled in the actuation system.

The propulsion model is based on tabulated steady-state performance data of a moderate bypass ratio turbofan engine. The gross thrust and ram drag data is interpolated from these tables based on the aircraft's Mach number, altitude, and PLA. The propulsion data is shown in Figure A.5 for reference.

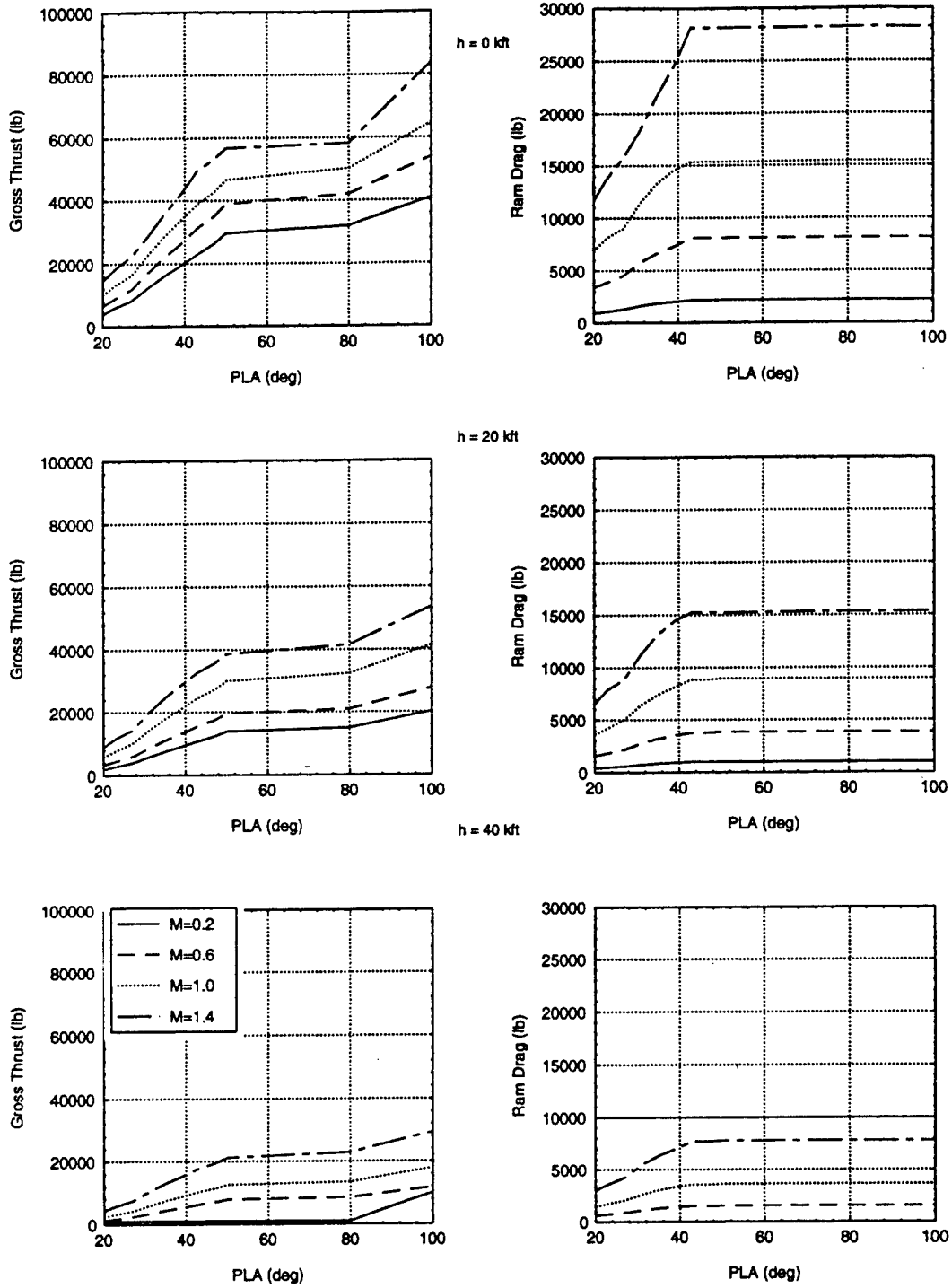


Figure A.5: TAFE Propulsion System Data

The engine gross thrust ( $F_G$ ) data is resolved to the engine axes by transforming it through the thrust vectoring angles. The axi-symmetric nozzle deflection is modeled via pitch ( $\delta_{TVp}$ ) and yaw ( $\delta_{TVy}$ ) vectoring angles. Sequential orthogonal transformations through the yaw and pitch vectoring angles resolve forces from engine to nozzle axes, as illustrated in Figure A.6.

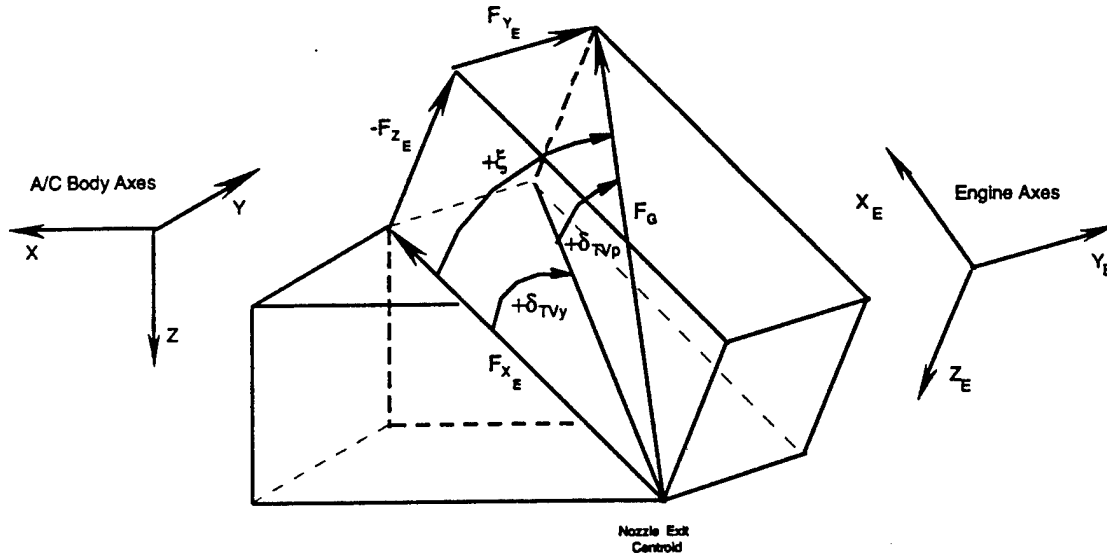


Figure A.6: Relationship Between Engine and Nozzle Axes

The propulsive forces, in engine axes, are defined in terms of the engine gross thrust and vectoring angles as

$$\begin{aligned} F_{X_E} &= F_G \cos(\delta_{TVp}) \cos(\delta_{TVy}) \\ F_{Y_E} &= F_G \cos(\delta_{TVp}) \sin(\delta_{TVy}) \\ F_{Z_E} &= F_G \sin(\delta_{TVp}) \end{aligned} \quad (A.4)$$

The body axis propulsive forces and moments are formed from gross thrust and inlet (ram) drag contributions. The gross thrust forces are transformed from engine axes to body axes via rotations through the engine installation angles. These angles represent the orientation of the engine with respect to the vehicle body axes. The transformation from body axes to engine axes is accomplished via sequential rotations through the engine yaw ( $\psi_E$ ) and pitch ( $\theta_E$ )

installation angles. The roll orientation of the engine is assumed to be coincident with the body. The body axis forces due to gross thrust are defined as

$$\begin{bmatrix} F_{X_G} \\ F_{Y_G} \\ F_{Z_G} \end{bmatrix} = \begin{bmatrix} \cos(\theta_E) \cos(\psi_E) & -\sin(\psi_E) & \sin(\theta_E) \cos(\psi_E) \\ \cos(\theta_E) \sin(\psi_E) & \cos(\psi_E) & \sin(\theta_E) \sin(\psi_E) \\ -\sin(\theta_E) & 0 & \cos(\theta_E) \end{bmatrix} \begin{bmatrix} F_{X_E} \\ F_{Y_E} \\ F_{Z_E} \end{bmatrix}. \quad (A.5)$$

Moments due to gross thrust are computed based on the gross thrust forces and the offset between the thrust centerline and the vehicle center of gravity. This yields

$$\begin{bmatrix} M_{L_G} \\ M_{M_G} \\ M_{N_G} \end{bmatrix} = \bar{r} \times \bar{F}_G = \begin{bmatrix} -(FS_{NOZ} - FS_{cg})/12 \\ (BL_{NOZ} - Bl_{cg})/12 \\ -(WL_{NOZ} - WL_{cg})/12 \end{bmatrix} \times \begin{bmatrix} F_{X_G} \\ F_{Y_G} \\ F_{Z_G} \end{bmatrix}. \quad (A.6)$$

The ram drag forces and moments are comprised of a static and a dynamic contribution. The static forces and moments are dependent on the vehicle's angle of attack and sideslip, while the dynamic forces and moments depend on the vehicle's rotational rates.

The ram drag static forces are computed from the inlet ram drag ( $D_{ram}$ ) and the vehicle's angle of attack and sideslip as

$$\begin{bmatrix} F_{X_{ram}} \\ F_{Y_{ram}} \\ F_{Z_{ram}} \end{bmatrix} = \begin{bmatrix} -D_{ram} * \cos(\alpha) * \cos(\beta) \\ -D_{ram} * \sin(\beta) \\ -D_{ram} * \sin(\alpha) * \cos(\beta) \end{bmatrix}. \quad (A.7)$$

The static ram drag moments are based on the ram drag forces and the inlet location relative to the vehicle's center of gravity, and are computed as

$$\begin{bmatrix} M_{L_{ram}} \\ M_{M_{ram}} \\ M_{N_{ram}} \end{bmatrix} = \bar{r} \times \bar{F}_{ram} = \begin{bmatrix} -(FS_{ram} - FS_{cg})/12 \\ (BL_{ram} - Bl_{cg})/12 \\ -(WL_{ram} - WL_{cg})/12 \end{bmatrix} \times \begin{bmatrix} F_{X_{ram}} \\ F_{Y_{ram}} \\ F_{Z_{ram}} \end{bmatrix}. \quad (A.8)$$

The dynamic ram drag forces are based on the vehicle's ram drag, rotational rates (p, q, r) and airspeed (V), and are computed as

$$\begin{bmatrix} F_{X_{inl}} \\ F_{Y_{inl}} \\ F_{Z_{inl}} \end{bmatrix} = -\frac{D_{ram}}{V} [\bar{r} \times \bar{\omega}] = -\frac{D_{ram}}{V} \begin{bmatrix} -(FS_{inl} - FS_{cg})/12 \\ (BL_{inl} - Bl_{cg})/12 \\ -(WL_{inl} - WL_{cg})/12 \end{bmatrix} \times \begin{bmatrix} p \\ q \\ r \end{bmatrix}. \quad (A.9)$$

The dynamic ram drag moments are computed from the dynamic ram drag forces based on the location of the inlet relative to the vehicle's center of gravity. The computations are summarized below.

$$\begin{bmatrix} M_{L_{inl}} \\ M_{M_{inl}} \\ M_{N_{inl}} \end{bmatrix} = \bar{r} \times \bar{F}_{inl} = \begin{bmatrix} -(FS_{inl} - FS_{cg})/12 \\ (BL_{inl} - Bl_{cg})/12 \\ -(WL_{inl} - WL_{cg})/12 \end{bmatrix} \times \begin{bmatrix} F_{X_{inl}} \\ F_{Y_{inl}} \\ F_{Z_{inl}} \end{bmatrix}. \quad (A.10)$$

The total propulsive forces and moments are formed by summing the gross thrust, static ram drag, and dynamic ram drag contributions. The TAFE propulsion mode constants are provided in Table A.3.

TAFE Propulsion Model Constants	
FS <sub>noz</sub> = 587.61 in	FS <sub>ram</sub> = 208.87 in
BL <sub>noz</sub> = 0 in	BL <sub>ram</sub> = 0 in
WL <sub>noz</sub> = 100 in	WL <sub>ram</sub> = 83.23 in
FS <sub>inl</sub> = 208.87 in	θ <sub>E</sub> = 0 deg

BL <sub>inl</sub> = 0 in	ψ <sub>E</sub> = 0 deg
WL <sub>inl</sub> = 83.23 in	

Table A.3: TAFE Propulsion Model Constants

#### A.4 Rigid Body Dynamics

The TAFE Rigid Body Dynamics model implements the rigid body six degree of freedom equations of motion. The translational dynamics are propagated in an inertial reference frame, while the rotational dynamics are propagated via quaternions. Additional dynamic parameters are computed and output from the model. The model supports flat earth equations of motion. The inputs to the model are the total body axis forces and moments acting on the vehicle, as well as the vehicle mass properties.

The TAFE Rigid Body Dynamics model first computes the translational (linear) and rotational accelerations acting on the vehicle. To compute the linear acceleration, the acceleration due to specific forces is first computed as

$$\mathbf{f}^B / m \quad (\text{A.11})$$

where  $m$  is the vehicle mass. This is the total acceleration due to external forces, excluding gravity. Note that the specific force vector is expressed in the body frame. The specific force is transformed to the inertial frame and added to gravity to form the total linear acceleration of the vehicle, expressed in the inertial frame.

$$\mathbf{a}' = \mathbf{g}' + \mathbf{C}'_B (\mathbf{f}^B / m) \quad (\text{A.12})$$

The body-to-inertial transformation matrix  $\mathbf{C}'_B$  is computed from the body-to-inertial attitude quaternion  $\mathbf{q}'_B = (q_0, q_1, q_2, q_3)$ .

$$\mathbf{C}'_B = \begin{bmatrix} q_0^2 + q_1^2 - q_2^2 - q_3^2 & 2(q_1q_2 - q_0q_3) & 2(q_1q_3 + q_0q_2) \\ 2(q_1q_2 + q_0q_3) & q_0^2 - q_1^2 + q_2^2 - q_3^2 & 2(q_2q_3 - q_0q_1) \\ 2(q_1q_3 - q_0q_2) & 2(q_2q_3 + q_0q_1) & q_0^2 - q_1^2 - q_2^2 + q_3^2 \end{bmatrix} \quad (\text{A.13})$$

Since the body-to-inertial transformation is available here, the gravity vector is also transformed to the body frame for use elsewhere.

$$\mathbf{g}^B = \mathbf{C}_I^B \mathbf{g}^I = (\mathbf{C}_B^I)^T \mathbf{g}^I \quad (\text{A.14})$$

The angular acceleration of the vehicle, expressed in the body frame, is computed as

$$\bar{\omega}^B \equiv \begin{bmatrix} \dot{P} \\ \dot{Q} \\ \dot{R} \end{bmatrix} = \mathbf{I}^{-1} (\mathbf{m}^B - \bar{\omega}^B \times \mathbf{I} \bar{\omega}^B) \quad (\text{A.15})$$

where  $\mathbf{I}$  is the inertia matrix.

The vehicle linear and angular accelerations are then integrated to produce velocity, position, angular rate, and attitude. The linear inertial acceleration vector is integrated to produce a linear inertial velocity vector.

$$\mathbf{v}^I = \int \mathbf{a}^I dt \quad (\text{A.16})$$

The linear inertial velocity vector is integrated to produce an inertial position vector.

$$\mathbf{r}^I = \int \mathbf{v}^I dt \quad (\text{A.17})$$

The angular acceleration vector is integrated to produce an angular velocity vector.

$$\bar{\omega}^B = \begin{bmatrix} P \\ Q \\ R \end{bmatrix} = \int \bar{\omega}^B dt \quad (\text{A.18})$$

Using the body attitude quaternion, the angular velocity vector is transformed to form an attitude quaternion rate

$$\dot{\mathbf{q}}_B^I = \frac{1}{2} \dot{\mathbf{q}}_B^I \bar{\omega}_{IB}^B = \frac{1}{2} \begin{bmatrix} 0 & -P & -Q & -R \\ P & 0 & R & -Q \\ Q & -R & 0 & P \\ R & Q & -P & 0 \end{bmatrix} \begin{bmatrix} q_0 \\ q_1 \\ q_2 \\ q_3 \end{bmatrix} \quad (\text{A.19})$$

which is integrated to produce a body attitude quaternion

$$\mathbf{q}_B^I = \int \dot{\mathbf{q}}_B^I dt. \quad (\text{A.20})$$

In all cases, the preceding vector integrals are reducible to independent scalar integrals on the components of the vectors. The scalar integrals are evaluated numerically using the integration method and time step selected by the user.

The TAFA Rigid Body Dynamics model then converts the vehicle state vector elements from the inertial frame to a geographic (local level) frame according to the Earth model. The Flat

Earth model assumes that the inertial coordinate frame used in propagating the state vector is the geographic, North-East-Down coordinate frame. It simply passes the position and velocity vectors through, renaming their elements to North, East, Down, and  $V_n$ ,  $V_e$ ,  $V_d$  respectively. The body-to-inertial attitude quaternion is also passed through and renamed to the body-to-geographic attitude quaternion. The position vector is transformed to Latitude, Longitude, Altitude (Latitude and Longitude are computed from the North and East positions divided by the earth radius, while Altitude is computed as -Down). Finally, the gravity vector for the Flat Earth model is computed, which is just a constant  $[0, 0, 32.174]$  ft/s/s.

Once the dynamics propagation is completed, additional useful quantities are computed which may be required as flight control feedback or inputs to sensor models. The North-East-Down components of the vehicle velocity are used to compute the vehicle's speed (velocity magnitude) and the flight path angles. The speed is computed as

$$Velocity\_fps = \|\mathbf{v}_B^{NED}\| = \sqrt{(V_N^2 + V_E^2 + V_D^2)} \quad (A.21)$$

The vertical flight path angle is computed as

$$\gamma = \sin^{-1}\left(\frac{-V_D}{Velocity\_fps}\right), \quad (A.22)$$

while the heading (horizontal flight path) angle is computed as

$$\chi = \tan^{-1}\left(\frac{V_E}{V_N}\right). \quad (A.23)$$

The wind velocity  $\mathbf{v}_W^{NED}$  at the vehicle's location, which is the velocity of the local air mass, is used to compute the vehicle velocity with respect to the air.

$$\mathbf{v}_{B\text{air}}^{NED} = \mathbf{v}_B^{NED} - \mathbf{v}_W^{NED} \quad (A.24)$$

This air-relative velocity is transformed to the body frame to form the body-frame air-relative velocity,

$$\mathbf{v}_{B\text{air}}^B = \begin{bmatrix} U\_wrt\_air \\ V\_wrt\_air \\ W\_wrt\_air \end{bmatrix}, \quad (A.25)$$

which is subsequently used to compute aerodynamic angles and rates.

The geographic-to-body transformation matrix  $C_G^B$  is computed from the body-to-geographic transformation quaternion  $q_B^G = (q_0, q_1, q_2, q_3)$ . A matrix transpose is included in the calculation to produce a matrix which will transform in the opposite sense as the quaternion.

$$C_G^B = \begin{bmatrix} q_0^2 + q_1^2 - q_2^2 - q_3^2 & 2(q_1q_2 + q_0q_3) & 2(q_1q_3 - q_0q_2) \\ 2(q_1q_2 - q_0q_3) & q_0^2 - q_1^2 + q_2^2 - q_3^2 & 2(q_2q_3 + q_0q_1) \\ 2(q_1q_3 + q_0q_2) & 2(q_2q_3 - q_0q_1) & q_0^2 - q_1^2 - q_2^2 + q_3^2 \end{bmatrix} \quad (A.26)$$

The geographic frame is the same as the North-East-Down frame, so the geographic-to-body transformation matrix  $C_G^B$  can be used as a North-East-Down-to-body transformation matrix  $C_{NED}^B$ . The matrix is used to transform the body velocity and the body air-relative velocity to the body frame.

$$\mathbf{v}_B^B = C_G^B \mathbf{v}_B^{NED}$$

$$\begin{bmatrix} U \\ V \\ W \end{bmatrix} = C_G^B \begin{bmatrix} V_N \\ V_E \\ V_D \end{bmatrix} \quad (A.27)$$

$$\mathbf{v}_{B\text{air}}^B = C_G^B \mathbf{v}_{B\text{air}}^{NED}$$

$$\begin{bmatrix} U_{\text{wrt\_air}} \\ V_{\text{wrt\_air}} \\ W_{\text{wrt\_air}} \end{bmatrix} = C_G^B \begin{bmatrix} V_{N\text{wrt\_air}} \\ V_{E\text{wrt\_air}} \\ V_{D\text{wrt\_air}} \end{bmatrix}$$

The rate of change of the body components of velocity are computed using the Coriolis equation,

$$\dot{\mathbf{v}}_B^B = (d\mathbf{v} / dt)^B - \bar{\omega}^B \times \mathbf{v}_B^B$$

$$\begin{bmatrix} \dot{U} \\ \dot{V} \\ \dot{W} \end{bmatrix} = \mathbf{a}^B - \bar{\omega}^B \times \mathbf{v}_B^B \quad (A.28)$$

where

$$\mathbf{a}^B = \mathbf{f}^B / m + \mathbf{g}^B. \quad (A.29)$$

The Euler angles describing the orientation of the body relative to the local level, North-East-Down frame are computed from elements of the geographic-to-body transformation matrix.

$$\begin{aligned}
 \text{Roll} = \Phi &= \text{ATAN2}(C_G^B(2,3), C_G^B(3,3)) \\
 \text{Pitch} = \Theta &= \sin^{-1}(-C_G^B(1,3)) \\
 \text{Yaw} = \Psi &= \text{ATAN2}(C_G^B(1,2), C_G^B(1,1))
 \end{aligned}
 \tag{A.30}$$

The ATAN2 function is the four-quadrant arctangent function. To prevent an argument error due to numerical round off errors, the argument of the arcsine function is limited to the range  $\pm 1$  inclusive.

The vehicle's air-relative velocity and its acceleration and angular rate are used to compute the true airspeed, aerodynamic angles, and aerodynamic angle rates. Two of the aerodynamic angles (angle of attack and sideslip) are then used to transform the body angular velocity vector to the wind axes coordinate frame. Because the wind frame is a rotating frame, this is not the body angular velocity with respect to the wind frame, but merely the projection of the body angular velocity into the wind frame.

$$\begin{bmatrix} P_w \\ Q_w \\ R_w \end{bmatrix} = C_B^W \bar{\omega}^B = \begin{bmatrix} \cos \beta \cos \alpha & \sin \beta & \cos \beta \sin \alpha \\ -\sin \beta \cos \alpha & \cos \beta & -\sin \beta \sin \alpha \\ -\sin \alpha & 0 & \cos \alpha \end{bmatrix} \begin{bmatrix} P \\ Q \\ R \end{bmatrix}
 \tag{A.31}$$

The true airspeed is computed as

$$V_{TAS} = \text{Airspeed\_fps} = \|v_{Bair}^B\|
 \tag{A.32}$$

The aerodynamic angles are computed as follows.

$\alpha = \text{ATAN2}(W, U)$	Angle of attack
$\beta = \sin^{-1}(V / V_{TAS})$	Sideslip angle
$\beta_B = \text{ATAN2}(V, U)$	"Body" Sideslip angle
$\alpha_T = \cos^{-1}(U / V_{TAS})$	Total angle of attack
$\alpha_r = \cos^{-1}(U / V_{TAS})$	Aerodynamic roll angle

To prevent an argument error due to numerical round off errors, the argument of the inverse sine and inverse cosine functions are limited to the range  $\pm 1$  inclusive. If Airspeed is zero, then sideslip and total angle of attack are set to zero.

The aerodynamic angle rates are undefined if the airspeed is zero. Furthermore, the angle of attack rate and sideslip rate are undefined if the sideslip angle is ninety degrees (causing  $U = W = 0$ ), and the total angle of attack rate is undefined if the total angle of attack is zero (so  $V = W = 0$ ). The rates are set to zero in these circumstances. However, rather than performing an explicit check that values are equal to zero and setting the results to zero, a small value is added to the airspeed and to  $W^2$ . Both of these quantities are greater than or equal to zero; adding a small value to each makes them strictly greater than zero.

$$V_{TAS1} = V_{TAS} + 10^{-6}$$

$$W_1^2 = W^2 + 10^{-6}$$

Using these perturbed quantities in the denominators of the equations for aerodynamic angle rates prevents division by zero errors and gives results of zero in the cases described above. The error introduced is negligible.

The aerodynamic angle rates are computed as

$$\dot{\alpha} = \frac{U\dot{W} - W\dot{U}}{U^2 + W_1^2} \tag{A.33}$$

$$\dot{\beta} = \frac{V_{TAS}\dot{V} - V\dot{V}_{TAS}}{V_{TAS1}\sqrt{(U^2 + W_1^2)}} \tag{A.34}$$

$$\dot{\alpha}_T = \frac{U\dot{V}_{TAS} - V_{TAS}\dot{U}}{V_{TAS1}\sqrt{V^2 + W_1^2}} \tag{A.35}$$

where

$$\dot{V}_{TAS} = \frac{(U, V, W) \cdot (\dot{U}, \dot{V}, \dot{W})}{V_{TAS1}} \tag{A.36}$$

and

$$(\dot{U}, \dot{V}, \dot{W}) = (\mathbf{f} / m + \mathbf{g})^B - \bar{\omega}_{IB}^B \times \mathbf{v}_{B^air}^B \text{ (assumes wind is not time-varying)} \tag{A.37}$$

Finally, load factors are computed from the specific forces acting on the vehicle. The body-frame Normal and Side load factors are computed from the body-frame Z and Y components of specific force respectively.

$$NZCG\_g\_plus\_up = -\frac{\mathbf{f}^B(z)/m}{32.174} \quad (\text{A.38})$$

$$NYCG\_g = \frac{\mathbf{f}^B(y)/m}{32.174} \quad (\text{A.39})$$

The Normal Load Factor is computed from the stability frame Z component of specific force, i.e., the acceleration due to Lift force. The Lift force is found by transforming body-frame X and Z components of specific force by angle of attack.

$$\mathbf{a}^S(z) = L/m = -(\mathbf{f}^B(x)/m)\sin\alpha + (\mathbf{f}^B(z)/m)\cos\alpha \quad (\text{A.40})$$

$$NL\_g = -\frac{\mathbf{a}^S(z)}{32.174} \quad (\text{A.41})$$

### A.5 Flexible Vehicle (Structural) Dynamics

The flexible vehicle dynamics model captures the effects of the vehicle's structural flexibility on the sensor measurements. These effects are dependent on the location of the sensors and the shapes of the various structural modes. The influence of the structural modes on the sensor measurements must be attenuated through the use of aeroservoelastic (ASE) compensation filters prior to use in the control law, since insufficient attenuation of these effects can lead to instability.

Linear analysis is commonly used to evaluate the impact of the structural dynamics on the control system performance and to determine the ASE filtering requirements. Linear models of the ASE dynamics are generated at various flight conditions using an integrated high fidelity model of the vehicle's aerodynamic and structural characteristics. The model determines the excitation of the structural dynamics caused by the aerodynamic and inertial loads acting on the vehicle, and the subsequent impact on sensor measurements. The model also captures the effect of the vehicle's flexure on the rigid body dynamics. The resulting linear ASE dynamics model is then combined with linear models of the rigid body dynamics, control system, and avionics subsystems to design ASE compensation filters and evaluate system performance.

The 6DOF model captures the effects of the structural flexibility on the sensor measurements, but neglects the influence of the structural flexibility on the rigid body dynamics

since this is generally a secondary effect. The equations used to model the structural dynamics are based on those described in References 2 and 3.

The equations governing the structural mode dynamics have the form

$$\left[ s^2 + 2\zeta_i \omega_i s + \omega_i^2 \right] \xi_i = \frac{1}{m_i} \sum_j \left[ \phi_i(\delta_j) F(\delta_j) + \left[ \phi_i(\delta_j) m_{R_j} \ell_{R_j} + \sigma_i(\delta_j) I_{y_j} \right] s^2 \delta_j(s) \right] \quad (\text{A.42})$$

where

$\xi_i$  - Generalized coordinate of the  $i^{\text{th}}$  structural mode

$\zeta_i$  - Damping of the  $i^{\text{th}}$  structural mode

$\omega_i$  - Natural frequency of the  $i^{\text{th}}$  structural mode (rad/sec)

$m_i$  - Generalized mass of the  $i^{\text{th}}$  structural mode (slug)

$\phi_i(\delta_j)$  - Deflection of the  $i^{\text{th}}$  structural mode at the location of control effector  $\delta_j$  (ft/ft)

$F(\delta_j)$  - Force due to control effector  $\delta_j$  which acts to excite the structural mode of interest.

This force lies in the plane of interest for bending modes. For torsional modes, the direction of the moment producing force is used.

$\sigma_i(\delta_j)$  - Slope of the  $i^{\text{th}}$  structural mode at the location of control effector  $\delta_j$  (rad/ft)

$m_{R_j}$  - Mass of control effector  $\delta_j$  (slug)

$\ell_{R_j}$  - Offset between the center of gravity and the hinge line of control effector  $\delta_j$  (ft)

$I_{y_j}$  - Moment of inertia of control effector  $\delta_j$  about its hinge line (slug-ft<sup>2</sup>)

The  $\phi_i(\delta_j) F(\delta_j)$  term on the right hand side represents the excitation of the  $i^{\text{th}}$  structural mode by the direct forces applied by the control effectors. The remaining terms on the right hand side represent the effect of the inertial reaction torque induced by the angular acceleration of the control effectors on the excitation of the structural mode. The excitation forces are summed over the control effector suite.

The effect of the structural modes on the sensor measurements depends on the location of the sensors along the mode shape. The effect of a given mode is proportional to the slope or deflection of the mode at the sensor location. The overall effect of the vehicle's flexibility on the

sensor measurements is the sum of the contributions from the various modes. Sensed quantities for a given mode are related to the mode shape as follows

$$\begin{array}{lll}
 \alpha_i & = \sigma_i(\alpha)\xi_i & \text{(Angle of Attack)} \\
 \beta_i & = \sigma_i(\beta)\xi_i & \text{(Sideslip)} \\
 p_i, q_i, r_i & = \sigma_i(\text{Gyro})\dot{\xi}_i & \text{(Rotational Rates)} \\
 h_i & = \phi_i(h)\xi_i & \text{(Altitude)} \\
 A_{y_i}, A_{z_i} & = \phi_i(\text{Accel})\ddot{\xi}_i & \text{(Linear Acceleration)} \\
 \phi_i, \theta_i, \psi_i & = \sigma_i(\text{Gyro})\xi_i & \text{(Body Attitudes)}
 \end{array}$$

For these equations, the quantity in parenthesis indicates the point at which the noted mode slope or deflection is defined. The mode slopes and deflections are defined with respect to the axis of interest.

Since detailed structural mode characteristics of the TAFE aircraft were not available, a structural model was created by combining the structural mode data of the F-15 ACTIVE with the TAFE aerodynamics. This model is approximate since it assumes the structural mode frequencies and mode shapes for the TAFE and F-15 ACTIVE are the same, but retains realism by capturing the structural mode excitation supplied by the relative forces and moments exerted by each control effector. The contribution of the ASE dynamics to the sensor measurements was verified to be comparable to that of the F-15 ACTIVE.

The first step in the development of the ASE dynamics model was to identify grid points on the F-15 ACTIVE structural model which correspond to the approximate location of the control effectors and sensors on the TAFE aircraft. These grid points are required to define the mode slopes and deflections used in the ASE dynamics differential equations. Since the aircraft are similar in size, the TAFE control effector and sensor locations were assumed to correspond to similarly located devices on the F-15 ACTIVE platform. The grid points used are provided in Table A.4.

The next step was to model the forces and inertial reaction torques which form the forcing terms that excite the structural modes. The direct force terms are computed directly from the TAFE aerodynamics and propulsion models, and are simply the force increments due to the

various control effectors. These terms come directly from the nonlinear aerodynamic and propulsion models and thus vary with flight condition and maneuver level.

TAFAs Sensors / Control Effectors	F-15 ACTIVE Sensors / Control Effectors
Trailing Edge Flap, Aft Body Flap, Aileron	Stabiator
Thrust Vectoring Nozzle	Thrust Vectoring Nozzle
Canard	Canard
Leading Edge Passive Porosity	Aileron
Forebody Blowing	(Location on Forward Forebody)
Accelerometers	Accelerometers
Gyros	Gyros
AoA / Sideslip	AoA / Sideslip
Altimeter	Accelerometer Location

**Table A.4: Grid Points Used in Development of TAFAs Structural Dynamics Model**

The inertial reaction torque terms are a function of the geometry of the control effectors. Since a detailed structural model of the TAFAs was not available, the control effector geometry data was estimated as described below. The inertial reaction torque only exists for control effectors which rotate a significant mass about a pivot point. As a result, the leading edge passive porosity and forebody blowing do not produce a significant inertial reaction torque. The mass, offset between the effector center of gravity and pivot axis, and the moment of inertia of the effector about its pivot point must be estimated.

The mass of the aerodynamic control effectors was estimated by multiplying the surface area of the control effectors by a density (mass/surface area). The density was computed using mass property data for the F/A-18C/D control surfaces, and assumed to be the same for the TAFAs aerodynamic control effectors. The density of the F/A-18C/D trailing edge flap (TEF) was used for the subsequent computations, and was found to be:

F/A-18C/D TEF Weight      117.39 lb  
 F/A-18C/D TEF Surface Area    47.45 ft<sup>2</sup>  
 density                      2.47 lb/ft<sup>2</sup> = 0.07689 slug/ft<sup>2</sup>

This led to the mass values for the TAFE aerodynamic control effectors provided in Table A.5. The mass of the thrust vectoring nozzle was based on mass property data for the F-15 ACTIVE, and is also provided in the table.

Control Effector	Surface Area (ft <sup>2</sup> )	Mass (slug)
Trailing Edge Flap	25.2	1.94
Aft Body Split Flap	10.9	0.84
Aileron	7.7	0.59
Canard	20.1	1.54
Thrust Vectoring Nozzle	-	9.1

**Table A.5: Mass Properties of TAFE Control Effectors**

The offset between the center of gravity and pivot point of each control effector,  $\ell_{R_j}$ , was estimated from the geometry of the control effectors. The effectors were assumed to have uniform density and thus the center of gravity is at the geometric center. The distance from the geometric center to the pivot point was thus taken as the required offset. The values are provided in Table A.6.

Control Effector	Offset Between cg and Pivot Point (ft)
Trailing Edge Flap	1.68
Aft Body Split Flap	1.28
Aileron	0.7
Canard	1.6
Thrust Vectoring Nozzle	1.0

**Table A.6: Offset Between cg and Pivot Point of TAFE Control Effectors**

The final quantity required for the inertial reaction torque model is the moment of inertia of each control effector about its pivot axis. This data was estimated from the mass moments of inertia for simple geometrical shapes (e.g. a thin rectangular plate). The resulting inertia data is provided in Table A.7.

<b>Control Effector</b>	<b>Moment of Inertia (slug-ft<sup>2</sup>)</b>
Trailing Edge Flap	36.38
Aft Body Split Flap	5.2
Aileron	5.95
Canard	3.88
Thrust Vectoring Nozzle	75

**Table A.7: Moment of Inertia of TAFE Control Effectors**

Using this data, the structural dynamics were integrated into the TAFE 6DOF. Longitudinal (symmetric) and lateral directional (anti-symmetric) modes were implemented separately. The lateral directional model includes lateral axis bending as well as torsional mode effects. These effects combine to form the forcing function for the lateral directional modal dynamics. The ASE model in the TAFE 6DOF is configured so that linear models can be extracted at selected operating points.

An example of the linear ASE dynamics model extracted from the TAFE 6DOF is provided in Figure A.7. This figure shows the magnitude of the frequency response relating the ASE contribution to sensed pitch rate and normal acceleration to the pitch axis control effector inputs. This data is for the low altitude ingress / egress flight condition described in Reference 1. This data shows high frequency peaks in the frequency response curves which exceed 20 dB, indicating the need for ASE filtering in the control law design.

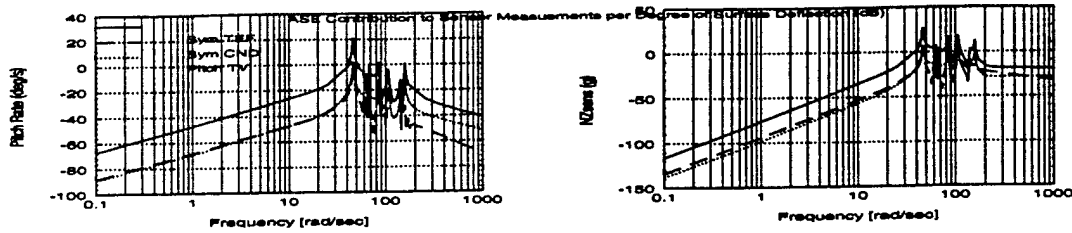


**Figure A.7: Frequency Response of Longitudinal Axis Flexible Vehicle Dynamics Model for Low Altitude Ingress / Egress Flight Condition**

### A.6 Actuator Models

The actuator models describe the dynamic response characteristics, position limits, and rate limits of the TAFE control effectors. Both high and low fidelity actuator models are available. The low fidelity model assumes position and rate limit capabilities based on nominal operating conditions. The high fidelity model computes the position and rate limit capabilities based on the surface loads (i.e. hinge moments). The hinge moment effects reduce the position and rate capabilities of the actuators at high dynamic pressure conditions.

The sign conventions of the TAFE control effectors are described in Figure A.8. Aerodynamic effectors and thrust vectoring sign conventions are described in terms of a positive deflection of the trailing edge (TE). A positive command to the forebody blowing effector vents thrust out the left side of the aircraft to yield a positive yawing moment. Positive commands to the leading edge passive porosity and aft body split flap (left or right) effectors cause them to open relative to their neutral position.

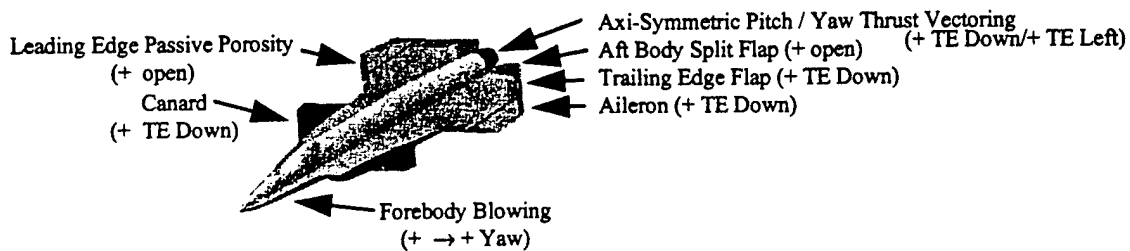


**Figure A.8: TAFE Control Effector Sign Conventions**

The actuator dynamics of the various control effectors are modeled using first or second order transfer functions with position and rate limits. The position and rate limits are applied to the integrator states rather than the integrator outputs to prevent windup during periods of saturation. The first order actuator dynamics are characterized by a bandwidth ( $\omega_B$ ), while the second order actuator dynamics are characterized by a damping ratio ( $\zeta$ ) and natural frequency ( $\omega_n$ ). The linear transfer functions of these models are provided below.

$$\frac{\delta}{\delta_c} = \frac{\omega_B}{s + \omega_B} \quad \frac{\delta}{\delta_c} = \frac{\omega_n^2}{s^2 + 2\zeta\omega_n s + \omega_n^2} \quad (\text{A.43})$$

The dynamic parameters used to characterize the TAFE actuators are provided in Table A.8.

Surface	Dynamics
Canard	$\omega_b = 40$ rad/s
LE Passive Porosity	$\omega_b = 30$ rad/s
Trailing Edge Flap	$\omega_b = 40$ rad/s
Aileron	$\omega_b = 40$ rad/s
Aft Body Flap	$\omega_b = 40$ rad/s
Vectoring Nozzle	$\zeta=0.8, \omega_n = 80$ rad/s
Forebody Blowing	$\omega_b = 20$ rad/s

**Table A.8: TAFE Actuator Dynamics**

The low fidelity actuator models use position and rate limits which characterize the capability under moderate loads. These limits are provided in Table A.9.

Surface	Position Limits	Rate Limits
Canard	-80°/10°	70°/s
LE Passive Porosity	0/1	10 s <sup>-1</sup>
Trailing Edge Flap	-30°/45°	90°/s
Aileron	-30°/30°	120°/s
Aft Body Flap	0°/90°	120°/s
Vectoring Nozzle	-30°/30°	60°/s
Forebody Blowing	±0.006	0.06 s <sup>-1</sup>

**Table A.9: TAFE Low Fidelity Actuator Model Position and Rate Limits**

The high fidelity actuator models reduce the position and rate limit capabilities of the actuator due to the aerodynamic loads acting on the effector at the current operating condition. Worst case models are formed by assuming the load always oppose motion of the surface. The aerodynamic loads do not affect the leading edge passive porosity, forebody blowing and thrust vectoring effectors, and thus their position and rate limits are unchanged from the low order model. Position and rate limit capabilities of the aerodynamic control effectors are characterized by the torque-speed curve shown in Figure A.9.

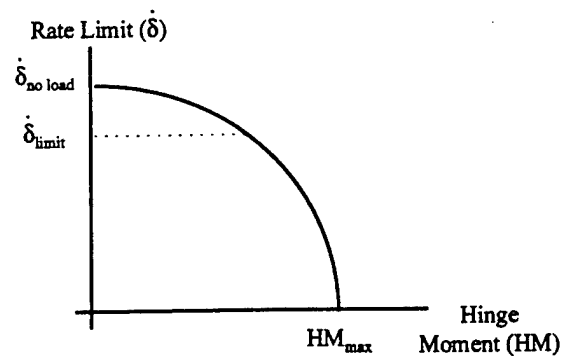


Figure A.9: High Fidelity Actuator Model Torque-Speed Curve

The torque-speed curve is characterized by a no load rate limit ( $\dot{\delta}_{no\ load}$ ) and a stall torque ( $HM_{max}$ ). The stall torque is the maximum load which the actuator can oppose to move the surface. The position and rate limits are computed from the torque-speed curve based on the current hinge moment load acting on the surface. The torque-speed is characterized by the equation

$$\left(\frac{\dot{\delta}}{\dot{\delta}_{no\ load}}\right)^2 + \left(\frac{HM}{HM_{max}}\right)^2 = 1 . \quad (A.44)$$

The hinge moment of each surface is computed based on a dimensionalized hinge moment derivative and the surface deflection. The equation is

$$HM = \bar{q} * S_{surf} * \ell * C_{HM} * |\delta| \quad (A.45)$$

where

- $\bar{q}$  Dynamic pressure
- $S_{surf}$  Surface area of the effector
- $l$  Offset between surface center of pressure and hinge line
- $C_{HM}$  Hinge moment derivative for given effector
- $\delta$  Deflection of given effector.

The position limits for a given effector are computed as the minimum of the deflections which yield the associated stall torque and the physical deflection limits of the effector. The equations are provided below.

$$\delta_{max_{HM}} = \frac{HM_{max}}{\bar{q} * S_{surf} * l * C_{HM}}$$

$$\delta_{upper\ limit} = \min(\delta_{max_{HM}}, \delta_{max_{physical\ limit}})$$

$$\delta_{lower\ limit} = \max(-\delta_{max_{HM}}, \delta_{min_{physical\ limit}})$$
(A.46)

The corresponding rate limit is computed from the equation for the torque-speed curve as

$$\dot{\delta}_{max} = \dot{\delta}_{no\ load} \sqrt{1 - \left(\frac{HM}{HM_{max}}\right)^2}$$
(A.47)

The rate limit capability is limited by a maximum achievable rate ( $\dot{\delta}_{limit}$ ) which characterizes the actuator's capability under the mechanical load imposed by the fin inertia, gearing, linkages, etc. The rate limit ( $\dot{\delta}_{limit}$ ) is assumed to equal the rate limit capability of the low fidelity actuator model so that the high fidelity model's rate capability will not exceed that of its low fidelity counterpart.

Data was obtained from Boeing's ASTOVL program indicating stall torque and no load rate limit requirements for the actuators. These values are assumed for the TAFE aircraft and are provided in Table A.10.

		No Load Rate Limit	Maximum Rate Capability
Surface	Stall Torque (in-lb)	( $\dot{\delta}_{no\ load}$ ) (deg/s)	( $\dot{\delta}_{limit}$ ) (deg/s)

Trailing Edge Flap	320000	145	90
Aileron	57000	170	120
Canard	290000	105	70
Aft Body Flap	35000	180	120

**Table A.10: TAFE High Fidelity Actuator Model Parameters**

The remaining parameters required for the TAFE high fidelity actuator model are those used to compute the hinge moments of the various control effectors as a function of dynamic pressure and surface deflection. A detailed hinge moment database would be collected by instrumenting the control effectors during wind tunnel testing and measuring the shear force, root bending moment and hinge moment as a function of flight condition and surface deflection. This database would include variations with mach and angle of attack to characterize changes in the air load acting on a given surface and movement of the center of pressure of the surfaces. A high fidelity hinge moment database is not available for the TAFE aircraft and thus a simple model will be used to capture the effects of hinge moments on the actuator position and rate capabilities.

Preliminary data obtained from the ASTOVL program showed that the trailing edge flaps and ailerons could reach their full deflection at dynamic pressures up to 560 psf. Comparable capability was assumed for the canard and aft body flap, and used to compute the hinge moment model parameters. The surface area of the effectors and the offset between the center of pressure and surface hinge line were estimated from the TAFE planform. The hinge moment derivative was then computed assuming that the maximum surface deflection yielded a hinge moment equal to the stall torque when the dynamic pressure was 560 psf. The resulting hinge moment model parameters are provided in Table A.11.

Surface	Surface Area $S$ (ft <sup>2</sup> )	Center of Pressure to Hinge Line Offset $l$ (in)	Hinge Moment Derivative $C_{HM}$ (1/deg)
Trailing Edge Flap	25.2	20.2	0.0246
Aileron	7.7	8.4	0.0552

Canard	20.2	19.2	0.0167
Aft Body Flap	10.9	15.4	0.0043

**Table A.11: TAFE Hinge Moment Model Parameters**

### A.7 Sensor Models

The TAFE sensor models simulate the expected signal characteristics yielded by the sensors on board the aircraft. These sensors include accelerometers, gyros, angle of attack and sideslip probes, the air data system, and the navigation / attitude reference system. All sensed signals are computed as the true value altered by a time delay, measurement bias, and zero mean white noise. The sensor model for a given feedback channel is shown in Figure A.10.

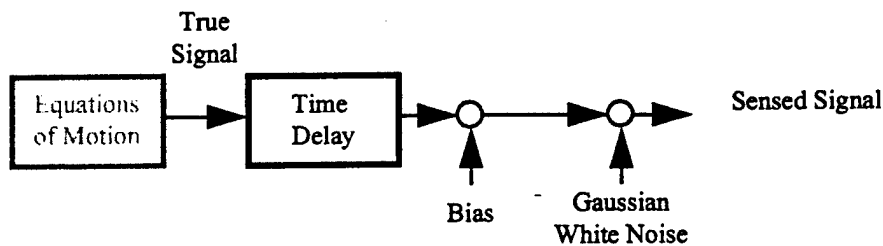


**Figure A.10: TAFE Sensor Model**

Specifications for the maximum time delay, bias level and noise standard deviation for each type of sensor are provided in Table A.12. The time delay parameter includes generation of the signal as well as the time between signal generation and utilization by the flight control algorithms.

Sensor Type	Time Delay (msec)	Bias	Noise Standard Deviation
<b>Accelerometers</b>			
AX, AY, AZ (ft/s <sup>2</sup> )	0	0.1	0.5
<b>Gyros</b>			
p (deg/s)	0	0.0	0.32
q, r (deg/s)	0	0.0	0.08
<b>AoA / Sideslip Probes</b>			

Angle of Attack (deg)	0	0.2	0.2
Sideslip (deg)	0	0.1	0.2
<b>Air Data System</b>			
Mach	10	0.01	0.01
Airspeed (ft/s)	10	1.0	10.0
Dynamic Pressure (psf)	10	0.0	10.0
<b>Navigation / Attitude Reference</b>			
Altitude (ft)	10	0.0	6.0
Roll Attitude (deg)	10	0.0	0.2
Pitch Attitude (deg)	10	0.1	0.2
Yaw Attitude (deg)	10	0.1	0.2
<b>Engine Thrust</b>			
Estimated Gross Thrust	10	10.0	300.0

**Table A.12: TAFE Sensor Model Parameters**

### A.8 Flight Control System Digital Effects

The flight control system digital effects model characterizes the time delay (i.e. phase lag) caused by the computational lag of the control laws. The computational lag is the time required for the control laws to generate control surface commands once the stick commands and sensor feedbacks are available in the flight control processor. The computational lag is equivalent to a time delay which adds phase lag to the loop response, thereby influencing stability and flying qualities.

The TAFE computational delay was estimated based on data collected under Boeing's Intelligent Flight Control (IFC) program (NASA funded effort). The IFC program is developing reconfigurable flight control laws which use system identification to generate on-line estimates of the stability and control derivatives. This data is used to form linear models of the plant at the current operating condition. The plant models used with a Riccati equation solver to generate linear quadratic control law gains on-line. The IFC program is using a Shark digital signal processing (DSP) chip to perform the system identification, while the Riccati solution and control law computations are performed on the main processor (68040 chip). The Riccati

solution is performed as a background task, which yields a 20 Hz computation rate. The control law calculations are performed at 80 Hz. Timing analysis on the flight hardware has shown computational delays for the calculation of the control laws of approximately 6 msec.

The Boeing TAFA control laws are based on a dynamic inversion control architecture with on-line single layer neural networks to cancel the error between the plant model and the actual plant dynamics. System identification is used to generate control derivatives used by the on line control effector management (ICEM) to generate control effector commands which produce the required control moments while optimizing specified performance objectives (load alleviation, ...). This approach minimizes the need for system identification for stabilizing the aircraft following failure or damage. As a result, the system identification is not time critical and thus can be relegated to a background task. Boeing's dynamic inversion control laws have been executed at 80 Hz in real time on a variety of flight processors, including 68040 and i960 chips. Current processors (e.g. Pentium, Power PC, ...) far exceed the throughput capabilities of the 68040 and i960, and are expected to be able to handle the additional overhead of the on-line neural networks and ICEM. Timing analysis on the selected flight processor will be required to determine whether the system identification can be run as a background task on the main processor or whether a DSP chip will be required to host these algorithms. Due to increased throughput capability of current processors, it is reasonable to expect that the reconfigurable flight control algorithms will exhibit computational delays similar to those observed with the IFC algorithms. A computational delay of 10 msec is assumed for conservatism.

### **A.9 Loads Model**

The TAFA loads model characterizes the shear forces and torques at various points on the aircraft due to the aerodynamic loads acting on the vehicle. The loads acting on the vehicle must remain within the structural limits to preserve flight safety and the vehicle's fatigue life. The loads acting on the vehicle are a function of the flight condition and control effector utilization. It is common for aircraft control laws to employ maneuver load alleviation logic, which utilizes the control in a manner which keeps the loads within the structural limits while achieving the desired maneuvers.

The TAFAs loads model generates the shear force, bending moment and torque moment at critical points on the aircraft structure. The points were selected to be the canard root, wing root and wing fold as shown in Figure A.11.

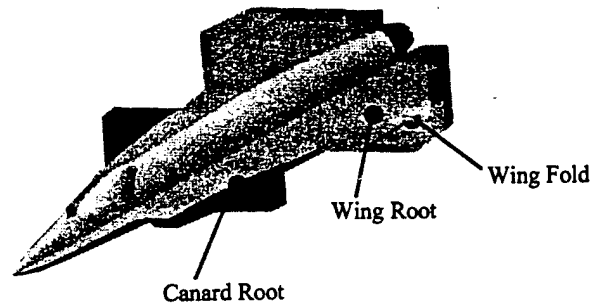


**Figure A.11: TAFAs Loads Model Definitions**

Loads are monitored for both sides of the aircraft. The shear force is measured positive up and expressed in pounds. A positive bending moment acts to bend the tip of the wing or canard over the top of the aircraft, while a positive torque moment acts to raise the leading edge of the wing or canard. The torque and bending moments are expressed in inch pounds.

The loads model was developed using the MSC/NASTRAN doublet lattice aerodynamic method on a flat lifting surface model approximating the TAFAs planform. The aerodynamic model was built to best approximate the important features of the actual aircraft configuration given the constraints of the doublet lattice aerodynamic method. The model panel geometry was designed to incorporate the canard, leading and trailing edge flaps, and the aileron. The layout of the wing panel arrangement was complicated by the very low taper ratio and constant chord trailing edge control surfaces. The left half of the aircraft was modeled, and symmetry was assumed.

The aft body split flaps are a clam shell device, with one panel opening above the wing and the other below the wing. The aft body flaps produce negligible lift and thus do not have a significant contribution to the shear force at the wing root or wing fold. The panels above and below the wing produce a net torque and bending moments near zero since the contributions of the upper and lower panels cancel each other. Based on these considerations, the aft body split flaps were excluded from the loads model. The thrust vectoring and forebody blowing devices

apply forces directly to the aircraft's fuselage and thus do not contribute to the aerodynamic loads of interest.

Aerodynamic analyses were conducted to identify the effect of the aircraft state variables (angle of attack, sideslip, rotational rates, control surface deflections) on each component load for a variety of flight conditions. Symmetric and anti-symmetric unit trim variable analyses were conducted at Mach numbers 0.6, 0.8, 0.9, 1.1, 1.2, and 1.4 to produce pressure distributions across the planform. These pressures were then integrated into canard, wing root, and wing fold shear force, bending moment and torsion moment. This analysis produced derivatives of the desired loads with respect to each aircraft state variable. The loads are then calculated by multiplying each load derivative by its respective state variable, and summing the contributions across the state variables.

#### **A.10 Atmosphere Model**

The TAFE atmosphere model describes the properties of the air near the vehicle. These properties include basic atmospheric conditions (pressure, temperature, speed of sound, air density, and air coefficient of friction), as well as atmospheric disturbances (winds, and turbulence). These models are described in the following sections.

##### **A.10.1 Atmospheric Conditions**

The TAFE atmosphere model implements MIL-STD-210A and US Standard Atmosphere 1966 Supplements models for use in simulation and analysis. The model allows the user to select from the various atmosphere models (source and day type). In addition, the user is allowed to include pressure and temperature biases as a possible aid in matching flight test data results. The model produces outside air temperature, static pressure, air density, speed of sound, and the air coefficient of friction as a function of altitude. The available atmosphere models are:

MIL-STD-210A	Tropical Day
MIL-STD-210A	Polar Day
MIL-STD-210A	Hot Day

MIL-STD-210A	Cold Day
U.S. Standard Atmosphere	Standard Day (45° N Spring/Fall)
U.S. Standard Atmosphere	Hot Day (30° N July)
U.S. Standard Atmosphere	Cold Day (75° N January)

The equations governing the MIL-STD-210A and U.S. Standard Atmosphere 1966 Supplements differ, primarily in the fact that the MIL-STD-210A models use the standard day temperature gradients for calculations with all day types. Temperature gradients for the selected day type are used in calculations for the U.S. Standard Atmosphere 1966 Supplements models. As a result, the U.S. Standard Atmosphere 1966 Supplements models are implemented via the appropriate equations, while the MIL-STD-210A models are stored as tables.

The model produces outside air temperature, static pressure, air density, speed of sound, and the air coefficient of friction as a function of altitude for the selected day type. The model also allows the user to specify pressure and temperature biases as a possible aid in matching flight test data results. The pressure biases can be added in two ways as given by the equation

$$P = P_{nom} \left( \frac{P_0 + dP_0}{P_0} \right) + B_{Bias} \quad (A.48)$$

where  $P_{nom}$  is the nominal pressure profile for the selected day type,  $P_0$  is the sea level pressure for the selected day type,  $dP_0$  is the sea level pressure increment, and  $P_{Bias}$  is the pressure bias. The sea level pressure increment produces an effect which increases with altitude while maintaining a hydrostatically balanced model. The pressure bias is constant over all altitudes, and yields a model which is not hydrostatically balanced. The temperature bias is applied as

$$T = T_{nom} + T_{Bias} \quad (A.49)$$

where  $T_{nom}$  is the nominal temperature profile for the selected day type, and  $T_{Bias}$  is the temperature bias. The temperature bias also maintains a hydrostatically balanced model.

### A.10.2 Wind and Turbulence

The TAFE simulation is supported by wind and turbulence models which implements the MIL-1797A steady state wind, wind shear, turbulence, and discrete gust characteristics for use

in simulation analyses. The model allows the user to activate any combination of these atmospheric characteristics. The wind and turbulence models are described in detail below.

The steady state wind specifies a constant wind magnitude and direction which is independent of altitude. The wind shear component models wind variations as a function of ground clearance altitude. Linear, logarithmic and vector shear models are available. The linear and logarithmic shear models describe a constant direction wind whose magnitude varies with altitude. The vector shear model describes a constant magnitude wind whose direction varies with altitude. The turbulence models are implemented using the Dryden spectra for linear (axial, lateral, vertical) and rotational (roll, pitch and yaw) disturbances. Light, moderate and severe turbulence models are available for both high and low altitude flight. The discrete gust models implement a single gust profile, triggered at a specified altitude, specified as a function of time, altitude, or distance traveled.

The net result of the wind and turbulence model is linear wind velocity components in inertial axes, and rotational gust components in the body axes. The linear wind components are combined with the aircraft's inertial velocity to create airspeed components. The body axis airspeed components are used to compute angle of attack and sideslip angles. The rotational gust components are combined with the body axis rotational rates to drive the damping terms of the aerodynamics model.

The implementation of the angle of attack and sideslip rate computations does not entirely account for the turbulence influence. For example, the angle of attack rate is computed as

$$\dot{\alpha} = \frac{u\dot{w} - w\dot{u}}{u^2 + w^2} \quad (\text{A.50})$$

The wind and turbulence effects are included in the linear velocity terms, but not the linear acceleration terms. Analytical computation of the linear acceleration terms is not possible when turbulence is active since this would involve differentiating a random process. The influence of turbulence on the angle of attack and sideslip rates can only be accurately captured by numerically differentiating the corresponding angle of attack and sideslip angles. An alternate approach is to numerically differentiate the linear velocity terms for use in the above equation. Refined computation of the angle of attack and sideslip rates due to turbulence is left for user implementation since the preferred approach may be application dependent.

The steady state wind model specifies a constant wind magnitude and direction which does not vary with altitude. The direction is specified by an inertial heading and direction relative to the horizontal plane.

The linear wind shear model characterizes wind variations as a linear function of ground clearance altitude. The wind speed varies linearly with ground clearance altitude with the wind maintaining a constant direction. The wind shear model contains only horizontal plane wind components, with the vertical wind shear component being zero. The linear wind shear model parameter definitions are illustrated in Figure A.12.

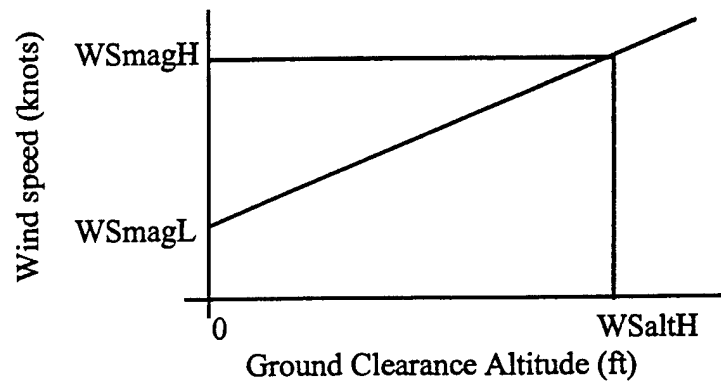


Figure A.12: Linear Wind Shear Model Definitions

The logarithmic wind shear model characterizes wind variations as a logarithmic function of ground clearance altitude. The wind speed varies logarithmically with ground clearance altitude, with the wind maintaining a constant direction. The wind shear model contains only horizontal plane wind components, with the vertical wind shear component being zero. The MIL\_SPEC logarithmic shear model differs for up-and-away flight and carrier take off and landing. The desired characteristic is selectable in the model. The logarithmic wind shear model has the form

$$WS = WSmag * \frac{\ln(h_{CL}/z_0)}{\ln(20/z_0)} \quad (A.51)$$

where  $h_{CL}$  is the ground clearance altitude,  $z_0 = 2.0$  for up-and-away and  $z_0 = 0.15$  for carrier takeoff and landing, and  $WS$  is the wind shear magnitude. The up-and-away and carrier wind shear models are illustrated in Figure A.13

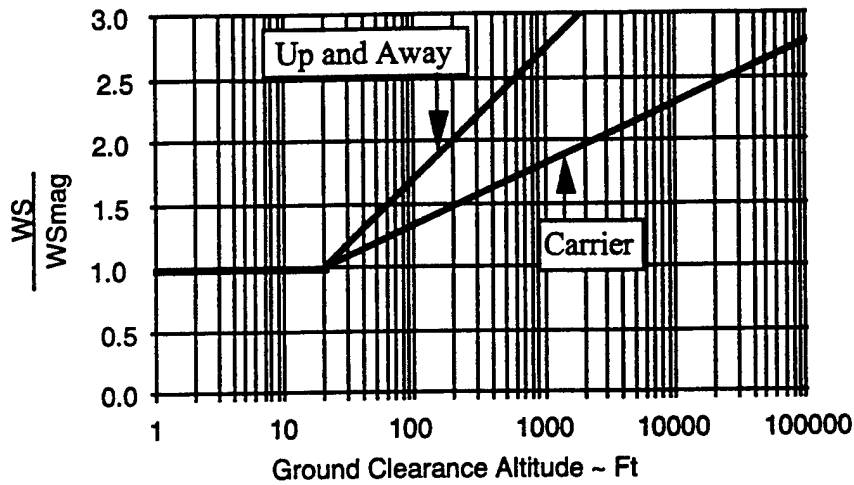


Figure A.13: Logarithmic Wind Shear Model

The vector wind shear model describes a constant magnitude wind whose direction varies linearly with ground clearance altitude. The vector wind shear model contains only horizontal plane wind components, with the vertical wind shear component being zero. A specified change in wind direction occurs over a specified change in altitude. The vector wind shear model parameter definitions are illustrated in Figure A.14.

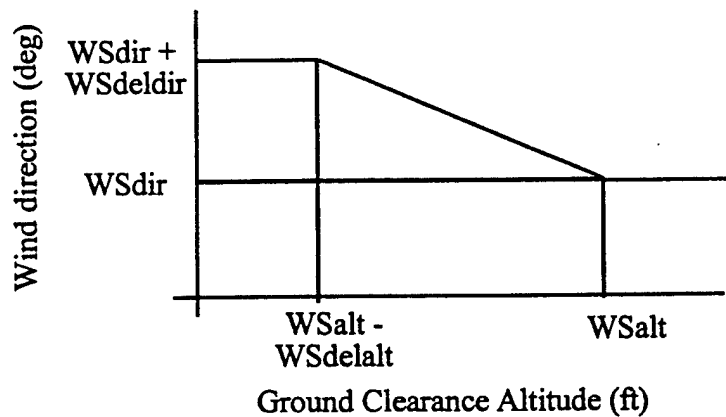


Figure A.14: Vector Wind Shear Model

The continuous turbulence models are implemented using the Dryden spectra. Light, moderate and severe turbulence models are available for both high and low altitude flight. The spectra are implemented using weighting filters driven by Gaussian white noise sources to produce the required correlation characteristics. Linear (axial, lateral, and vertical) and rotational (roll, pitch, and yaw) turbulence models are implemented. The linear turbulence is directed along the horizontal flight path angle, while the rotational turbulence spectra are implemented in body axes. Gust multipliers are provided to scale (or turn off) the turbulence in selected axes.

The Dryden spectra and continuous domain weighting filter implementations are summarized in Figure A.15.

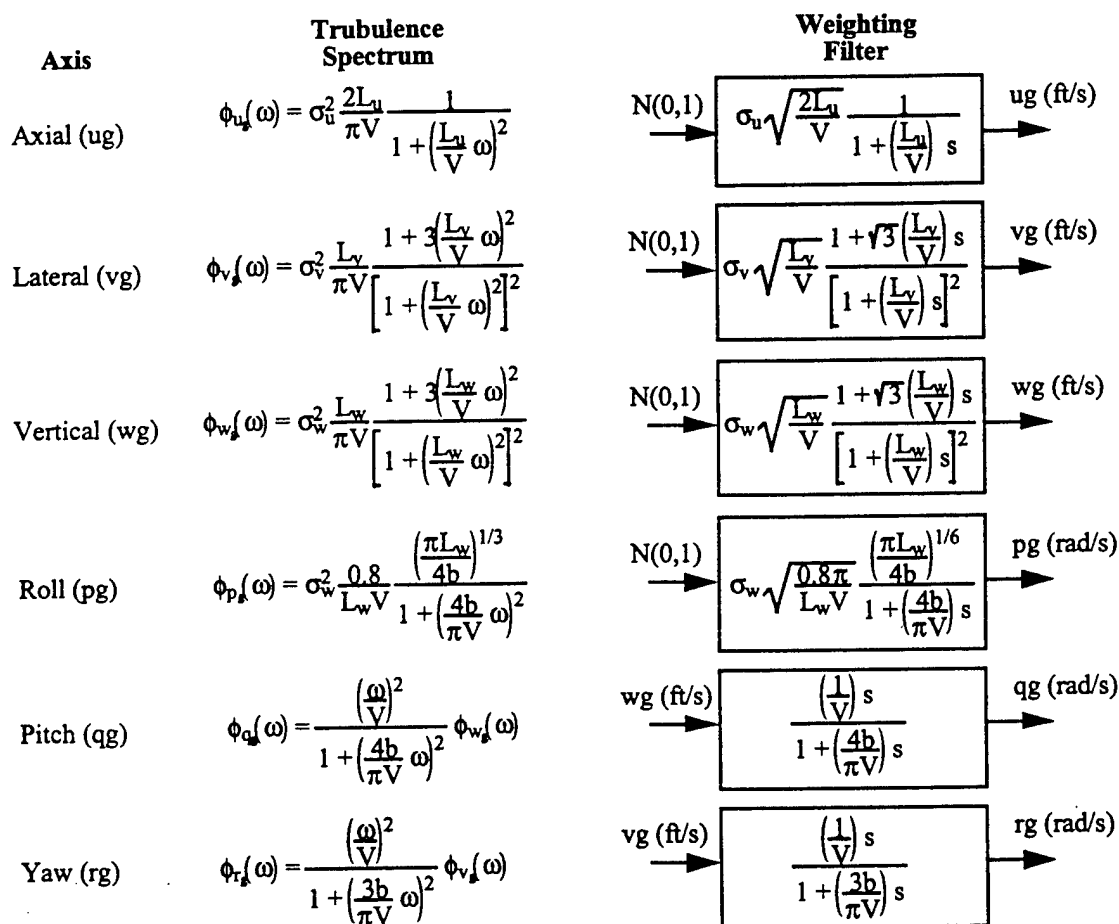


Figure A.15: Dryden Turbulence Spectra and Continuous Weighting Filter

Implementation

The turbulence model parameters for light, moderate, and severe turbulence are provided in Table A.13.

Condition	RMS Intensities ~ ft/sec ( $\sigma_u, \sigma_v, \sigma_w$ )	Scale Lengths ~ ft ( $L_u, L_v, L_w$ )
Altitude > 1000 ft	$\sigma_u = \sigma_v = \sigma_w$ ; function of altitude and turbulence severity shown in Figure A.16	$L_u = 1750$ $L_v = L_w = 875$
Altitude < 1000 ft (Carrier Environment)	$\sigma_u = 1.77, \sigma_v = 1.69, \sigma_w = 1.06$	$L_u = L_v = L_w = 100$
Altitude < 1000 ft (Land Environment)	$\sigma_w = 0.1 * U_{20}$ $\sigma_u = \sigma_w / (0.177 + 0.000823h)^{0.4}$ $\sigma_v = \sigma_u$	$L_u = h / (0.177 + 0.000823h)^{1.2}$ $L_v = L_u / 2$ $L_w = h / 2$

$U_{20} = 15$  knots (light turb.), 30 knots (moderate turb.), 45 knots (severe turb.)

Table A.13: Turbulence Model Parameters

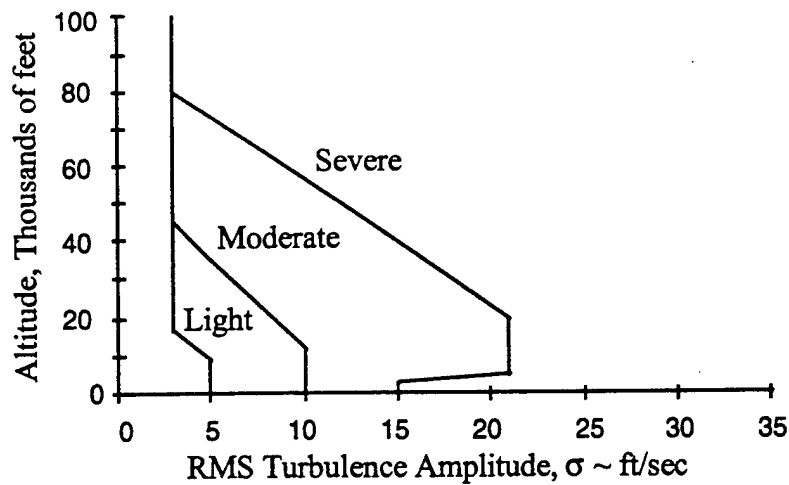


**Figure A.16: Medium / High Altitude Turbulence Intensities**

The discrete gust models implement a single gust profile, triggered at a specified altitude, and specified as a function of time, altitude, or distance traveled. The time dependent gusts can be used to implement user specified gust profiles in the axial, lateral, vertical and roll axes. The altitude and distance dependent gusts exhibit a one minus cosine characteristic and can be employed in one of the four axes (axial, lateral, vertical and roll). The user is allowed to specify the frequency of the gust profile, the maximum gust magnitude, and distance between gusts.

The discrete gust as a function of time model implements a single gust profile, triggered at a specified altitude. If a gust profile is not provided, the MIL-SPEC discrete gust profile of Figure A.17 is applied in the lateral and vertical directions. The gust profile of Figure A.17 represents an actual wind gust encountered during air vehicle flight testing.

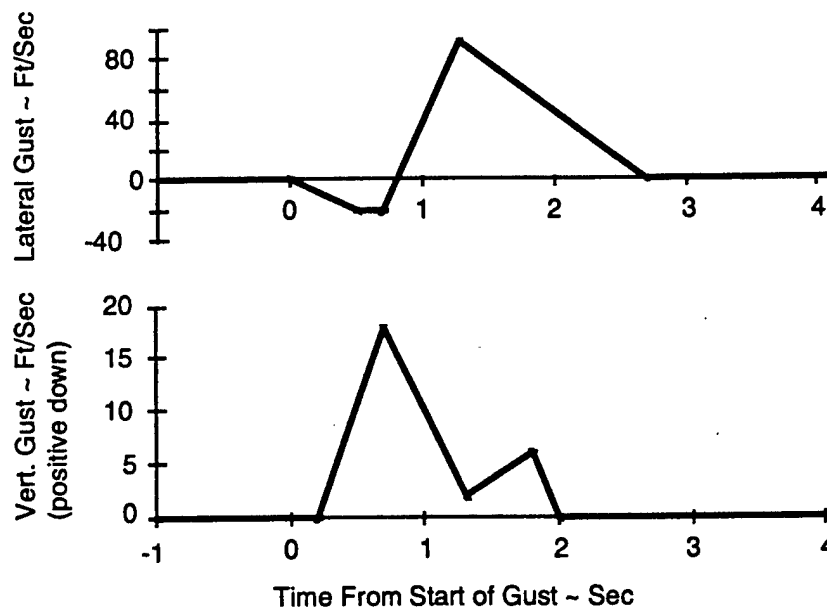


**Figure A.17: MIL-SPEC Discrete Gust Profile**

The discrete gust as a function of altitude or distance models implement a single gust profile, triggered at a specified altitude. These gusts exhibit a one minus cosine characteristic and can be employed in one of the four axes (axial, lateral, vertical and roll). The user is allowed to specify

the frequency of the gust profile, the maximum gust magnitude, and distance between gusts. Definitions of these parameters are shown in Figure A.18.

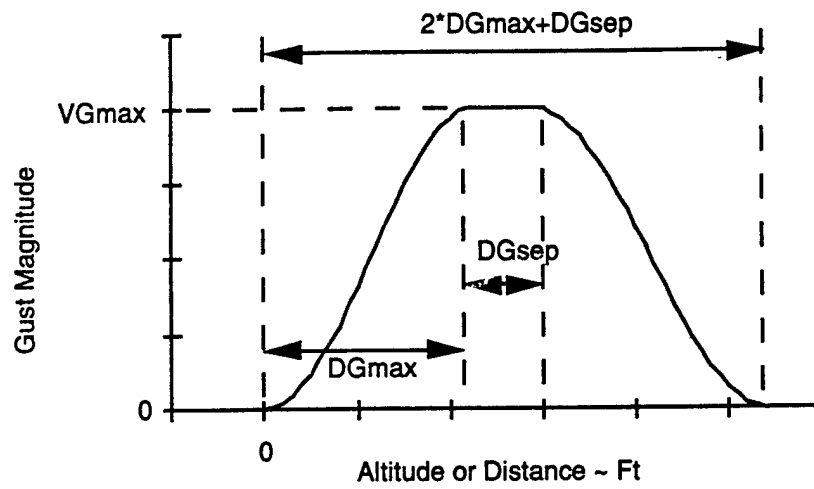


Figure A.18: One Minus Cosine Discrete Gust Model